Michael Zawodzki, BSc

# Interfacial Morphology and Device Performance of Organic Solar Cells

Master Thesis

For obtaining the Acadamic Degree:
Diplom-Ingenieur

Master Programm
of technical Physics

University of Technology

Supervisor:

Ao.Univ.-Prof. Dipl.-Ing. Dr.techn. Roland Resel

Institute of Solid State Physics
Graz University of Technology

Graz, September 2013

Deutsche Fassung:
Beschluss der Curricula-Kommission für Bachelor-, Master- und Diplomstudien vom 10.11.2008
Genehmigung des Senates am 1.12.2008

# EIDESSTATTLICHE ERKLÄRUNG

Ich erkläre an Eides statt, dass ich die vorliegende Arbeit selbstständig verfasst, andere als die angegebenen Quellen/Hilfsmittel nicht benutzt, und die den benutzten Quellen wörtlich und inhaltlich entnommenen Stellen als solche kenntlich gemacht habe.

Graz, am ……………………………  ………………………………………………..
(Unterschrift)

Englische Fassung:

# STATUTORY DECLARATION

I declare that I have authored this thesis independently, that I have not used other than the declared sources / resources, and that I have explicitly marked all material which has been quoted either literally or by content from the used sources.

……………………………  ………………………………………………..
date  (signature)

*Einsicht haben, oder den anhören,*
*der sie hat*

*Ohne Verstand, eigenen oder geborgten, läßt sich's nicht leben. Allein viele wissen nicht, daß sie nichts wissen, und andre glauben zu wissen, wissen aber nichts. Gebrechen des Kopfs sind unheilbar, und da die Unwissenden sich nicht kennen, suchen sie auch nicht, was ihnen abgeht. Manche würden weise sein, wenn sie nicht glaubten, es zu sein. Daher kommt es, daß, obwohl die Orakel der Klugheit selten sind, diese dennoch unbeschäftigt leben, weil keiner sie um Rat frägt. Sich beraten, schmälert nicht die Größe und zeugt nicht von Mangel eigener Fähigkeit, vielmehr ist sich gut beraten ein Beweis derselben. Man überlege mit der Vernunft, damit man nicht widerlegt werde vom unglücklichen Ausgang.*

A. Schopenhauer, *Die Kunst der Weltklugheit*, Gracians Handorakel

# Interfacial Morphology and Device Performance of Organic Bilayer Solar Cells

## Abstract

The efficiency of organic solar cells strongly depends on the polymer interface, where the charge separation of the exciton takes place. Therefore, a detailed knowledge of the polymer interface is required. Investigations were performed on an organic bilayer solar cell, using P3HT(Poly(3-hexylthiophen-2,5-diyl)) as spin-coated n-type organic semiconductor and F8BT(Poly[(9,9-di-n-octylfluorenyl-2,7-diyl)-alt-(benzo[2,1,3]thiadiazol-4,8-diyl)]) as a p-type material, which was floated on top of the P3HT. Those bilayers were investigated on oxidized silicon substrates with X-ray reflectivity, neutron reflectivity and grazing incident X-ray diffraction at different annealing temperatures ($90°C$ to $110°C$) and annealing times ($0\ min$ to $250\ min$). Through annealing a continuous change of the interfacial morphology was obtaind, the observed roughness was in the order of a few nanometers. Organic solar cell devices were built on ITO(Indium Tin Oxid) surface with a silver cathode on top of the active layers. The photovoltaic measurements showed an increase of $40 - 180\ \%$ in short circuit current for an annealing time of $8 - 40\ min$ and consequently an increase of $40 - 100\ \%$ in efficiency was observed, despite the constant dropping of the open circuit voltage. For longer annealing times the enhanced short circuit current and efficiency began to drop as well, like the open circuit voltage. As expected, the effects became stronger at higher temperatures and the maximum efficiency was shifted to shorter times. The improve performance is connected to structural changes, which increased the charge mobility and through that the charge separation of the exctions at the interface. The result suggests that a smooth interface provids an effective charge separation, in contrast rougher interfaces have a higher disorder, which may leds to a decrease of performance.

**Key words:** organic solar cells, interface roughness, X-ray reflectivity, neutron reflectivity, gracing incident X-ray diffraction

# Grenzflächenmorphologie und Solarzelleneffizienz von Organischen Zwei-Schicht Solarzellen

## Kurzfassung

Der Wirkungsgrad einer organischen Solarzelle hängt sehr stark von der Effektivität der Ladungsseparation der Exzitonen an den Phasengrenzflächen der Polymere ab. Um diesen Effekt untersuchen zu können, wurden Solarzellen aus zwei Schichten hergestellt. Das Polymer auf der Anodenseite war P3HT(Poly(3-hexylthiophen-2,5-diyl)) ein n-Typ Halbleiter, auf welches das p-Typ Polymer F8BT(Poly[(9,9-di-n-octylfluorenyl-2,7-diyl)-alt-(benzo[2,1,3]thiadiazol-4,8-diyl)]) mittels Floating aufgebracht wurde. Dieses Zwei-Schichtsystem wurde auf Siliziumsubstraten mittels Röntgenreflektivität, Neutronenreflektivität und Röntgendiffraktometrie mit streifendem Einfall bei unterschiedliche Temperaturen ($90°C$ bis $110°C$) und Wärmebehandlungszeiten ($0\ min$ bis $250\ min$) untersucht. Durch die Wärmebehandlung kam es zu einer Änderung der Grenzflächenmorphologie. Die Rauigkeiten lagen in der Größenordung von wenigen Nanometern. Die organischen Solarzellen wurden direkt auf Indium Zinn Oxid(ITO)-Substrat gefertigt und eine Silberkathode auf die Polymerschichten aufgedampft. Die photovoltaischen Messungen zeigten eine Erhöhung des Photostromes von 40 bis 180 % für Wärmebehandlungszeiten von 8 bis 40 $min$ und damit einhergehend eine Steigerung der Effizienz um 40 bis 100 %, parallel dazu sank jedoch die Kurzschlussspannung der Zelle. Längere Wärmebehandlungen führten zu einem Verfallen des gesteigerten Photostromes, der Kurzschlussspannung und folglich der Effizienz. Röntgenuntersuchungen, sowie die photovoltaischen Messungen zeigten erwartungsgemäß eine Beschleunigung der Effekte bei höheren Temperaturen. Die Leistungssteigerung wird auf eine strukturelle Änderung des P3HTs zurückgeführt, wodurch sich die Mobilität der Löcher und dadruch die Ladungsseparation der Exzitonen verbessern. Das Ergebnis legt nahe, dass eine glatte Grenzfläche zwischen den Polymeren eine Ladungstrennung der Exzitonen begünstigt, hingegen ist die Ladungstrennung bei höher Grenzflächenrauigkeit weniger effektiv.

**Schlagwörter:** Organische Solarzelle, Grenzflächenrauigkeit, Röntgenreflektivität, Neutronenreflektivität, Röntgendiffraktometrie mit streifendem Einfall

# Contents

# 1 Introduction

## 1.1 X-Ray Reflectivity(XRR)

The investigation of thin films with X-rays scattering methods has a long history, [1]. It is actually a quite straight forward method for the determination of thickness, roughness and electron density of inorganic and organic thin films on defined substrates.
The theoretical background, which is following, is a summary mostly out of Jen Als-Nielson [2], Metin Tolan [3], Mario Birkholz [4] and Theo Neger [5].

### 1.1.1 Basics

The electron usually circles in the corresponding orbitals of the atom or molecule. When an electro-magnetic wave hits an isotropic dielectric medium, its electrons begin to interact with the electro-magnetic wave. Consequently the electron is accelerated, that means it leaves its equilibrium state, which causes additionally a damping. A simplified look, where the orbitals are approximated with the Bohr model as circles gives the following mathematical expression:

$$m_e \frac{d^2\mathbf{r}^2}{dt^2} + m_e \gamma \frac{d\mathbf{r}}{dt} + m_e \omega_0^2 \mathbf{r} = -e\mathbf{E}$$

$\gamma$ is the damping factor, $\omega_0$ resonance frequency, $\mathbf{E}$ electrical field, which disturbs the electron and $\mathbf{r}$ the position of the electron.
With an ansatz for harmonic oscillations $r = r_0 e^{-i\omega t}$ and $E = E_0 e^{-i\omega t}$ follows:

$$\mathbf{P} = \frac{Ne^2}{(\omega_0^2 - \omega^2 - i\gamma\omega)m_e}\mathbf{E} \tag{1.1}$$

$\mathbf{P}$ is the polarisation and $N$ number of electrons in a certain volume. That means, when an electro magnetic wave is travelling through a dielectric medium, it polarizes its environment. This effect strongly depends on the frequency of the wave and it is called dynamic polarisation. But what happens with the wave? Regarding the Maxwell equations for a light in a dielectric medium:

$$\nabla \times (\nabla \times \mathbf{E}) = -\frac{1}{c^2}\frac{\partial^2 \mathbf{E}}{\partial t^2} - \frac{\partial^2 \mathbf{P}}{\partial t^2} \tag{1.2}$$

With the use of the dynamic polarisation Eqn. 1.1, the ansatz for plain electro magnetic wave($E = E_0 e^{i(Kz - \omega t)}$ and $\nabla \times (\nabla \times \mathbf{E}) = -\nabla^2 \mathbf{E}$ the Eqn. 1.2 turns into::

$$\nabla^2 \mathbf{E} = -\frac{\omega^2}{c^2}(1 + \frac{Ne^2}{m_e \varepsilon_0}\frac{1}{(\omega_0^2 - \omega^2 - i\gamma\omega)}) \tag{1.3}$$

The expression is equal to $\nabla^2\mathbf{E} = -K^2$ and $\frac{\omega^2}{c^2} = k^2$. Out of this correlation the refraction index could be identified as $n(r)^2 = 1 + \frac{Ne^2}{m_e\varepsilon_0}\frac{1}{(\omega_0^2-\omega^2-i\gamma\omega)}$, which could be disassembled in $N = n + i\kappa$. $\kappa$ is identified as *absorbtion coefficient*.
A more common form of Eqn. 1.2 is the so called Helmholtz equation:

$$\mathbf{\Delta E(r)} = k^2\mathbf{n(r)}^2 E(r) \tag{1.4}$$

Until now the whole formalism is based on the assumption that all electrons are equally bound to its nuclei, but in reality this is not the case. Electrons in different shells or atoms have different bond strenghts. Therefore they have also different resonance frequencies and damping factors($\gamma_i$). Regarding all this, the refraction index is expressed as:

$$n(r)^2 = 1 + \frac{Ne^2}{m_e\varepsilon_0}\sum_{j=1}^{N}\frac{f_j}{\omega_j^2 - \omega^2 - i\gamma_j\omega} \tag{1.5}$$

$f_j$ are called oscillation strength and are in general complex numbers $f_j = f_j^0 + f_j'(E) + if_j''(E)$. $f_j'(E)$ and $f_j''(E)$ are dispersion and absorption corrections, [4].
X-ray have a very high frequency, that means $\omega >> \omega_j$. Because of this relation the $\omega^2$ in the denominator becomes very strong against $\omega_j^2$ and therefore the refraction index becomes $n < 1$. With the assumption for X-rays the following equation for the refraction index is gained:

$$n(r) = 1 - \delta(r) + i\beta(r) \tag{1.6}$$

Where

$$\delta(r) = \frac{2\pi r_e\rho_e(r)}{k^2} \tag{1.7}$$

and

$$\beta(r) = \frac{\mu(r)}{2k} \tag{1.8}$$

$\rho_e(r)$ is the electron density, $\mu(r)$ the attenuation coefficient in a certain volume $\mathbf{r}$, $r_e$ the *Thomson scattering length*$(2.815 \cdot 10^{-15}\ m)$ and $k$ is the wave vector of the X-ray. For a more detailed derivation of $\delta(r)$ and $\beta(r)$ from Eqn. 1.5, it is referred to [2], [3], [4].

### 1.1.2 Principles of XRR

Taking Eqn. 1.6 and just regarding the effect of $\delta(r)$ on the refraction index becomes $n(r) < 1$, because $\delta(r)$ is in the range of $\approx 10^{-6}$ for X-rays. The absorption $\beta(r)$ is usually one or two magnitudes smaller and could be in the most cases neglected, [3].
Using *Snell's -Law* of diffraction a correlation between $\delta(r)$ and the angle for total reflection can be found:

$$\cos(\alpha_i) = n\cos(\alpha_t) \tag{1.9}$$

$\alpha_i$ is the incident angle of the beam, $\alpha_t$ the angle of transmitted beam and $n(r)$ the refraction index. The $\alpha_c$ critical angle can be derived, if $\alpha_t$ is set $\alpha_t = 0$ for total reflection. With the use of $n(r) \approx 1 - \delta(r)$:

$$\cos(\alpha_c) = 1 - \frac{\alpha_c^2}{2} = 1 - \delta(r)$$

Valid for small incident angles. The critical angle $\alpha_c$ for a material is:

$$\alpha_c = \sqrt{2\delta(r)} = \frac{1}{k}\sqrt{2\pi r_e \rho_e(r)}$$

That means for incident angles smaller than $\alpha_c$ the X-ray can not penetrate the material it gets total reflected.
$\delta(r)$ is correlated to the electron density, see Eqn. 1.7. In Tab. 1.1.2 values for different materials are listed.

Table 1.1: Different inorganic materials and polystrene with the corresponding critical values for $CuK_\alpha = 1.54\ \AA$. $\rho/[g/cm^{-3}]$ mass density, $\rho_e/[\AA^{-3}]$ electron density, $\alpha_c/[°]$ critical angle and $q_c/[\AA^{-1}]$ critical scattering vector, [2]

| Compound | $\rho/[g/cm^{-3}]$ | $\rho_e/[\AA^{-3}]$ | $\alpha_c/[°]$ | $q_c/[\AA^{-1}]$ |
|---|---|---|---|---|
| $SiO_2$ | 2.20 | 0.662 | 0.216 | 0.031 |
| $Si$ | 2.33 | 0.712 | 0.225 | 0.032 |
| $Nb_2O_5$ | 4.47 | 1.236 | 0.294 | 0.042 |
| $ZnO$ | 5.61 | 1.576 | 0.326 | 0.046 |
| $C$ | 2.26 | 0.680 | 0.217 | 0.031 |
| $Au$ | 19.32 | 4.666 | 0.570 | 0.081 |
| $W$ | 19.30 | 4.678 | 0.569 | 0.081 |
| *polystrene* | 1.00 | 0.325 | 0.112 | 0.016 |

## Specular Condition

In X-ray reflectivity the specular condition is used to analyse thin films on defined substrates. Specular condition is given, if $\alpha_i = \alpha_f$, where $\alpha_f$ is the angles of the diffracted side, see Fig. 1.1

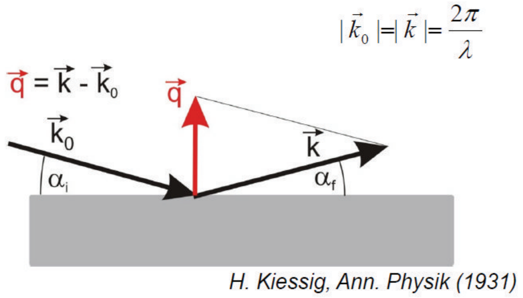

H. Kiessig, Ann. Physik (1931)

Figure 1.1: Specular condition in the reciprocal space. $k_0$ is the incident wave and $k$ the diffracted, [6].

For an XRR-scan $\alpha_i$ and $\alpha_f$ have to be change simultaneously to maintain the specular condition. In Fig. 1.1 the diffraction vector $q_z$ is depicted. In general the reciprocal diffraction vector $q$ is:

$$\mathbf{q} = \mathbf{k} - \mathbf{k_0}$$

$k = \frac{2\pi}{\lambda}$, because the specular condition is used $q$ simplifies to $q_z$.

$$q_z = \frac{4\pi}{\lambda} \sin(\alpha_i) \tag{1.10}$$

The advantages is a wave length independent depiction of the XRR-scan, which makes a comparison easier.

### Kiessig-Fringes

Fringes occur when a single layer or multilayer are analysed over a certain $q$-range, see Fig. 1.2. The physics is similar to visible light interference on thin and plain mediums. The X-ray beam gets reflected and transmitted at the vacuum/medium interface and again reflected and transmitted at the medium/substrate interface, see Fig. 1.4. The two reflected beams have a path difference, which vary during a scan. The path difference could be calculated out of geometrical assumptions.

$$\Delta = 2t \sin(\alpha_t) \approx 2t\sqrt{\alpha_i^2 - \alpha_c^2}$$

$\Delta$ represents the path difference, $t$ the thickness of the layer and $\alpha_t$ the angle of the transmitted beam, see Fig. 1.2. The approximation for $\alpha_t$ is given by *Snell's- Law*, where $\alpha_t^2 \approx \alpha_i^2 - \alpha_c^2$ for small angles.
Maximum of intensity is reached every time when the path difference is some multiple of $\lambda$, like $\Delta = m\lambda$.

$$2\alpha_{m+1} - 2\alpha_m \approx \frac{\lambda}{t}$$

When the Kiessig fringes are very defined, like in Fig. 1.2, the estimation of the thin film thickness just varies a view percent. To obtain good fringes the maximum film thickness for conventional X-ray source is about $\approx 200$ *nm* for organic materials, [4].

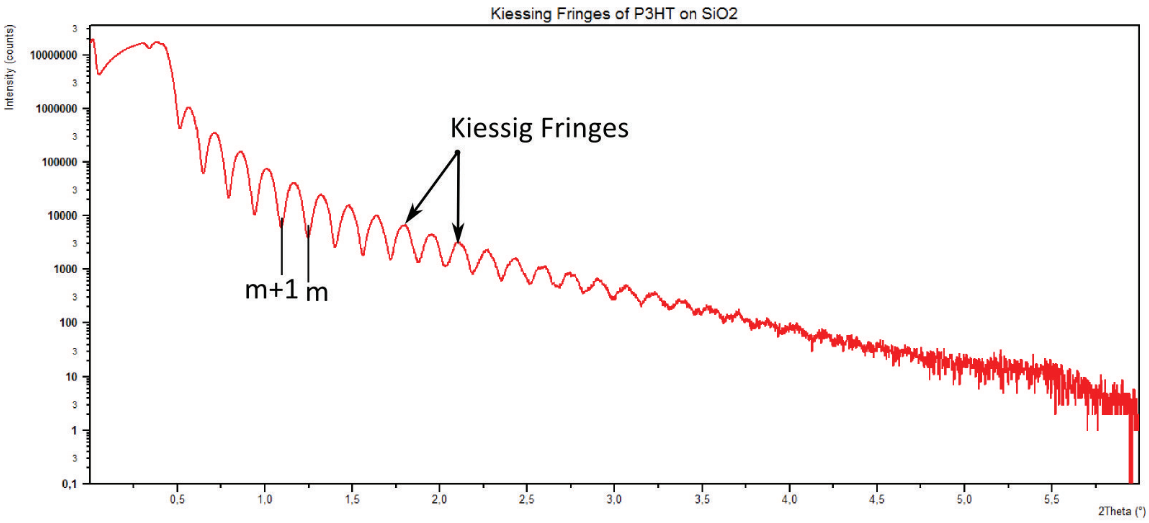

Figure 1.2: A measured P3HT layer on top of native $Si$, where the Kiessig fringes can be seen.

### 1.1.3 Single- and Multilayers

The measured intensity at the detector is connected with the absorption of the material, roughness at interfaces and electron density. How the fringes look in a single or multilayer system depends on the reflection coefficient of every interface.
Reflection and transmission coefficients must be calculated out of the amplitude reflectivity $r$ and transitivity $t$. To do this the *Fresnel Equation* are used. They are based on the continuity of the tangential amplitude of the incident, reflected and transmitted wave. With this boundary condition the *Fresnel Equations* are:

$$r = \frac{\alpha_i - \alpha_t}{\alpha_i + \alpha_t}$$

$$t = \frac{2\alpha_i}{\alpha_i + \alpha_t}$$

*Snell's Law*, Eqn. 1.9 instead gives the relationship between $\alpha_i$ and $\alpha_t$:

$$\alpha_i = \sqrt{\alpha_t^2 + \alpha_c^2 - 2i\beta}$$

For simplification just the reflection from a substrate is regarded with an infinite thickness. To get the required intensities in this case, transmittivity can be neglected and just reflection is needed. Because $r$ is the amplitude reflectivity the absolute square have to be used for getting the reflection coefficient.

$$R = \frac{I_R}{I_0} = |\frac{\alpha_i - \sqrt{\alpha_i^2 - \alpha_c^2 - 2i\beta}}{\alpha_i + \sqrt{\alpha_i^2 - \alpha_c^2 - 2i\beta}}|^2$$

$I_0$ is the incoming intensity from the tube and $I_R$ is the reflected intensity measured at the detector. With Eqn. 1.10 the intensity $I_R$ according to its $q$ dependence is :

$$R(q) = \frac{I_R(q)}{I_0} = \left| \frac{q_z - \sqrt{q_z^2 - q_c^2 - \frac{32\pi^2}{\lambda^2} i\beta}}{q_z + \sqrt{q_z^2 - q_c^2 - \frac{32\pi^2}{\lambda^2} i\beta}} \right|^2$$

$R(q)$ has different region, shown in Fig. 1.3. In most case $\beta$ can be neglected.

- $q_z > q_c$ the $R(q)$ decays like $(\frac{q_c}{2q_z})^4$. This consideration is valid for a perfect plain surface without roughness. XRR-scans with real interfaces have a steeper decay of $I_R(q)$.
- $q_z \approx q_c$ in this region an evanescent wave occurres on the surface of the material, this region is used by the Gracing Incident X-ray Diffraction. The wave can penetrate.
- $q_z < q_c$ it is the total reflection region, where quasi nothing of the X-ray beam is penetrating the material, therefore the reflection coefficient is nearly constant. The plateau below $q_c$, see Fig. 1.3, is determined through the size of the substrate, smaller substrates give a smaller plateau. This can be derived through simple geometrical model, considering the beam hight of the X-ray beam.

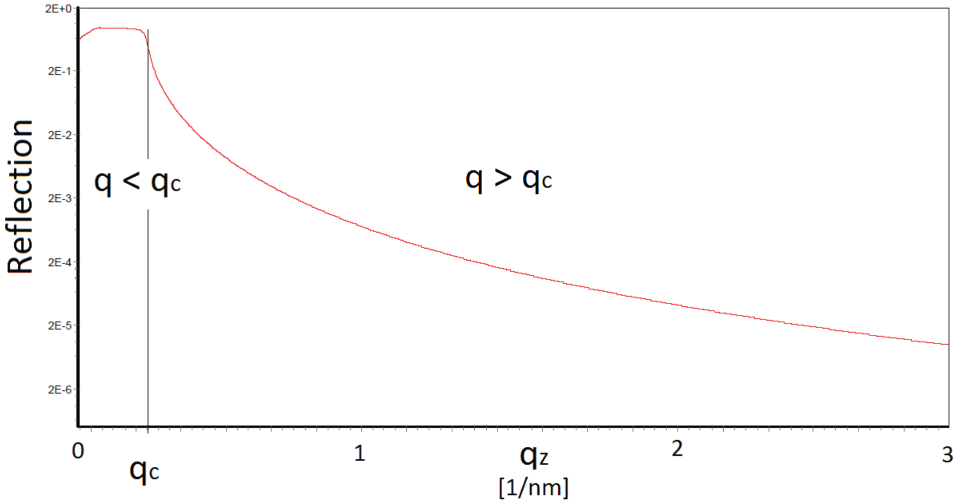

Figure 1.3: Shown is a simulation of reflectivity on a substrate with no roughness. $q_c$ is the critical scattering vector.

### Reflection of Single Layer

If the incident angle is bigger than $\alpha_c$, the X-rays will be also transmitted at the interface. Now a single layer, like in Fig. 1.4, with a finite thickness is regarded. The intensity at the detector depends on:

- Reflection at vacuum/medium interface $r_{01}$
- A part of the beam is goes into the medium $t_{01}$ and hits the interface of medium/substrate $r_{12}$. The beam inside the medium is reflected back to the medium/vacuum interface, where it can leave the material with $t_{10}$. Because this X-rays moved in a medium, a path difference between $r_{01}$ and transmitted and reflected($t_{01}t_{10}r_{12}$ beam have to be included. The phase factor is $p^2 = e^{iq\Delta}$).
- Multiple reflection can occur. The beam is reflected again at the medium/vacuum interface $r_{10}$ and then reflected again at $r_{12}$.

The total amplitude reflectivity is, [2]:

$$r_{Single} = r_{01} + t_{01}t_{10}r_{12}p^2 + t_{01}t_{10}r_{10}r_{12}^2p^4.... \tag{1.11}$$

Where $t_{01}t_{10}r_{10}^{n-1}r_{12}^{n}p^{2n}$ is the term for multiple reflections, for $n \geq 2$. Eqn. 1.11 turn out to be geometric series, which can be simplified with the *Fresnel Equations* and the assumption $r_{01} = r_{10}$ to:

$$r_{Single} = \frac{r_{01} + r_{12}p^2}{1 + r_{01}r_{12}p^2} \tag{1.12}$$

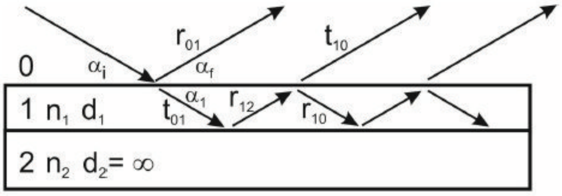

Figure 1.4: A schematic description of the reflected and transmitted beam, [6]

### Reflection from Multilayers

For simplification now multiple reflection events are neglected and just single reflection counts for the reflectivity amplitude $r$. To obtain $r$ the first step is to start at the medium/substrate interface, where the *Fresnel Equations* give:

$$r'_{N,substrate} = \frac{k_N - k_{substrate}}{k_N + k_{substrate}}$$

Similar the to single layers the next layer is considered

$$r_{N-1,N} = \frac{r'_{N-1,N} + r'_{N,substrate}p_N^2}{1 + r'_{N-1,N}r'_{N,substrate}p_N^2}$$

To calculate the reflectivity amplitude $r$ for the whole multilayer system, this method must be recursively continued for all layers. For more detailed derivative, [2] is recommended.

### 1.1.4 Roughness at Surfaces and Interfaces

A schematic description for the effects of roughness is shown in Fig. 1.5. The rough surfaces and interfaces can cause off-specular scattering, this lead to a loss of intensity at the detector side. Through that the $R_{rough}(q) < R_{Fresnel}(q)$ and the XRR-scans decay steeper than in the ideal Fresnel-picture($R(q) \approx q^{-4}$). For small $q$ both curves are nearly the same, but for higher $q$ the roughness causes a big divergence, see Eqn. 1.14.

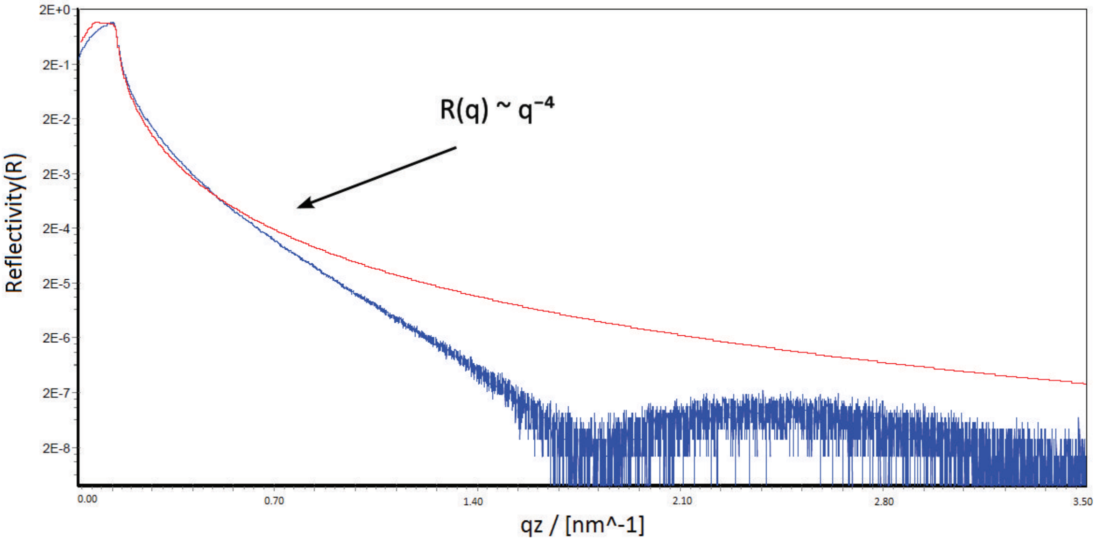

Figure 1.5: A XRR-scan was preformed on native $Si$(blue curve)and compared with a simulation without roughness(red curve).

Now the *differential cross-section* is considered. As it is shown in the appendix in [2], the *differential cross-section* is proportional to the scattered intensity $I_{sc} \approx (\frac{d\sigma}{d\Omega})$. The mathematics is:

$$\frac{d\sigma}{d\Omega} = \frac{r_e\rho_e{}^2}{q_z}\frac{A_0}{\sin(\alpha_i)}\int e^{-q_z^2\langle[h(0,0)-h(x,y)]^2\rangle/2}e^{i(q_xx+q_yy)}dxdy \qquad (1.13)$$

$\frac{A_0}{\sin(\alpha_i)}$ is the illuminated surface area, $r_e$ here the *Thomson scattering length* of an electron. The $\langle e^{iq_z[h(0,0)-h(x,y)]}\rangle = e^{-q_z^2\langle[h(0,0)-h(x,y)]^2\rangle/2}$ is know as the *Baker-Hausdorff Theorem*, [2], which can just be applied if the heigth distrubution is assumed as a *Gaussian-distribution*. The use of the *Gaussian-distribution* implies that very close areas ($A(x, y)$ and $A(x', y')$) are not correlated with each other, [2]. Although a *Gaussian-distribution* model for the height distribution is very unphysical, this simple model display good estimation of the roughness. In Fig. 1.6 an example of an uncorrelated surface is given. The height of the surface is obainted from the average value of the *Gaussian-distribution*. The roughness is estimated through $\sigma_{rms}$ the root mean square deviation and gives a hint how strongly the height varies around the average height of the surface.

With

$$(\frac{d\sigma}{d\Omega})_{Fresnel} = \frac{r_e \rho_e{}^2}{q_z} \frac{A_0}{\sin(\alpha_i)} \int e^{i(q_x x + q_y y)} dx dy$$

and

$$\langle [h(0,0) - h(x,y)]^2 \rangle = 2\langle h^2 \rangle - 2\langle h(0,0) \rangle \langle h(x,y) \rangle = 2\langle h^2 \rangle$$

Equation 1.13 becomes:

$$(\frac{d\sigma}{d\Omega}) = (\frac{d\sigma}{d\Omega})_{Fresnel}\ e^{-q_z^2 \sigma_{rms}^2} \tag{1.14}$$

$\sigma_{rms} = \sqrt{\langle h^2 \rangle}$ is used. The consideration of roughness leads to following conclusion:

- Roughness leads always to a lower intensity. The Fresnel reflectivity $(\frac{d\sigma}{d\Omega})_{Fresnel}$ is reduced by the factor $e^{-q_z^2 \sigma_{rms}^2}$. From the dependence on $q_z$ the effects of roughness getting stronger with an increasing incident angle $\alpha_i$

- A step further to a real interface is the introduction of a non-uniform electron density of layers. Not perfectly sharp interfaces can be described with $R(q_z) = R_F(q_z)\ e^{-q_z^2 \sigma^2}$. '*This illustrates that different models may yield the same reflectivity curves. In other words, reflectivity experiments cannot uniquely reveal the true nature of an interface*', [2].

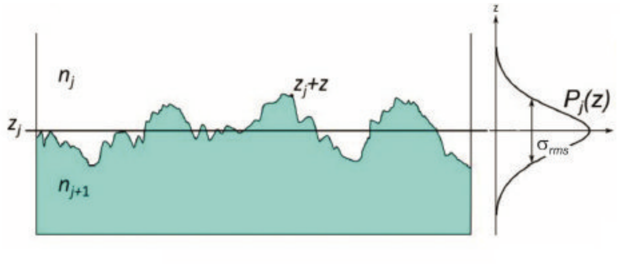

Figure 1.6: Roughness of a surface and the approximation with a Gaussian distribution, [6].

### Example of XRR-Simulation

This example, Fig. 1.7 is out of Metin Tolan, [3]. It shows the effects of surface roughness($\sigma_1$) and interface roughness($\sigma_2$) of a polystyrene(PS) thin film on silicon. The X-ray beam is for small angles($\alpha_i$) very sensitive for the surface, if the roughness there is small, the fringes are very strong in this region. If the surface roughness is increased the XRR-cruve is changed and the strong fringes for small $\alpha_i$ become weaker. When both roughness are high the curve disappears faster.

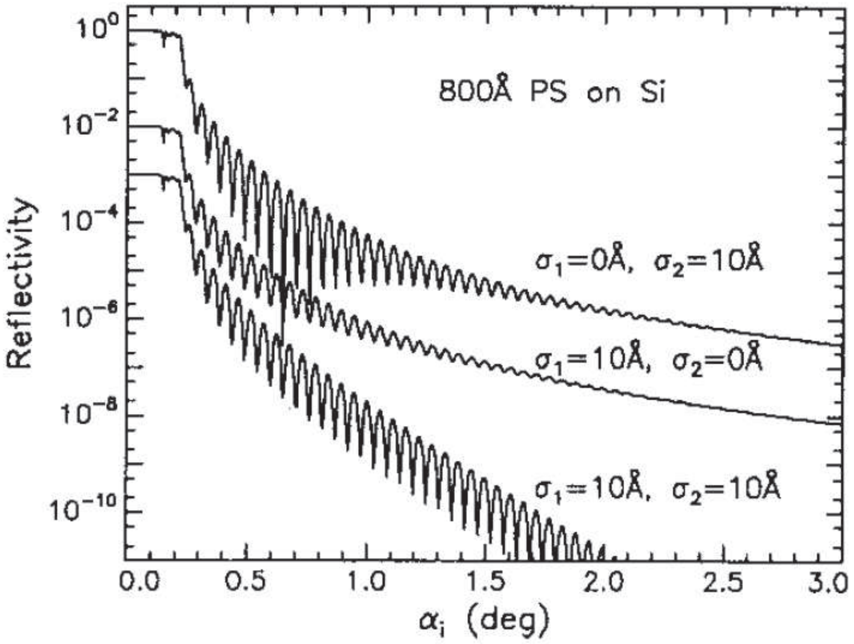

Figure 1.7: Simulations of a polystyrene(PS) layer on $Si$. The effects of surface roughness($\sigma_1$) and interface roughness($\sigma_2$), [3]

## 1.2 Gracing Incident X-Ray Diffraction(GIXD)

A more sophisticated method to investigate thin films on substrates is GIXD. Specular scans are sensitive for out-plane order of materials. Out-plane means that the crystal planes of organics or inorganics is parallel to the substrate surface. This ordering gives Bragg-peaks, which are described with the formula:

$$m\lambda = 2d_{hkl}\sin(\alpha_i) -> \ q_z = \frac{4\pi}{k}\sin(\alpha_i) \tag{1.15}$$

$m$ is the order of the Bragg-peak, $\lambda$ the wavelength of the X-ray, $d_{hkl}$ distance between two $hkl$-planes, $k$ the reciprocal wave vector and $\alpha_i$ the incident angle. Especially when an organic material is deposited the surface energy of the substrates can induce a ordering, which is different for the bulk of the material. To analyse such thin films, a beam is needed, which is nearly parallel to the surface($\alpha_i \approx \alpha_c$), see Fig. 1.8.

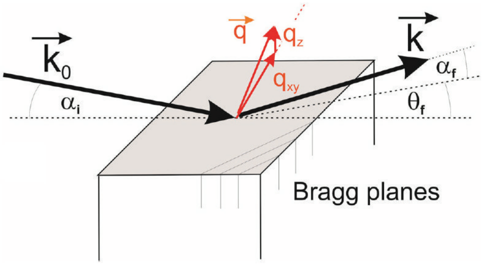

W. C. Marra et al. J. Appl. Phys. (1979)

Figure 1.8: Schematic picture of a gracing incident X-ray diffraction. The X-rays are out of the specular condition and have now also a $q_x$ and a $q_y$ content, [6].

There are two regions for GIXD:

- When $\alpha_i < \alpha_c$ total reflection occurs at the surface, regime of constant reflection. A evanescent wave is created on the surface, with a penetration depth of about $\approx 5 - 10\ nm$, [4]. In this region GIXD is surface sensitive and can maintain the lateral correlation of surfaces.

- The second region for GIXD is, when the incident angles is slightly bigger than the critical angle $\alpha_i > \alpha_c$. Here the penetration depth increases rapidly and is just limited to the absorption of the material, [2]. In good approximation the penetration length($l$) is about $l \approx \frac{1}{\mu}$ for a perpendicular incident beam and is in the order of about $\approx 10^5 - 10^6\ nm$ for organics, [4].

GIXD works with Bragg-scattering vector, but here the scattering vector is composed of a X-, Y-, Z-component. The scattering $q$ is:

$$q = \sqrt{q_x^2 + q_y^2 + q_z^2} = \sqrt{q_{xy}^2 + q_z^2}$$

During the experiment the detector arm is turned around the Z-axis to change the $q_{xy}$ vector in its length, so a scan over a certain range can be preformed and reciprocal space maps are gained with a 1D-detector, Fig. 1.9. The GIXD - map is a 2D map in the reciprocal space, where $q_p$ is plotted on the X-coordinate as the in-plane scattering vector and $q_z$ on the Y-coordiante. The colors are indicating the intensities with blue is low and red is high. The indexation was done by assuming the unit cell of ternaphthalene(NNN).

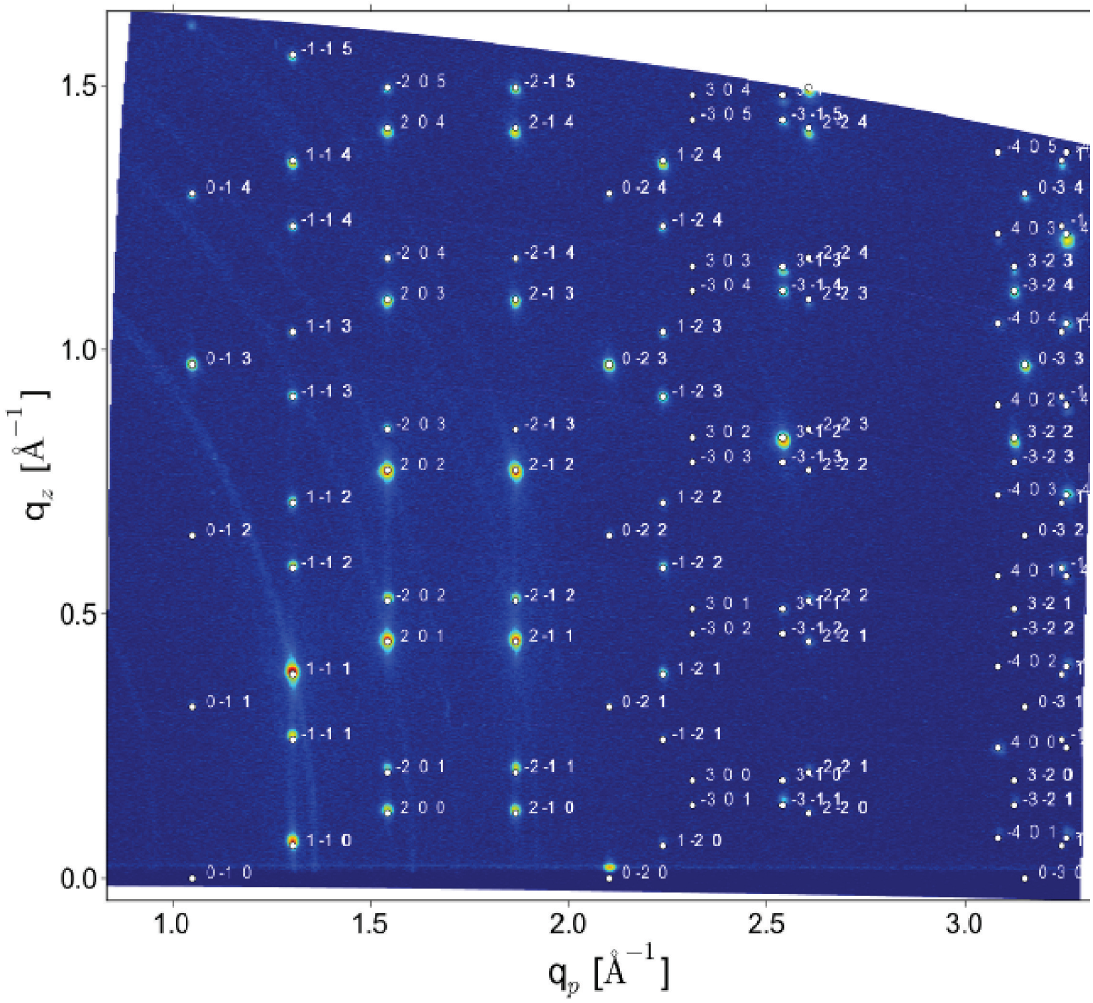

Figure 1.9: A GIXD measurement from ternaphthalene(NNN) with indexation measured at the synchrotron, [7]

## 1.3 Neutron Reflectivity(NR)

Scattering experiements are often done with X-rays radiation as alternative neutrons could be used too. In most of the cases also the same models are applied to describe Neutron Scattering, Neutron Reflectivity, Small Angel Neutron Scattering,... In case of NR the obtained data is qualitatively the same as the XRR-data, but of course there are differences.

**X-rays** are Photons. What means they are Bosons and don't have a magnetic moment($\mu_M$)

and mass.

Photons which meets an atom can undergo the following events, [8]:

- Elastic scattering - no change of energy(**Thomson Scattering**)
- Inelastic scattering - some energy of the photon is transferred to an electron, which is usually excited into a higher orbital or can overcome its bounding energy(**Compton Effect**)
- Absorption is consisting of elastic scattering, inelastic scattering and the photo effect. The incoming photon is extinguished, but another photon can be emitted, with a lower energy(**Fluorescence**)

**Neutrons** are particles and have a mass of about $m_0c^2 = 939MeV$, a spin of $\frac{1}{2}$ and a magnetic moment $\mu_m$. The charge free nature of the neutrons enable them to penetrate through the electron shells of the atom and scattering events at the nucleus are possible. The propability of a scattering event depends on the size of the core(mass number), on the unpaired spins and the magnetic moment of the core. Because of their spin, neutron can also interact with the unpaired spin of electrons in shells.

NR and XRR experiments are qualitatively the same. Also in NR-Scans for non-magnetic materials a total reflection regime, Kiessig-Fringes and a $\frac{1}{q^4}$ decay exists.

The interaction of neutrons with atoms or matter can be summed up in:

- Elastic scattering - no change of energy(NR)
- Inelastic scattering - measurment of the dispersion relationship of Phonons in solids
- Nuclear reactions, like absorbtion, interaction with the magnetic spin of the core or unpaired spins of protons and neutrons.

### 1.3.1 Scattering Length Density

As mentioned above the main difference between neutrons and X-rays lays in the interaction with the matter. Therefore the scattering length density for neutrons varies more from element to element and isotope to isotope, than it does for X-rays.

The scattering length($b$) is a quantity, which describes the intensity fluctuation of a wave after a scattering event in a certain observation direction **u** and the differential cross section can be directly calculated out of $b$, [9]:

$$(\frac{d\sigma}{d\Omega})(b(\mathbf{u})) = |b(\mathbf{u})|^2 \tag{1.16}$$

A scattering event on a spherical symmetric scatterer, the total scattered intensity is proportional to $\sigma_{scat,tot}$ and is an integral over the surface of a whole sphere, [9]:

$$\sigma_{scat,tot} = \int\int |b(\mathbf{u})|^2 d\Omega$$

Because a spherical symmetric scatterer is regarded the scattering length is constant over the surface area $b(\mathbf{u}) = b$, it follows

$$\sigma_{scat,tot} = 4\pi b^2$$

To consider the whole interaction with a medium absorption have to be included $\sigma_{abs}$. Total cross-section of a spherical symmetric scatterer is:

$$\sigma_{tot} = \sigma_{abs} + \sigma_{scat}$$

The scattering length density($\rho$) is just the average over the scattering length in a certain volume:

$$\rho = \frac{1}{V}\sum_j b_j$$

This is a very general model and is out of [8] and [9] and are also valid for X-rays. The scattering length for neutrons is often not spherical symmeteric, what means that $b$ depends on the observation direction $u$ and is not uniformly distributed anymore over the whole solid angele. Generally the scattering length for neutrons is $b(\mathbf{u})$ for a specific observaion direction **u**, [9] and have to be calculated like in Eqn. 1.16. Neutrons are influenced by the interaction of their spins with the spin of the core and magnetic moments. But another important parameter of the $b(\mathbf{u})$ is the scattering on not spereical symmetric cores, which occures especially for higher mass numbers.

### Consideration of X-rays

Assuming a spherical symmetric scattering event is a way of looking on the interaction of X-rays with matter, but it is nevertheless a rough assumption. A step further is to include the atomic structure factor in this consideration. The scattered intensity of an Bragg-peak is determined by the atomic structure factor($f(q)$), [4], and is

$$f(q) = \int_{atom} \rho_e(r)e^{-iqr}d\mathbf{r}$$

It is known, that the intensities are depending on the Fourier transformation of the electron density $\rho_e(r)$, a scattering event on a single atom :

$$\frac{I_{sc}(\mathbf{q})}{I_0} = \frac{d\sigma}{d\Omega}(\mathbf{q}) = r_e^2|f(q)|^2 = b^2(q)$$

$I_0$ is the incoming intensity and $I_{SC}$ scattered one. Out of this relation, the scattering length for X-rays for an atom is:

$$b(q) = r_e f(q)$$

$r_e$ is the *Thomson scattering length* again, $q$ is the reciprocal scattering vector, which also give the observation direction. The polarisation factor is neglected. This expression is called *Thomson scattering.* If the incident beam has an energy to come in resonance with the electrons in their orbitals. Then the atom structure factor must be corrected, [8] or [9] for further information.

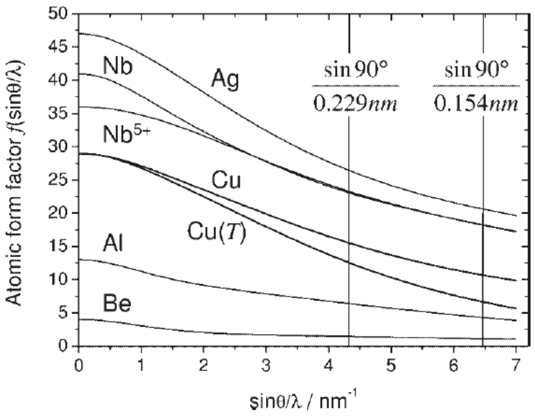

Figure 1.10: Atomic from factor of different elements and their dependence on the wave length of a X-ray beam and incident angle, [4]

### Consideration of Neutrons

To determine the scattering length for neutrons is far more difficult than it is for X-rays. The reason is that an isotopic scattering length is not valid any more, $b$ depends in an unsymmetric way on the interaction with the nucleus, [8]. Because of the magnetic moment($\mu_m$) and spin, neutrons are also sensitive for the magnetic moment of the nucleus and spin. Therefore $b$ depends on the direction of the nuclear spin, [8]. Also the scattering cross section splits up into two components:

$$\sigma_{scat} = \sigma_{coherent} + \sigma_{incoherent}$$

Only $\sigma_{coherent}$ have information about the structure. The incoherence $\sigma_{incoherent}$ is caused be a missing phase relation between the incoming and scattered beam and it is correlated to the disorder of the ensemble, [9]. To simplify this case a ensemble of $N$ identical particels is regarded, [8]:

$$\frac{d\sigma}{d\Omega}(\mathbf{q}) = \sum_{j,k=1}^{N} \langle b_j b_k e^{i\mathbf{q}\mathbf{r}_{jk}} \rangle$$

Now the indices have to be considered. The values $b_j$ and $b_k$ depend on the given isotope and spin state, [8]. No interference is gained when $j = k$, that means the sum is splitted up into two parts, where $j \neq k$ and $j = k$. $\langle b_j b_k \rangle$ becomes:

$$j = k : \langle b_j b_k \rangle = \langle b_j^2 \rangle = \langle b^2 \rangle$$

$$j \neq k : \langle b_j b_k \rangle = \langle b_j \rangle \langle b_k \rangle = \langle b \rangle^2$$

The differential cross section is now:

$$\frac{d\sigma}{d\Omega}(\mathbf{q}) = \langle b \rangle^2 \sum_{j,k=1}^{N} e^{i\mathbf{q}\mathbf{r}_{jk}} + N(\langle b^2 \rangle - \langle b \rangle^2)$$

The substitution of $N\langle b \rangle^2$ is necessary, because the sum $\sum_{j,k=1}^{N} e^{i\mathbf{q}\mathbf{r}_{jk}}$ still runs over all indices, which includes also $j = k$. The first term considers the interference and is called the coherent cross section. The second term is just diffusive scattering and named incoherent cross section.

The scattering length is averaged over al isotopes in the ensemble. In this derivation the spin state is independent of the position of the scatterer, [8].

So the coherent term looks like:

$$\sigma_{coherent} = 4\pi \langle b \rangle^2$$

and the incoherent term is:

$$\sigma_{incoherent} = 4\pi(\langle b^2 \rangle - \langle b \rangle^2)$$

In table, Tab.1.2 the scattering lengths are listed for different elements and isotopes. Tab. 1.3 shows the coherent and incoherent cross section of some important elements. They are obtained out of experiments:

Table 1.2: Scattering length($b$) for light elements, [8].

| [H] Scattering length | $^1H$ | $^2H$ | $^{12}C$ | $^{16}O$ |
|---|---|---|---|---|
| $b(10^{-14}m)$ | $-0.38$ | 0.66 | 0.66 | $0,58$ |

Table 1.3: Cross-section of different light elements. $\sigma_{coh}(10^{-28}m^2)$ is the coherent cross section, it carries all information and $\sigma_{incoh}(10^{-28}m^2)$ is the incoherent cross section, it is considered as back round and don't have any information about structure of the investigated material, [8].

| [H] Isotope | Nuclear Spin | $\sigma_{coh}(10^{-28}m^2)$ | $\sigma_{incoh}(10^{-28}m^2)$ |
|---|---|---|---|
| $^1H$ | 1/2 | 1.8 | 79.7 |
| $^2H$ | 1 | 5.6 | 2.0 |
| $^{12}C$ | 0 | 5.6 | - |
| $^{14}N$ | 1 | 11.6 | 0.3 |
| $^{16}O$ | 0 | 4.2 | - |

### Advantages of Neutrons

- The variance of the coherent cross section is even for elements, which are close in the periodic system big, see Tab. 1.3. Compared with X-rays, it is so possible to analyse materials with a very similar electron density. That is a big advantages, when multilayer samples must be analysed. With X-rays it could happen, that layers are too similar in scattering length density and could therefore not be resolved. So neutron reflectivity gives a very good alternative for resolving polymer layers on defined substrates.
  Additionally the big difference of scattering length density from $C$ and $N$ is an invitation to probe proteins and other complex biological structures with neutrons.
- Tab. 1.2 mentions the scattering length for $H_1$ and $D_2$. To increase the sensitivity of neutrons for a certain material or structure it is possible to substitute $D_2$ instead of $H_1$ to increase the scattering length density. This technique is widely used in Soft Matter Physics and a lot of important breakthroughs were made this way in understanding the conformation of polymers in the melt or amorphous solids, [8].
- Their spin and magnetic moment makes them sensitive for the magnetic structure of materials and enables investigations.

## 1.3.2 Neutron Sources

One big disadvantages of neutron experiments is that they are very expensive hence there are just a few facilities in the world, where such experiments could performed. Additionally the flux of the incoming beam is between $10^{14} - 10^{17} \frac{neutron}{cm^2 \cdot second}$, [10] depending on the source, so a experiment could take several hours. This is also the true for NR-experiments. Compared with the synchrotron, where the flux is about $10^{16} - 10^{22} \frac{photons}{cm^2 \cdot mr^2 \cdot second \cdot (0.1\% bandwidth)}$, neutron experiments, are time-consuming. But nevertheless there are some work arounds. It is quiet common, especially in NR-experiments to deuteraed the polymers to increase $\frac{d\sigma}{d\Omega}(\mathbf{q})$ not only for the contrast, but also to shorten the measuring time.
Worldwide the neutron facilities of the next generation tend to a higher and higher neutron flux, the J-PARC is one of them. In Fig. 1.11 all scientific reactors for neutron scattering are listed.

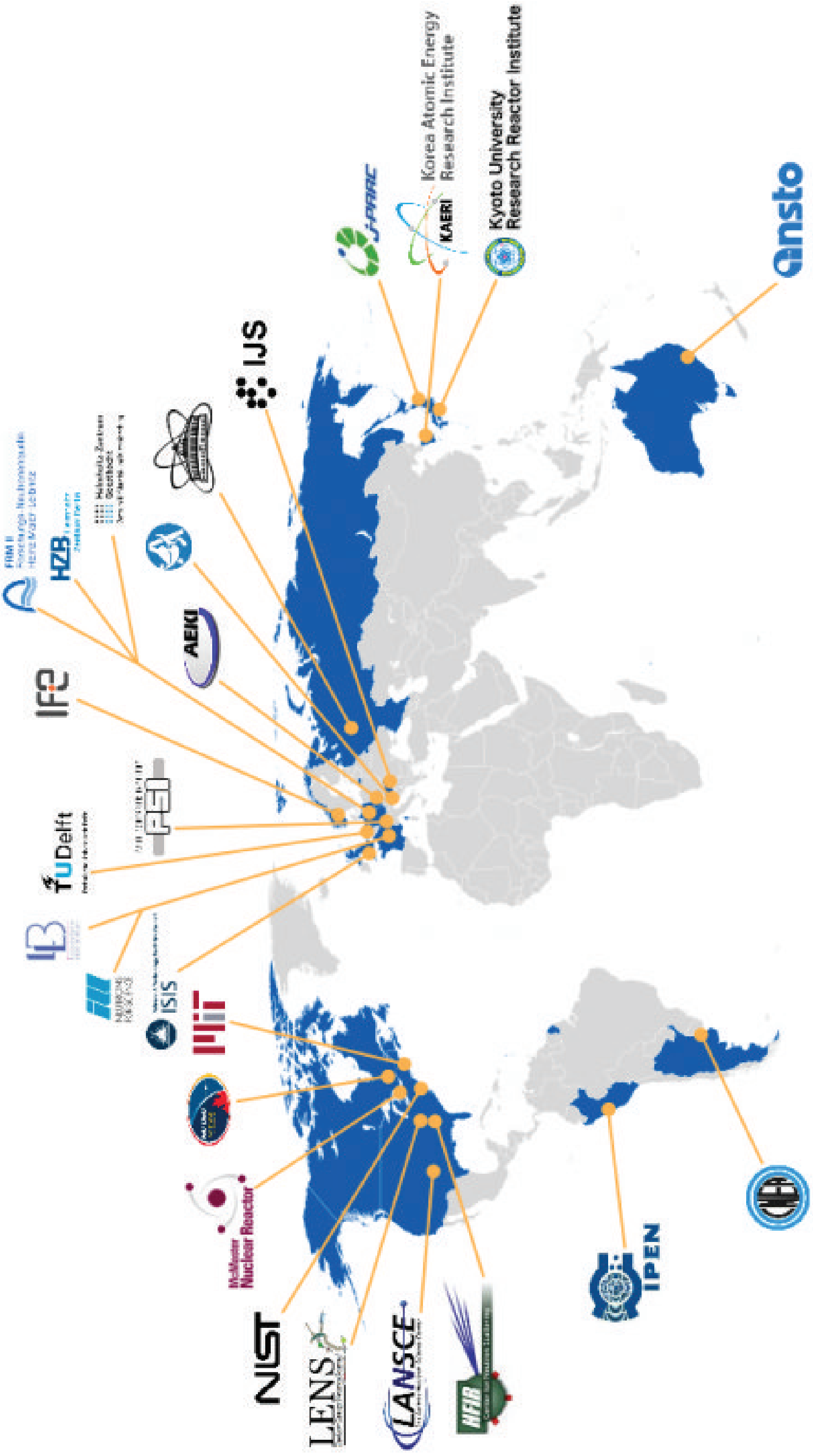

Figure 1.11: World map of all the research neutron facilities in the world. More over 20 exists, [12]

### Research Reactors

These research reactors have a far lower energy production than conventional nuclear power plants. As example the research rector in Garching, FRM II is mentioned. FRM II has a power of 20 $MW$, [13]. In the FRM II fuel cells are used, depicted in Fig. 1.12 the principal concept is shown.

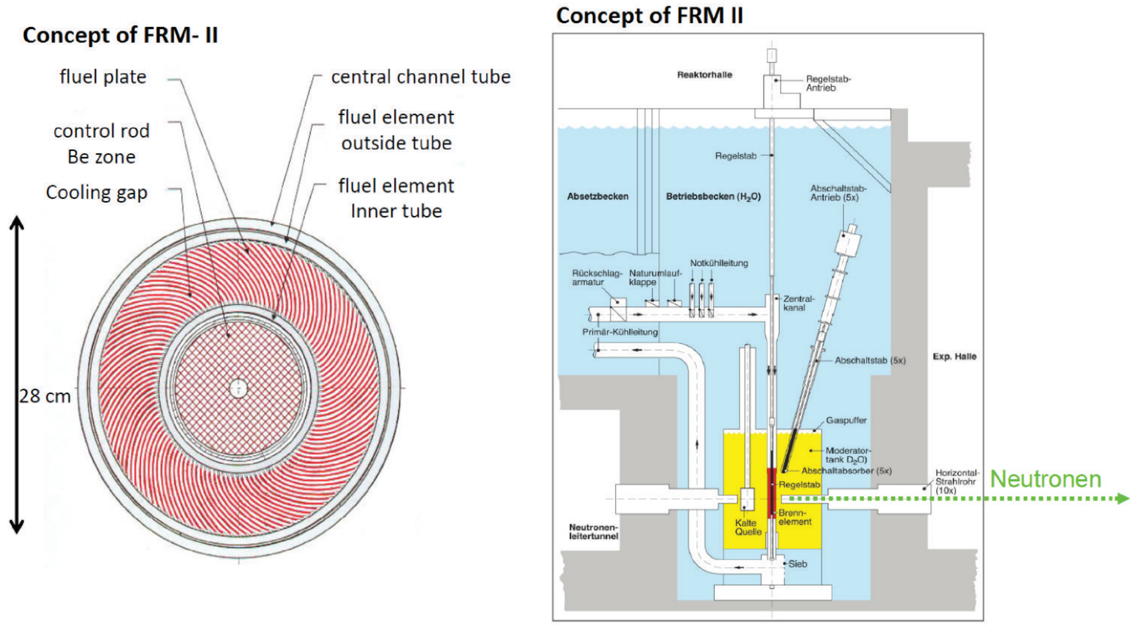

Figure 1.12: A fuel cell from FRM-II. The evoluted fuel plates guarantee a homogeneous flow of cooling water. Right is the reactor of FRM II, [13].

This fuel cells are enriched with $Uranium_{235}$( 20%) the evolute shape of the fuel plates optimize the cooling with light water $H_2O$, [13]. The reaction is following:

- Slow neutron are absorbed by the $U_{235}$. $U_{236}$ is by far less stable and the nucleus cracks into parts.
- Fission of the $U_{236}$ produces high speed neutron, which leave the fuel cell, but get reflected( 30%), [13] by the heavy water $D_2O$ in the moderator tank, which surround the fuel cell.
- The advantage of the heavy water is the low absorption coefficient for neutrons. So the unreflected neutrons travelling through the heavy water and losses their energy. See Fig. 1.13 for the flux of thermical neutrons.
- Into the moderator tank different jet tubes lead the neutron to the beam lines.

Fig. 1.13 shows the distribution of the thermical neutrons in the moderator around the fuel cell. The jet tube are located in around the fuel cell and guide the neutrons to the beam lines. Beside the thermical neutrons, also ulra cooled or hot neutrons are in the moderator, which have a flux maximum at a different distance. Jet tube can be placed at the flux maximum of a certain neutrons ensemble, to guide those to the experiment.

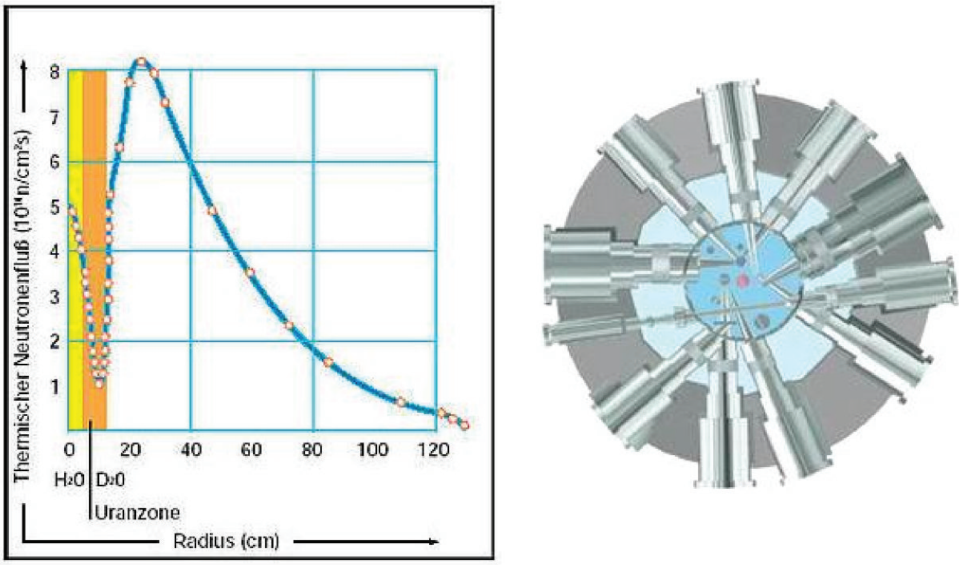

Figure 1.13: Neuron spectra of FRM II on the left and the jet tubes of FRM II on the rigth, [14]

**Spallation Source**

Another possibility is to use the phenomena of spallation to produce neutrons. Here charged particles(protons) are accelerated to a very high energy, usually done in a linear accelerator first and secondly in acceleration ring. When the proton has enough energy to overcome the Coulomb barrier of the nucleus, the proton penetrates the core. The core itself is very closed packed with protons and neutrons. Through inelastic scattering and Coulomb interaction the penetrating proton can transfer its energy to the nucleus and excite it into a higher state. It is also said in particle physics that the nucleus is heated up, see Fig. 1.14.

To get rid of the extra energy, the nucleus evaporates particles like neutrons. When a heavy target is used the nucleus evaporate $20 - 30$ neutrons, [15]. As heavy targets mercury, lead and tantalum are used.

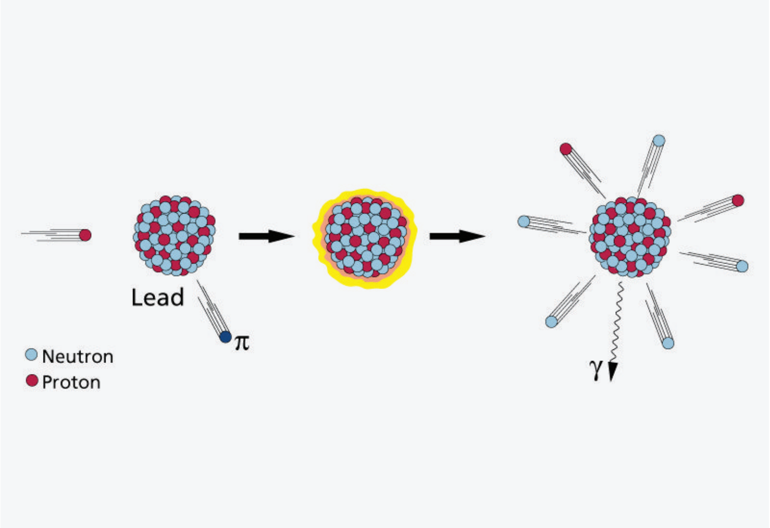

Figure 1.14: Spallation of a heavy core, [15].

The incoming proton beam has so much energy that the target, like mercury in J-PARC has to run in circles to prevent the reactor from heating up. The reactor itself is shown in Fig. 1.15. It is made very massive, so the mercury in- and outlet have about 10 *cm* in diameter, the whole reactor unit itself is shown in Fig. 1.15, right.

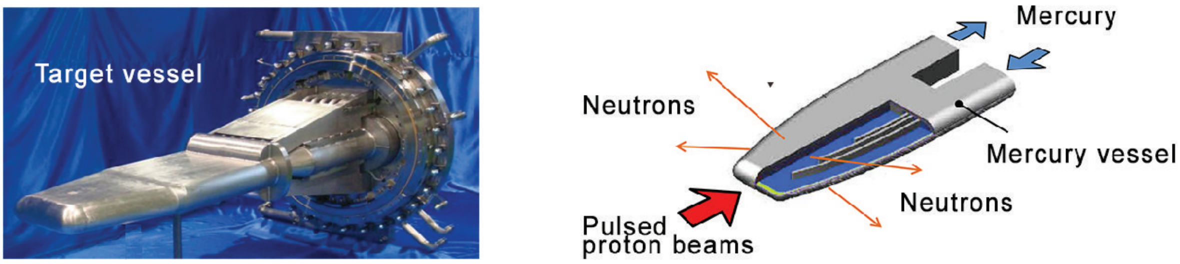

Figure 1.15: Reactor of J-PARC. The mercury must be circulated in a cooling circle, because of the high energy of the incoming proton beam, [16].

### Time of Flight

Especially in neutron scattering a knowledge of the energy is indispensable. There are two methods to determine the energy of neutrons:

- Analysers(crystals), like for X-rays
- Time of flight method

The spallation source in Japan Particle Research Center(J-PARC) for example is pulsed by 25 $Hz$, [16]. Every 4 $ms$ a bunch of neutrons with a dispersive energy hits the sample and get scattered into the detector. The time of flight method do nothing else, to measure the time delay between one measuring point before the sample and when the neutron hits the target. Out of this time delay the corresponding $q$-vectors can be determined, see Fig. 1.16.

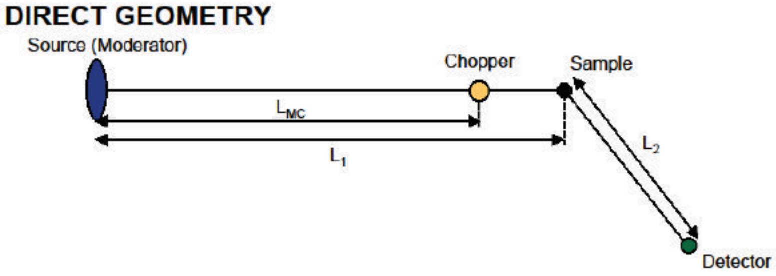

Figure 1.16: Time of flight method for neutrons, [17]

The measuring method in J-PARC for NR is very different from that for XRR. By XRR coherent X-rays are used and the reciprocal scattering vector($q_z$) is changed via changing the $\theta/2\theta$-angle for scanning a certain range. With an energy dispersive source every bunch of neutrons itself has a $q$-range, because of their different velocities. For scanning a certain $q$-range the incident angle($\alpha_i$) has to be changed just a few times, an example is given in Fig.1.17.

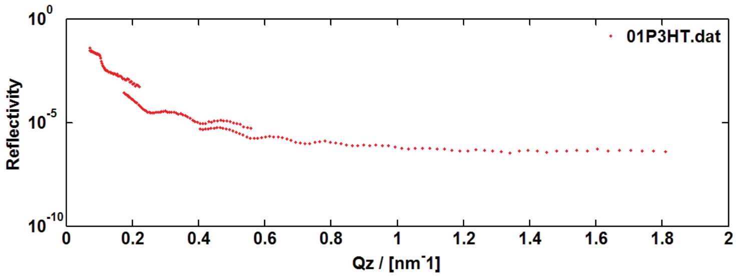

Figure 1.17: Neutron reflectivity scan of P3HT on native-$Si$.

### Japan Particle Research Center (J-PARC)

It is a relative new facility in Japan. The protons for spallation are first accelerated in a linear accelerator and then led in a small synchrotron of 3 $GeV$, see Fig. 1.18. J-PARC can provide neutrons and muons for the material and life science facility with the small synchrotron of 3 $GeV$ and neutrinos and kaons with the main ring 50 $GeV$ for elementary particle physics experiments.
Because the electron density of the used polymers P3HT- Poly(3-hexylthiophen-2,5-diyl)

and F8BT-Poly[(9,9-di-n-octylfluorenyl-2,7-diyl)-alt-(benzo[2,1,3]thiadiazol-4,8-diyl)] for the organic solar cell was to similar. It was not possible to separate both polymer layers sufficiently with XRR in our lab, but that was necessary to get some reliable information about the roughness at the interface. It was possible to see a tendency of an increase in interface roughness, but it was a pure qualitatively conclusion, see Sec. 3.2.
The only alternative was NR at J-PARC. The experiments were performed at the beam line SOFIA(Soft Interface Analyser). The advantages was that J-PARC has a quiet high flux of neutrons and the beam line has a $2D$-scintillator as detector. Via this $2D$-detector is was possible to measure NR and off-specular data at once. The complex of J-PARC is depicted in Fig. 1.18, [16]
Other characteristic data of SOFIA is listed below, [16],

- The incident neutron wavelength is about: $0.2nm < \lambda_{neutron} < 0.88nm$
- The maximum range is $2\theta = \ 6°$
- Observable reflectivity is about: $R = \ 10^{-7}$
- Duration time:
  - Deuterated polymer $(Q < 1nm^{-1}, R < 10^{-4}) : 5min$
  - Deuterated polymer $(Q < 2nm^{-1}, R < 10^{-6}) : 20min$
  - Deuterated polymer $(Q < 4nm^{-1}, R < 10^{-7}) : 1h$
  - Hydrated polymer $(Q < 2nm^{-1}, R < 10^{-7}) : 2h$

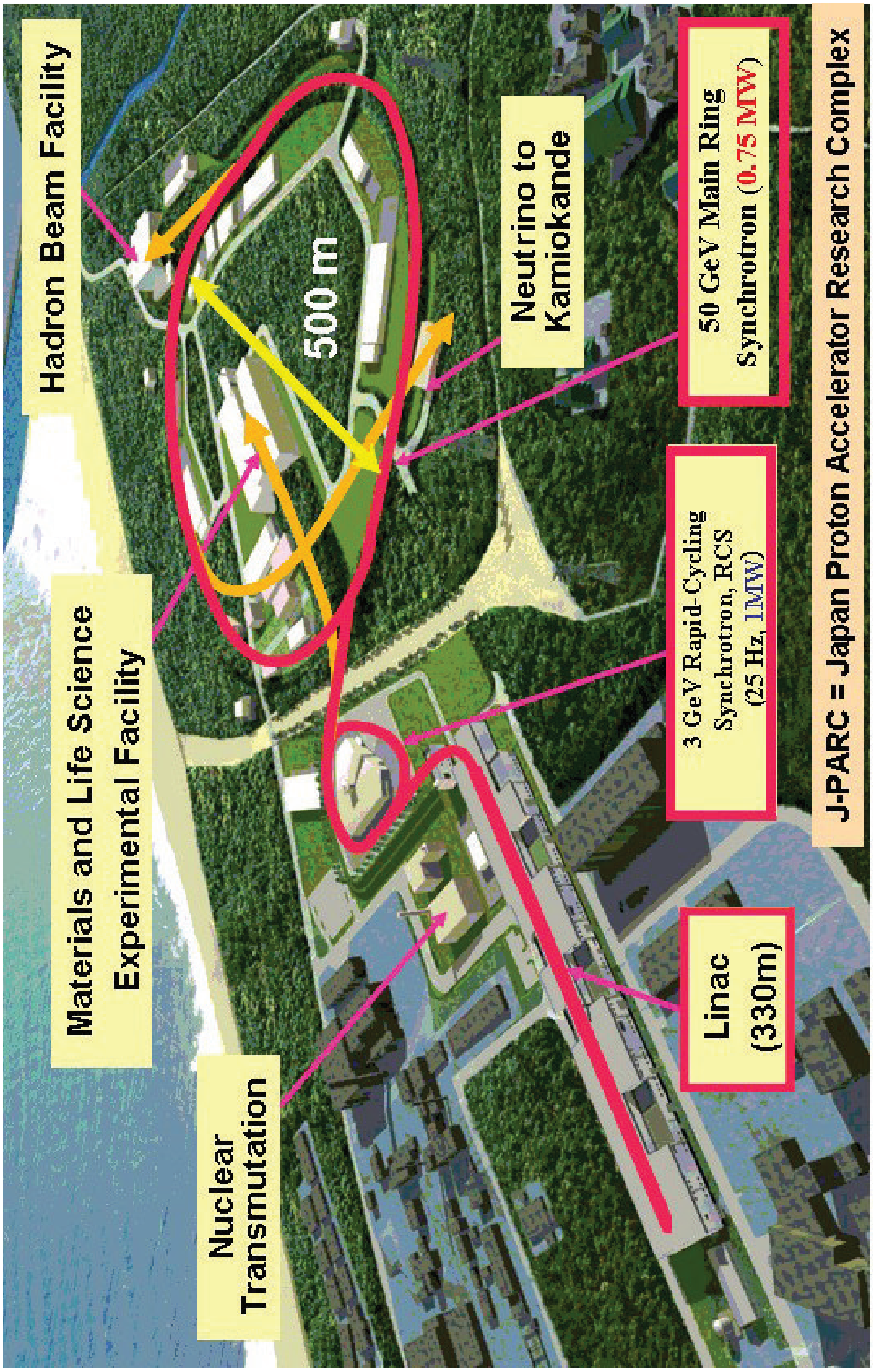

Figure 1.18: Whole research area of J-PARC, [16]

## 1.4 Materials

The materials of choice for organic solar cells are those with a high absorption of light, high exciton generation, good mobility and stability. Conjugated polymers are one big family of those. They were discovered in the 1970's, [18]. Conjugated means for a chemist, that the p-orbital is delocalised over the whole molecule and an electron in such a orbital can move with an high mobility, [18]. A simple example is the benzene ring, where the six $p_z$- orbitals form a $\pi$-orbital above and under the $\sigma$ bound, see Fig. 1.19. The other big group are small molecules, like fullerene($C_{60}$), oligomere or dye molecules. Dye molecules have optical properties, which can be tuned by adding other molecules at their ends or replacing the inorganic element through another. Through that the band gap could be influenced, what means that the absorption maximum can be shifted in the more red region or more blue region.

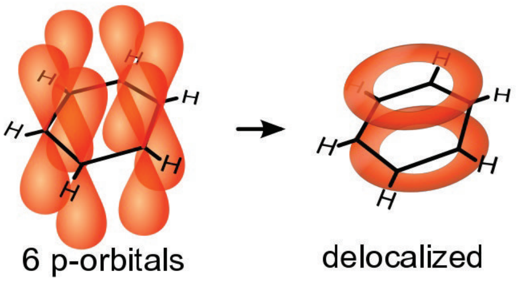

Figure 1.19: The $p_z$ orbitals of the carbon atoms in the benzene ring form $\pi$-orbitals above and below the ring, [19]

### 1.4.1 Conjugated Polymers

As the name implies polymers consisting of a basic unit the monomer, see Fig.1.20, which is synthesized with the same monomer again to long chains, the polymers. For the chemical, optical and electrical properties the chemical structure of the monomer is of importance. The mechanical, thermodynamic and structural properties depend more on the molecular weight(chain length) and the arrangement of heads and tails.

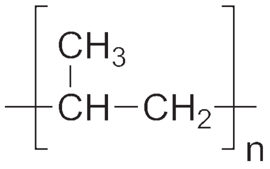

$$\left[ -\underset{}{\overset{CH_3}{\overset{|}{CH}}}-CH_2- \right]_n$$

Figure 1.20: Monomer unit of polypropylene, [20].

The properties of polymers are not so easy to correlate to length or the chemical structure. For example, the mobility is also effected by the chain length and the thermodynamic properties also depend on the length of the alkyl side chain, [21]. It should be mentioned the this is just rough introduction in polymers and there no claim

of completeness.
The arrangement of head and tails effects the structural order strongly. Therefore it is necessary to distinguish, how the monomers are set together.

- **Head(H)** is the side of the monomer, where the chemical rest(R) is, see Fig. 1.21
- **Tail(T)** is consequently on the other side

The different arrangements are shown in Fig. 1.21, because of their high effect on ordering the polymers are divided in regioregular(RR) and regioirrregular(RRa).

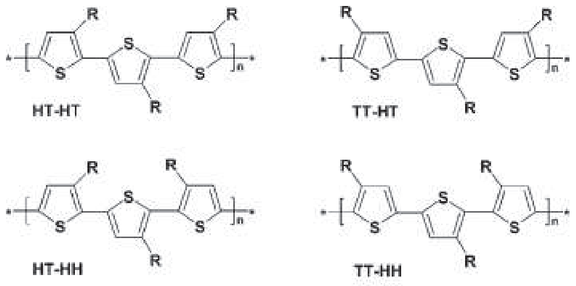

Figure 1.21: Possible arrangements of head and tail in polythiophenes. The head is there were the molecular rest(R) sits, [22].

### HOMO and LUMO of Conjugated Polymers

In organics the HOMO is stand for *Highest Occupied Molecular Orbital* and the LUMO for *Lowest Unoccupied Molecular Orbital.*

### Charge Mobility($\mu$)

For the efficiency of an organic solar cell the charge mobility is very important. The $\mu$ of holes $\mu_h$ and electrons $\mu_e$ should be in the same range to guarantee a good charge transport and charge separation at the interface. Here only the simplest model for charge mobility will be discussed:

$$v_{e/h} = \mu_{e/h} E$$

$v_{e/h}$ is the velocity of holes or electrons and $E$ is the electric field. The models for $\mu_{e/h}$ with regarding the $E$-field- or $T$-dependence are no topic of this discussion.

### Measurement of $\mu$

For a satisfying description of organic solar cells the bulk mobilities of the charges are needed. Time of Flight(TOF) is a mehtod, which can prevent such informantion, as long the mobilities are low, [23]. The principle is the following: A short pulse of light creats excitons on one side of the sample, see Fig. 1.22 simultaneously a voltage is applied from one end of the electrode to the other, which separates the charges. One charge species will discharge directly at the front electrode, whereas the second travel through the organic material. The directly discharged charges cause a displacement current, which can be detected. When the charges in the organic material reach the other electrode the displacement current drops to zero and the time delay($\tau_t$) is determined, [23].

$$\tau = \frac{L}{\mu E} = \frac{L^2}{\mu V}$$

$L$ is the distance between the electrodes and $V$ is the applied voltage.

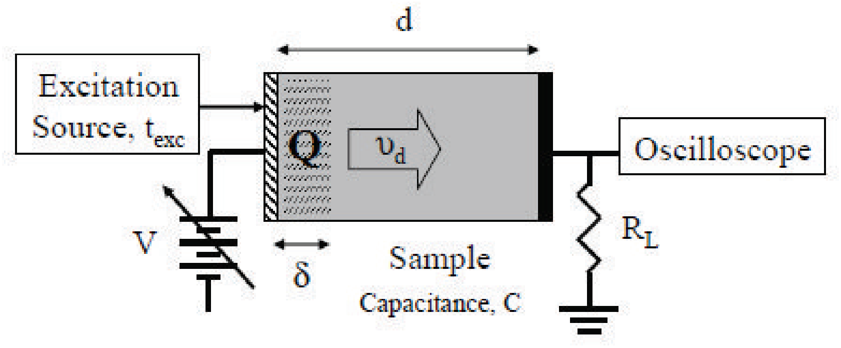

Figure 1.22: Measurement setup for charge mobility, [24].

### Photoluminesecence Quantum Efficiency(PLQE)

Photoluminescence is a result of the recombination of carriers. When light hits a photoactive polymers it is absorbed and generates a electron-hole pair(exciton), which is normally located at the back bone of the chain. Here the electron is excited in the LUMO and a hole is generated in HOMO. Excitons are electrically neutral, have a certain life time and move statistically around on the polymer. They can recombine again in a radiative way.
There are also non-radiative ways. Coupling between chains, can separate the exciton, so that the negative and positive charges are located on different polymer chains. This charge transfer to the other chain breaks the exciton and the charges are not neutral any more. Through that a distortion occurs in the polymers and polarons are formed. Subsequently these polarons are transformed into charged bipolaron and can decay in a non-radiative way, [23].
Out of the combination of absorption and PLQE data it can be determined how effective the material produces exciton pairs.

### Measurement of Photoluminesecence Quantum Efficiency

The exciton is caused by laser light, which hits the sample with very short pulses($ns$). Recombined excitons emit light randomly. For a PLQE the emitted light have to be collected. That's why the sample is placed in a sphere, where the inner surface has a very high reflection coefficient for light. The reflected light of the sphere is then focused into a detector.

These measurement is quiet sophisticated and can supply much more information about the material than it is mentioned above, for example vibronic states could be identified or different distortions, but the explanation would here lead to far. So only a schematic view over the measuring setup is given.

### Glass Transition Temperature($T_g$)

The glass transition marks a transition state between the liquid and the solid phase. In the glass phase the material has some short range order like in a liquid, but its viscosity is higher than in the liquid phase. That means, the material is solid, but highly amorphous, like glass.

At $T_g$ the movement of the molecules are enhances and therefore the materials are elastic. The enhanced movement compared to a solid are described by the concept of **cooperativity**, [25].

Experimentally $T_g$ could be observed by cooling the sample and constantly measuring the specific heat capacitiy($c_p$) or the thermal expansivity. If the material is cooled from the liquid phase with a constant rate the glass transition can be seen, Fig. 1.23, but if the cooling rate is change the $T_g$ can be shifted. That means the glass transition is not at a fix temperature like the crystallistion temperature($T_m$). $T_g$ depends strongly on the cooling rate and the sample history and therefore the glass transition is not a real thermodynamical phase transtion at all. It is a kinematical transition, where the sample is going through a lot of local energy minimums during the cooling.

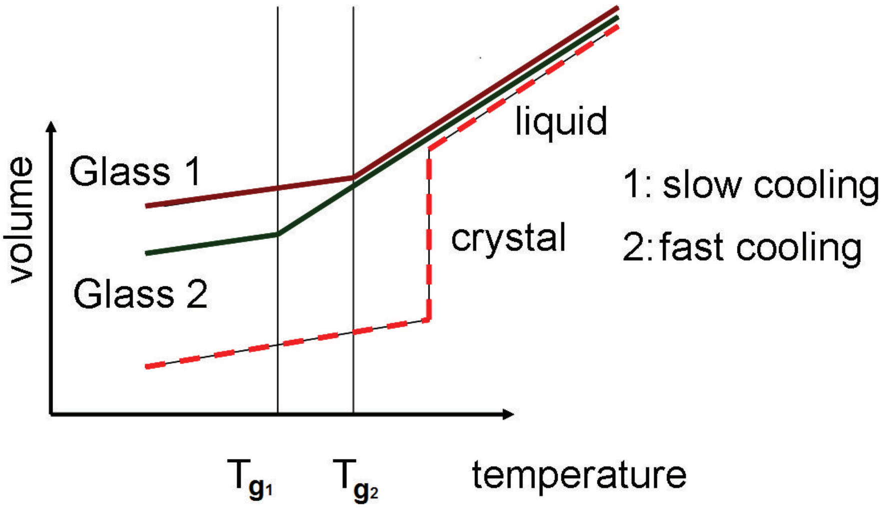

Figure 1.23: The glass transition measured through the volume expansion. $T_m$ crystalistion temperature, $T_{g_1}$ is for slow and $T_{g_2}$ fast cooling, [26].

### Measurement of the Glass Transition Temperature

Differential scanning calorimeter(DSC) measure the heat flow during cooling and heating a sample up. The change of the heat flow marks a phase transition. Experimentally it is realised by observing cosntantly the temperature of two sample holders. One holder is empty the other one is filled with the material. Both holders are kept at the same temperature during heating or cooling. The holder with the sample will need a higher heat flow, especially at phase transitions or transitions in general. The increase of heat flow is observed as a bump in the $c_p$ curve.

## 1.4.2 P3HT - Poly(3-hexylthiophen-2,5-diyl)

P3HT($C_{10}H_{14}S_1$) is a widely used material in organic electronics and in organic solar cells it is used as an electron donor(n-Type). It's monomer unit is depicted in Fig. 1.24. It's solvable in the most common solvents like, chloroform, chlorbenzene, toluene and xylene. P3HT is known to form organized lamellar structures, with a Bragg-peak for $CuK_\alpha$ at $2\theta = 5.4°$, which is corresponding to an intermolecular spacing of $d = 16.36$ Å and a peak at $2\theta \approx 28°$, which comes from the plan parallel distance between the polythiophene rings($d = 3.7 - 3.8$ Å), [23], the lamellar structure is shown in Fig.1.24, right.

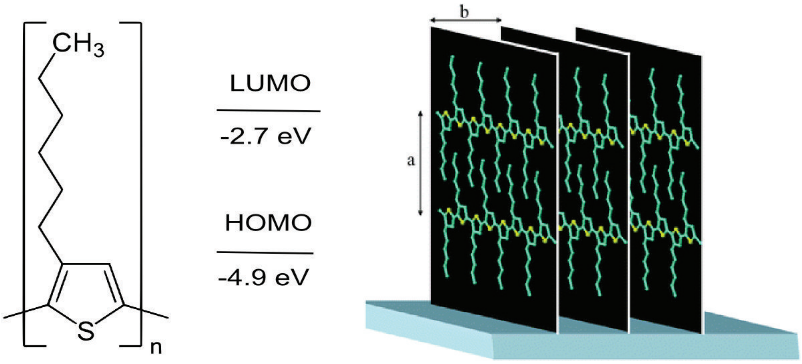

Figure 1.24: Chemical structure of P3HT. In the middle the energy levels of the HOMO and LUMO are shown, [37]. Right is the lamellar structure of P3HT depicted $a = 16$ Å and $b = 3.8$ Å, [28], [29].

### Charge Mobility of P3HT

It is known that long polymer chains are more prone to entanglement, [52]. Therefor the mobility decreases with an increase of chain length, [30]. The influence on hole-mobility for different molecular weight can be seen in Fig. 1.25. The P3HT-26(number indicates the molecular weight($M_w$)) has $\mu_h = 2 \cdot 10^{-4}\ cm^2V^{-1}s^{-1}$ that for P3HT-156, P3HT-221 and P3HT-447 is with $2 \cdot 10^{-5}\ cm^2V^{-1}s^{-1}$ one magnitude lower, [30].

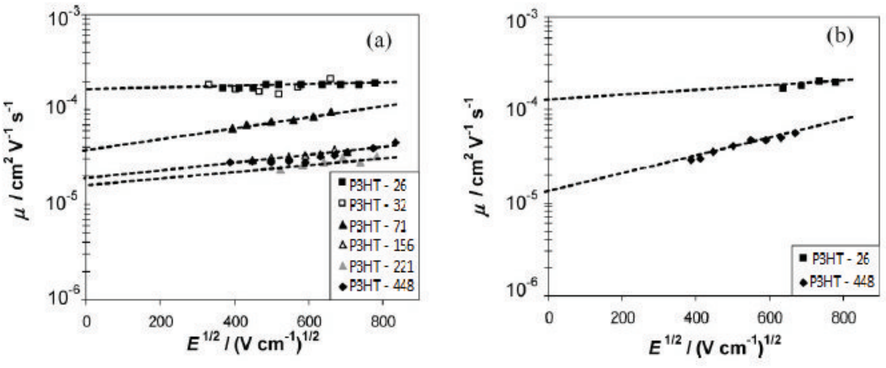

Figure 1.25: Hole mobility of P3HT for different $M_w$ in dependence of the electrical field. Right hand side the heaviest with P3HT-448 and the lightest with P3HT-26 are shown, [30]

Annealing experiments of pristine P3HT showed just a weak impact on the charge mobility. Pristine P3HT with $M_w = 52\ kg/mol$ at room temperature and at 453 $K$ was investigated. The increase was modest the unannealed film was $\mu_h = 1.7 \cdot 10^{-4} cm^2 V^{-1} s^{-1}$ and for the annealed one at $453K$, $\mu_h = 3 \cdot 10^{-4} cm^2 V^{-1} s^{-1}$, [31]. For all measurements the time of flight method was used.

### Photoluminescence Quantum Efficiency of P3HT

The results are out of [32], the pristine P3HT was measured at different temperatures, the molecular weight was not mentioned in this paper. The PLQE is given in Fig.1.26. Both measurements were done the same way: heating up from $-10°C$ to $140°C$ in intervals of $10°C$. The PLQE show a blue shift broadening. The absorption spectra shows a more defined shoulder and a red shift for lower temperatures. A decrease of PLQE was observed until $80°C$ for higher temperatures the PLQE increased, [32]. '*The reason for the increase at higher temperatures is as seen in the absorption data(Fig.1.26), P3HT becomes more ordered when heated, and this reduces defects and non-radiative recombination*', [32].

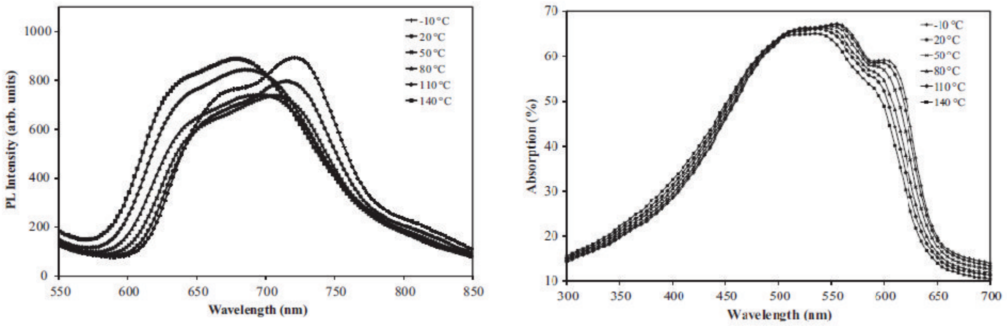

Figure 1.26: Left is the PLQE-spectra of P3HT and right the absorption spectra, [32].

### Glass Transition Temperature of P3HT

It is not easy to say something correct about the $T_g$ of P3HT, because the data in the literature is quite contradictory. The wide range of $T_g$ and the melting temperature $T_m$ are listed in Tab.1.4.

Table 1.4: All given values for the transition temperatures of P3HT are measured with Differential Scanning Calorimetry(DSC). $T_g/[°C]$ glass transition, $T_m/[°C]$ crystallisation temperature and $M_w/[kg/mol]$ molecular weight

| Papers | $T_g/[°C]$ | $T_m/[°C]$ | $M_w/[kg/mol]$ |
|---|---|---|---|
| [33] | 9.8 | 233.7 | 65.5 |
| [34] | 12 | 178 | - |
| [21] | 142 | - | 55 |

It should be mentioned that the transition temperature could be shifted with a higher or lower heating rate, but the effects are not so strong to explain the high divergence in Tab. 1.4. The last row of Tab.1.4, with the data from [21], is maybe the most reliable one, because the data of the $T_g$ from the DSC is in accordance with the data out of a Dynamic Mechanical Analysis(DMA). DMA was performed on the same batch of P3HT as the DSC.

### 1.4.3 F8BT - Poly[(9,9-di-n-octylfluorenyl-2,7-diyl)-alt-(benzo[2,1,3]thiadiazol-4,8-diyl)]

F8BT($C_{34}H_{42}N_2S_1$) is a not so common polymer in organic solar cells, but it is used as an electron acceptor. F8BT is a fluorene copolymer with a biphenyl and a benzothiaiazole units in its copolymeric segment, and has been used in highly efficient light-emmitting diods, [35]. Its chemical stucture and the HOMO and LUMO is shown in Fig.1.27. The structure of the crystallographic packing is also given in Fig.1.27. For $Cu_\alpha$ radiation the corresponding lattice constants are , [36]:

- $a = 5.3\ \mathring{A}$ with a peak at $2\theta = 16.7°$
- $b = 16.7\ \mathring{A}$ with a peak at $2\theta = 5.28°$
- $c = 14.65\ \mathring{A}$ with a peak at $2\theta = 6.02°$
- $d = 4.18\ \mathring{A}$ with a peak at $2\theta = 10.61°$

F8BT is a very promising material, it has high charge carrier mobility and a very high PLQE, but it is sensible for $O_2$ - Traps and therefore unstable.

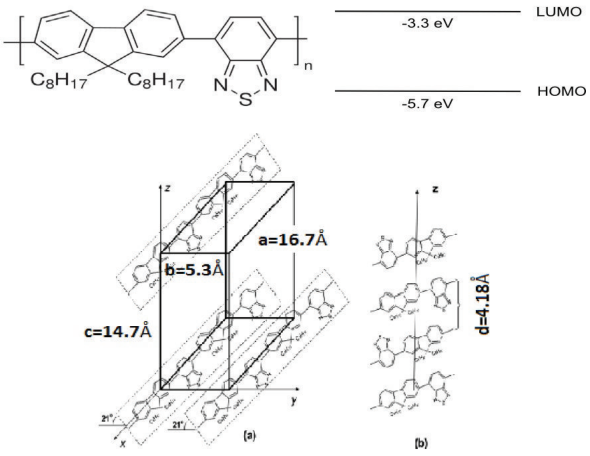

Figure 1.27: Chemical structure unit of F8BT. On the right side the energy levels of the HOMO and LUMO are shown, data is out of, [37]. Below the crystallographic packing is shwon, [61]

### Charge Mobility of F8BT

F8BT is an electron acceptor. Therefore the electron mobility is of high interest. The $\mu_e$ of F8BT are depicted in Fig. 1.28. Here the mobility increases with a increase of molecular weight and decreases with annealing. The values range from $\mu_e = 6 \cdot 10^{-4} cm^2 V^{-1} s^{-1}$ to $\mu_e = 4.8 \cdot 10^{-3} cm^2 V^{-1} s^{-1}$, see Fig.1.28.
The higher molecular weight induces a not so favorable ordering of F8BT chain to one another. Normally the F8BT with the low molecular weight organizes like in Fig. 1.28 (B), because neighbouring BT units repel each other. Through that the interspace distance between those BT units is higher, than for F8BT with high molecular weight. In heavy F8BT the long chains suppress such an arrangment and therefore the spacing in between the BT-BT unit is shorter, see Fig. 1.28 (A), [36].
Because F8 works like as barrier within the chain, the chance of hopping between BT-BT units is higher for F8BT with high molecular weight, see Fig.1.28 left and consequently the mobiltiy is increased. A decrease in electron mobility could also be observed for annealing the F8BT at the $T_g$ or higher. Here the higher temperature enables the F8BT

to rearrange through more flexibility and change the ordering of the chains from (A) -> (B), see Fig. 1.28.

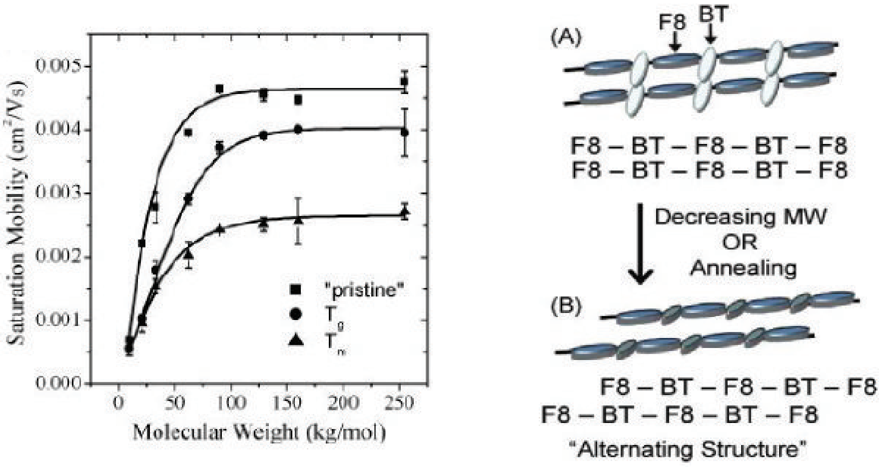

Figure 1.28: Mobility of electrons in F8BT in dependence on the annealing at the glass transitsion temperature($T_g$), melting temperature($T_m$) and molcecular weight($M_w$), left. Arrangement of F8BT, (A) for high $M_w$ and (B) for low $M_w$ or annealing, [36]

### Photoluminescence Quantum Efficiency of F8BT

F8BT has a very high PLQE compared to other polymers like P3HT. For annealing at $T_g$ a blue shift could be measured, [36]. In Fig. 1.29 the results are given for F8BT with different $M_w$ and annealing temperatures. For F8BT with low or high molecular weight the pristine samples have the lowest PLQE. With annealing at $T_g$ the PLQE become better. At higher molecular weight the cooling rate has a stronger influence on the PLQE. Annealing at $T_m$ have also positive effects on PLQE, but the improvements are a bit lower than for annealing at $T_g$. The results are in good accordance with other measurements.
Tab. 1.5 has a compartment of pristine P3HT and pristine F8BT, though the high absorption of light from P3HT the F8BT has a 12 times better PLQE then P3HT.

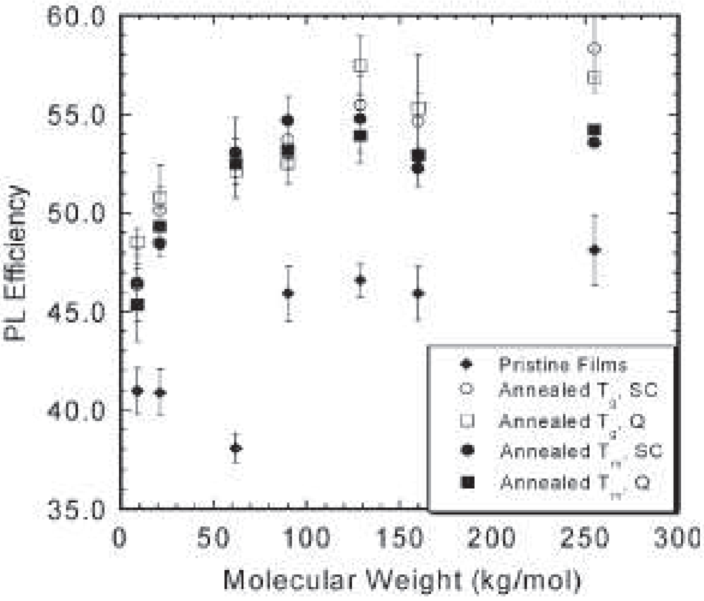

Figure 1.29: PLQE in dependence on the molecular weigth($M_w$) and annealing at glass transition temperature($T_g$) or melting temperature($T_m$), [36].

Table 1.5: PLQE in dependence of the weight ration of F8BT:P3HT in blends. The effect of P3HT is tremendous, just 20% let the PLEQ drop to one third of the pristine F8BT, [37].

| F8BT:P3HT(weight ratio) | PLQE(%) | PL lifetime($ps$) |
|---|---|---|
| 100 : 0 | 50.8 | 836 |
| 80 : 20 | 17.7 | 349 |
| 40 : 60 | 0.52 | 222 |
| 0 : 100 | 4.0 | 297 |

### Glass Transition Temperature of F8BT

The data which is presented in Tab. 1.6 was gained via DSC measurements.

Table 1.6: Glass transition temperature for F8BT with different $M_w$. $T_g/[°C]$ glass transition temperature, $T_m/[°C]$ crystallisation temperature and $M_w/[kg/mol]$ molecular weight.

| Paper | $T_g/[°C]$ | $T_m/[°C]$ | $M_w/[kg/mol]$ |
|---|---|---|---|
| [35] | 112 | 220 | 618 |
| [38] | 125 | 258 | 101 |
| [38] | 133 | 277 | 220 |
| [38] | 135 | 283 | 417 |

Our investigation of F8BT-thin films on $SiO_2$ and results from a other study on F8TBT, which is very similar give hints that the $T_g$ should be around $T_g = 133°C$, [21], [31], which was used in this work.

## 1.5 Organic Solar Cells(OSC)

One of the main differences to inorganic solar cells is the low mobility in organic devices. A conventional Si-based solar cell has a mobility for holes of $\mu_h = 450\ cm^2V^{-1}s^{-1}$ and for electrons $\mu_e = 1400\ cm^2V^{-1}s^{-1}$, [39]. Compared to organic devices they are very high. In organic semiconductors mobilities were reached in the range of $\mu_h = 15\ cm^2V^{-1}s^{-1}$ for holes in a small single crystal, but still it is more than a magnitude lower, [39]. The mobilities of P3HT said to be in the range of $\mu_h \approx 10^{-4}\ cm^2V^{-1}s^{-1}$ and for electrons in F8BT $\mu_e \approx 10^{-3}\ cm^2V^{-1}s^{-1}$, so they are in fact several magnitudes lower, than the inorganic ones.

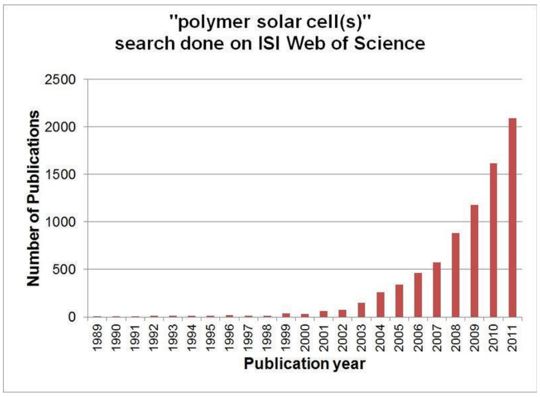

Figure 1.30: Publication world wide of OSC, [40]

However, there are also some advantages of OSC. Their light harvesting is far better than the inorganic solar cells. Usually the absorption spectra of OSC is smaller than the inorganics, but the absorption is much better. Therefore the active layer of the material can be reduced to 100 $nm$, [41] and most of the incoming photon will be absorbed. Nevertheless a organic solar cell with a lower band gab would be better for maximizing the power output. A band gab of 1.1 $eV$(1100 $nm$) can absorb 77% of the solar radiation coming to the earth(5% UV, 43% visible, 52% IR). Now organic solar cells have a band gab of about 2 $eV$(650 $nm$), which limits the possible use of incident sun light to 30%, [41]. Also rough estimations say that just 10% of the created excitons where transformed to free charge carries. So there is still a lot of

potential in the field of organic solar cells.
Despite this good prospects the commercial interest is still almost zero, but in the academic world it is a steadily growing field, Fig. 1.30.

### 1.5.1 Architecture of Organic Solar Cells

In Fig. 1.31 the two most common setups are depicted. The first OSC were single layer systems with a very low efficiency of about 0.0005% that was in the 1970s, [42], but they were rapidly replaced by other systems.

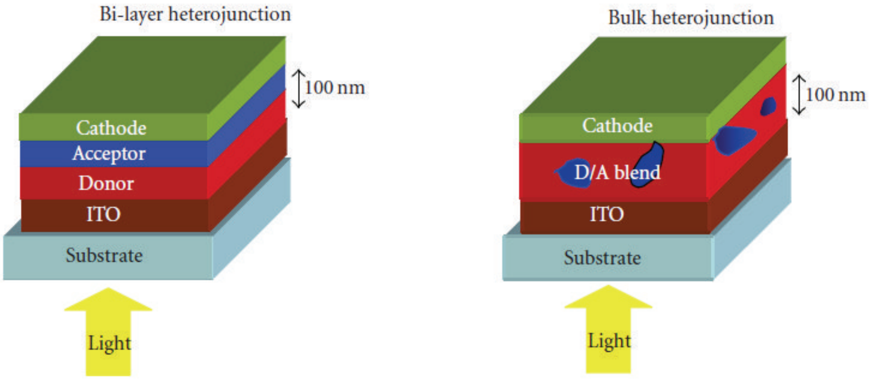

Figure 1.31: Left side a schematic bilayer cell. Right side a bulk heterojunction cell, [39].

A bilayer heterojunction OSC, Fig. 1.31 left hand side, has the advantages of a 'defined' interfaces area and that charges have a direct path to their electrode. When there are no orthogonal solvents for the two polymers the fabrication of the bilayer system can become difficult. A work around have to be found, like floating the second layer on top of the polymer on the substrate.
Blends, Fig. 1.31 right hand side, are normally much easier to build. Here both polymers or polymer/fullerene mixture are solved together in a common solvent and are spin-coated on the ITO(Indium Tin Oxide) or ITO/PEDOT:PSS(poly(3,4-ethylenedioxythiophene) poly(styrenesulfonate)). Phase separation happens, because most of the polymers don't mix with each other. Therefore a lot of interface area is created. It can be in blends that there is a path of one polymer from one electrode to the other, when this happens the cell is short circuit and won't produce anything. Also the physical properties are different in blends from their single ones. For example, blends made with P3HT:PCBM can increase their efficiency through annealing by more than a magnitude, just because the P3HT is in the pristine P3HT:PCBM layer extremely disorder and tends to order after some annealing process($T_{ann} < T_g$), see Fig. 1.32, so the mobility is increased. That was never observed for single layers of P3HT, [43]. Same was observed in blends of P3HT:F8BT, [37].
Another example is the PLQE for blends of F8BT:P3HT in the study of [44], see Tab. 1.5. Here the physical properties of the polymers change dramatically by changing the

compostition of the blend.

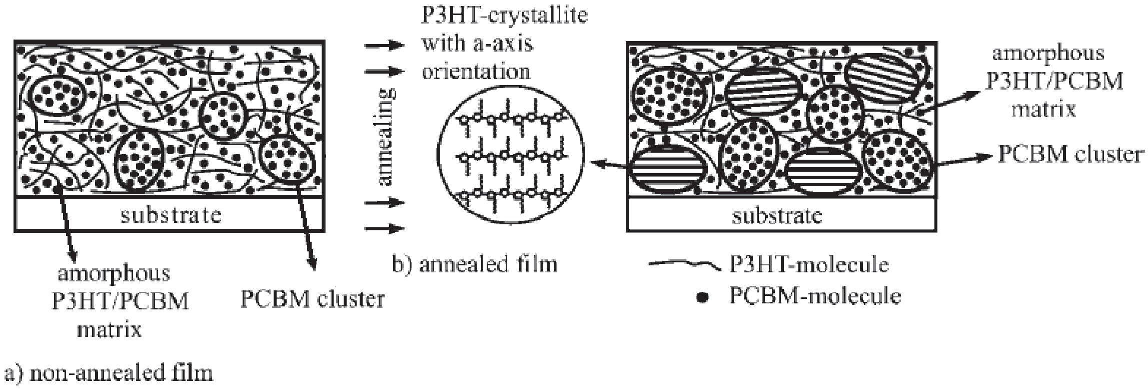

Figure 1.32: The pristine blend(a) was annealed at $75°C$ for several minutes, [53] and a big change of the structural order of P3HT could be obsered with XRD, [43]

Relatively new are tandem solar cells, see Fig. 1.33. To broadening the absorption spectra two different active layers are combined and separated with a conductive intermediate layer. Active layers could be $P3HT : PCBM$ and $ZnPc : C_{60}$, [45]. Improved efficiency could be demonstrated, which is a result of an higher $V_{OC}$ and $I_{SC}$. New difficulties also arise with this type of setup. Charges of the subcells can recombine at the intermediate layer, so current matching must be considered. Otherwise one charge will accumulate at the interlayer and decrease efficiency, [45]. On the other hand the intermediate layer consist of a thin metal layer, which reduces the transmitted light for the second subcell. For example a layer of In 100 $nm$ thick just transmit only $1 - 2\%$ of the incident light in the visible region, [42].
In January 2013 a German company set a new world record with tandem OSC. They reached an efficiency of $\eta = 12\%$. For the fabrication oligomers were used. With vacuum deposition it was possible to make stacks of ultra thin layers, which were highly order. According to Heliatek, they built also tandem cells with three active layer and obtained a OSC with a very wide absorption spectra in the visible region, [47].

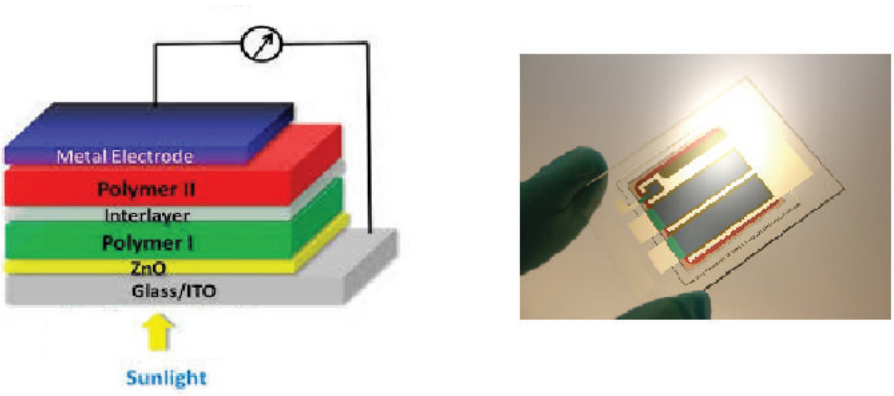

Figure 1.33: Left a schematic picture of a tandem solar cell. Mined the intermediate layer and the two subcells. Right a picture of the world record OSC from Heliatek, [46].

### 1.5.2 How does an organic soalr cell work?

If a photon is absorbed by a conjugated polymer it can lift one electron from the HOMO(Highest Occupied Molecular Orbital) into the LUMO(Lowest Unoccupied Molecular Orbital). That creates an electron in the LUMO and a hole in the HOMO. This electro-hole pair is called exciton. The exciton is electronically neutral and moves mostly along the polymer backbone. Their short lifetime limits the local movement to just $\approx 10\ nm$ nanometers. Because of their electron neutrality they diffuse around in the active layer. This process is statistical, schematic depicted in Fig. 1.34.

To get an electrical current out of the OSC the exciton have to separate and this can just happen at polymer phase interfaces. Here the right arrangement of HOMO and LUMO of both polymers come into. Electrons can just be transferred to lower laying levels and holes can just move into higher laying bands.

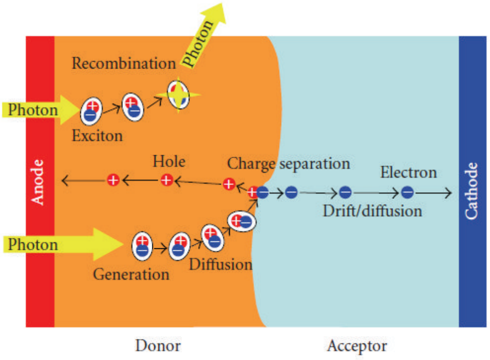

Figure 1.34: The diffusion of an exciton in a bulk heterojunction with charge separation at the polymer interface, [39].

To optimize this transfer process the energy gab between $HOMO_{don}$ and $HOMO_{acc}$ and $LUMO_{don}$ and $LUMO_{acc}$ respectively should by small, to minimize barriers for a good transfer statistic, [39], [41], [45].
For a good charge separation at the interface the difference between the ionsation potential of the donor and the electron affinity of the acceptor must be larger than the binding energy of the exciton, [39]. If this is the case the electron can fall in the $LUMO_{acc}$ and the hole in the acceptor can be transferred into $HOMO_{don}$. That is also why the p-type material is by OSC called donor, because it give the electron to the n-type material, despite it is a hole conductor.
Fig. 1.35 gives a schematic view over the charge separation left hand side and an exciton transfer right hand side. If the HOMOs and LUMOs are arranged like in the left side charge separation is possible.

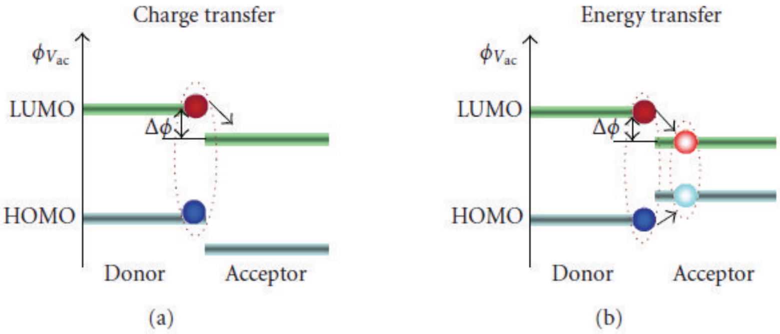

Figure 1.35: Schematic view over two possilbe process of an exciton at a polymer interface. $\Delta\phi$ is the difference between the LUMO of the acceptor and donor, [39]

Another important thing is the choice of electrodes, which collect the charges after separation. As anode materials usually metals with a high work function are used to

prevent blocking an the anode/acceptor interface. The work function should match the $HOMO_{acc}$. For the cathode side low work function materials are used, which match the $LUMO_{don}$.
Before the free charges can be collected they must come to their corresponding electrode. This is done by the built in potential, which is produced from the wok function difference of the electrodes. $V_{built-in} = W_{cathode} - W_{anode}$. Even a little difference cause by a thickness of 100 $nm$ a locally very high electric field. To increase efficiency through enhanced charge collection a high work function difference is necessary, [39], [41] and [45].

### Efficiency

It depends on a lot of different parameters. For an overlook the most important ones are summed up:

- Absorption of light
- Generation of excitons
- Life time of excitons
- Transport to the interface
- Phase interface area for charge separation
- Charge separation
- Built in potential
- Charge mobility of the polymers
- Charge collection of the electrodes
- $V_{OC}$

### Interface Engineering

Gaining more efficiency is the major task in the field OSC. Different materials were employed to reduce minor currents and blocking barriers. The almost famous PEDOT:PSS(poly(3,4-ethylenedioxythiophene) poly(styrenesulfonate)) is mostly spin-coated onto the ITO to avoid such blocking barriers and to planarize it. But its inhomogeneity limits the ability of electron blocking, [48]. Other materials are better in this concerns like, transition oxides such as vanadium oxide($V_2O_5$), molybdenum oxide($MoO_3$), nickel oxide($NiO$) and tungsten oxide($WO_3$), they improve the interfacial properties and are hole-transporting electron blocking, [48]. The cathode side need materials as it was mentioned above with a low work function. Suggestion are lithium florid LiF/Al or calcium Ca/Al. These materials are electron selective and can prevent the cathode from oxidation, [48].

### 1.5.3 Characterization of OSC

For the characterization of an OSC the four major quantities are listed:

- **Open Circuit Voltage**($V_{OC}$) depends on the off set between the energy bands of acceptor and donor.

  $$V_{OC} = LUMO_{acc} - HOMO_{don} - 0.4V$$

  Usually there is a loss at each electrode of about $0.2eV$.

- **Short Circuit Current**($I_{SC}$) is the maximum current the OSC can provide.

- **Fill Factor(FF)** is calculated like:

  $$FF = \frac{V_{MPP}I_{MPP}}{V_{OC}I_{SC}}$$

  Where $V_{MPP}$ and $I_{MPP}$ are determined through the point of maximum power(maximum power point), is depicted in Fig. 1.36. The fill factor gives a hint how good a solar cell works, low FF can mean a weak charge collection or separation.

- **Power Conversion Efficiency(PCE)** is just the efficiency of the OSC. The performance at the Maxiumum Point of Power(MPP) is divided by the incoming light from the solar simulator.

  $$\eta = \frac{V_{MPP}I_{MPP}}{P_{in}}$$

  $P_{in}$ is the power of the incident light.

### 1.5.4 Photovoltaic Measurement

For the characterisation of an organic solar cell the $I(V)$ have to be taken under light. The Source Measuring Unit(SMU) is needed to obtain this $I(V)$ curves, in Fig. 1.36.

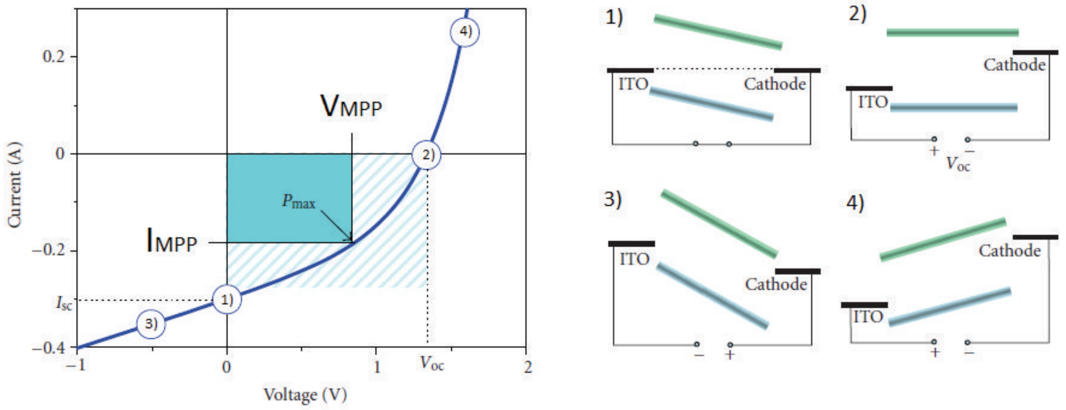

Figure 1.36: A typical V-I measurement is shown on the left side. Right side shows four different stage of the energy levels from the electrodes and active layer, [39]

The $I(V)$ curve can be divided into three section where charge collection happens $V < 0$, photo active section $0 \leq V \leq V_{OC}$ and the diode mode $V_{OC} < V$. The four points are following:

1. Here the SMU is in zero-bias. At this point the charge collection from the solar cell is in its maximum and called $I_{SC}$ for short circuit current. The current consists of a drift current and a diffusion current. The drift current is caused by the internal field of the OSC and the charge will move along the gradient. The diffusion current comes from high charge concentrations at the phase interface and the charge will move long the concentration gradient, [45].
   Because the electrodes are in a equilibrium state the bands in the active layer have to incline. The inclination of the band HOMO and LUMO, causes that the electron and holes can still move to their corresponding electrode. In other words, at $I_{SC}$ the internal electric field is maximum and charge separation and collection are therefore at their possible maximum too. The shift of the band depends on the built in potential, which is nothing more than the work function difference of the anode and cathode.
   In the region $0 < V < V_{OC}$ the SMU applies a voltage, which reduces the internal electrical field inside the active layer of the organic solar cell. Therefore the collected photocurrent is reduced.

2. At this point the SMU provides the same voltage as the solar cell. No current follows, the bands of the polymers are flat and there is no internal field at all in the active layer. The point is called $V_{OC}$ for open circuit voltage and it is the maximum voltage, which the solar cell can give.

3. Last mode is when $V < 0$, here the SMU increases the electric field in the active layer of the solar cell. The higher field leads to a better charge collection and separation. Normally there are a lot of traps and disorders in the polymers, which reduces the mobility of the charges. With an higher field charges are prevented from sticking in a trap and therefore the current is here higher than in zero bias($I_{SC}$).

4. If the voltage is increased over $V_{OC}$ charge injection takes place. Electrons are injected from the side of the cathode into the LUMO of the acceptor and holes from the anode, respectively. Here photons are produced at the interface through hole-electron annihilation.

### 1.5.5 Stability

This topic became in the last years more and more attention from the scientific community. The reason is plain, inorganic solar cells are until now the devices of choice for commercially production and distribution, though to they are quiet expansive, their good performance of about for example $\eta = 15\%$, [49], for a Silicon based photovoltaic device and a rather long operational lifetime. So the perfect organic solar cell should be stable in atmosphere, easy to processes and efficient, see Fig. 1.37, otherwise the industry will not have any interest in these products.

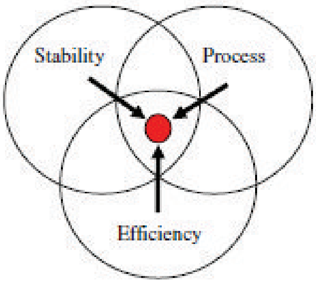

Figure 1.37: Problems like stability, efficiency and cheap production have to be solved, [50]

But still it is a young field, where may only creativity limits the possibilities. Polymers with a good prospect are P3CT(poly(3-carboxythiophene-co-thiophene)), it is very stable under light and normal conditions with it lifetime of about 10 000 $h$ are in reach, [50].

Therefore stability gets more in the focus of researchers. Now some long term studies are available, but still the community lacks of standardised methods that a comparison between each study becomes easy or even possible. The problem is, that devices physics is a field, where a lot of parameters(temperature, light, polymers, interfaces,...) play a roll and a good standardisation is hard to define. The question is also, which parameter should quantify the degradation, of cause $I_{SC}$ and $PCE$ are good candidates.

The life time table in Fig. 1.38 PPV(Poly(p-phenylen-vinylen)) is only stable for a few hours, because of photo oxidation. P3HT has a longer lifetime of a few day, nevertheless it is degradating very fast. Good prospects gives materials like P3CT, which is suspected to have a lifetime of about 10 000 hours.

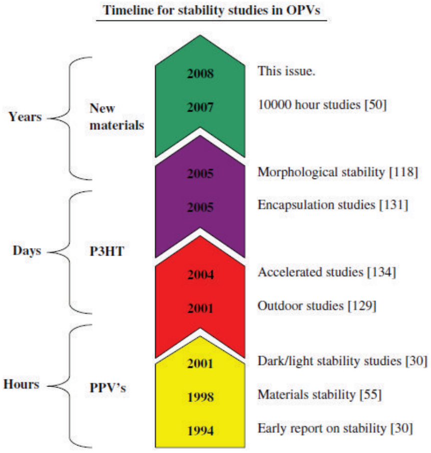

Figure 1.38: Lifetime table of the most famous polymers, [50]

### 1.5.6 Degradation

**Chemical degradation** is mainly focusing on effects of oxygen, water and electrode material reactions with the active polymer, [50]. The oxygen can come through the manufacture process into the polymer, but also the exposure of the device to atmosphere leads to an diffusion of oxygen and water into the active layer and consequently to a decay of efficiency.
As it was studied in the work, [51] oxygen led in F8BT to a decrease of mobility, because of the high affinity of $O_2$ for electrons, they were able to increase the mobility of F8BT with DMC(demethylcobaltocene) a n-typ donor.
Photochemistry and photo-oxidation of polymers is another topic of degradation and the polymers of the future have to be stable under UV-light. A famous example for photo-oxidation is PPV(Poly(p-phenylen-vinylen), it is very unstable, see Fig. 1.39. Here the single oxygen is believed to react with the vinylene groups in PPVs and breaks the chain, [50].

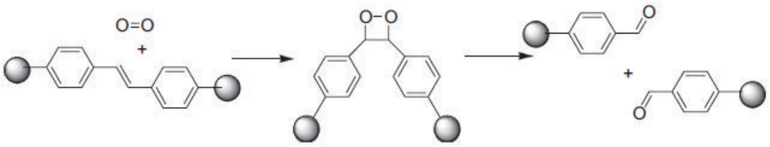

Figure 1.39: The oxygen is coupling with vinylene bond and forming an intermediate dioxetane by cutting the chain. The aldehyde products can react further with oxygen, [50].

Also the PEDOT:PSS layer, which is usually on top of the ITO(indium tin oxid) can lead to the diffusion of water. It is used to prevent blocking barriers on the anode. So the PEDOT:PSS is spin-coated directly on top of the ITO. The hygroscopic nature of PEDOT:PSS was reported to attract water from the atmosphere, [50].
Water accelerates the etching of ITO-electrode. Then the indium($In$) diffuses through the active layer to the counter electrode, how $In$ reacts in the active layer is still unknown. Water and oxygen can diffuse in the interface of polymer and electrode and reduce the contact dramatically. It is known that oxygen reacts with the aluminium cathode and forms aluminium oxides at the interface, which acts like a blocking layer, [50]. All described processes are shown in Fig. 1.40.

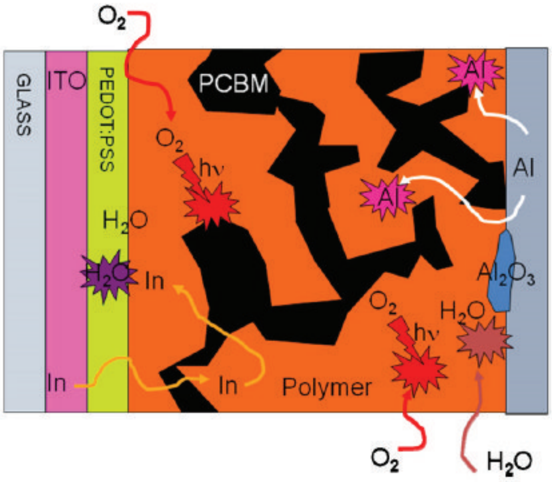

Figure 1.40: Scheme of the most important degradation processes, [50].

**Physical degradation** is concerned with the structural and morphological changes of the active layer. It could be that the highest efficiencies are obtained from a not thermodynamically stable state, still physical degradation is a small field.

# 2 Experimental

This chapter gives an overview of the methods and equipment, which were used to prepare the samples. All the samples were prepared in the lab of the TU-Graz, Institute of Solid State Physics.

The used polymers were P3HT with a $M_w = 70\ kg/mol$ as donor and F8BT with a $M_w = 150\ kg/mol$ as an acceptor the mean properties of those materials listed in Sec.ă1.4.

To make thin films with organic polymers a very good straight forward method is to spin-coat the polymers onto a substrate. For a reasonable XRR-investigation defined substrates, like $SiO_2$ or native $Si$ are the first choice. They have a more less defined surface roughness, which is in between $0.30\ nm < \sigma_{rough} < 0.50\ nm$.

Both types of silicon substrates are from a $Si$-wafer with 150 $mm$ in diameter with a orientation of $\{100\}$ at the surface and cut into pieces with the size of $20 \times 20\ mm$. The $SiO_2$ has a thermally grown $SiO_2$ layer with a thickness of 150 $nm$. The native $Si$ is cut the same way, but there is no thermally grown $SiO_2$ layer. The $SiO_2$ layer in native $Si$ is about 1.6 $nm$ thick and comes of the diffusion of $O_2$ into the $Si$ surface layer. Because the OSC have ITO as substrate the first idea was to investigate the thin films on those, but it turned out that ITO is far to rough to get any information out of the polymer, which is spin-coated as a thin film on top. Also there was never an interest in the interface between the polymere/substrate, therefore all the samples for the reflectivity measurements were prepared on $SiO_2$ or native $Si$ and not unpatterend ITO. The focus still lays on the interfacial morphology of P3HT/F8BT, so there was no loss of information by building the samples for the reflectivity measurements on silicon substrates. Influences of the different surface energy of the substrates on the polymer interface were generally neglected, because the thin films were much thicker than some monolayers.

## 2.1 Sample Preparation for Reflectivity

To obtain good thin films with spin-coating the right solvent, rotation speed and temperature of the solution must be found. Because of the quiet long polymer chains it turned out that low boiling point solutions like chloroform($T_{boil} = 61.3\ °C$) are not suit able for spin-coating P3HT or F8BT. Chloroform evaporates far to fast and so lot of polymer clusters are formed, which can be seen with eye. Therefore the films were to rough and no fringes were seen in XRR experiments.

A work around would be to reduce the concentration of the polymers in chloroform, but than films with a thickness of just 20 $nm$ are gained. Next possibility were different solvents like chlorbenzene($T_{boil} = 132\ °C$), xylene($T_{boil} = 140°C$) or toluene($T_{boil} = 111°C$).

All those have a far higher boiling point than chloroform. Chlorbenzene showed the best and fastest dissolving characteristics for P3HT and F8BT and had also a high boiling point, so for all samples which were measured with XRR chlorbenzene was used.

### 2.1.1 Spin-Coating

The thickness and surface roughness of the thin film are determined through concentration of the solution, type of solvent, temperature of the solution and rotation speed. It needs a bite of experience to produce reproductive results. Also the right amount of solution is important to get optical nice homogeneous films over the whole substrate. The polymer films on native $Si$ and $SiO_2$ were later on always produced the same way, the parameter, are listed in Tab. 2.1 for P3HT and for F8BT in Tab. 2.2.

Table 2.1: The P3HT was disolved in chlorbenzene. Rotation time is the duration of the spin-coating process. The solution was on the heater for a period of 20 $min$ at a temperature of 100°$C$ and was immediatly spin-coated.

| substrate | Concentration/$[g/l]$ | rotation / $[rpm]$ | rotation time /$[s]$ |
|---|---|---|---|
| n-$Si$ | 8.5 | 1000 | 60 |
| $SiO_2$ | 9.1 | 1000 | 60 |

| solution temp. /$[°C]$ | time /$[min]$ | amount / $[\mu l]$ | thickness/$[nm]$ |
|---|---|---|---|
| 100 | 20 | 160 | 39 |
| 100 | 20 | 160 | 51 |

Table 2.2: The F8BT was disolved in chlorbenzene. Rotation time is the duration of the spin-coating process. The solution was on the heater for a period of 20 $min$ at a temperature of 100°$C$ and was immediatly spin-coated.

| substrate | Concentration/$[g/l]$ | rotation / $[rpm]$ | rotaton time /$[s]$ |
|---|---|---|---|
| n-$Si$ | 7.8 | 1000 | 60 |
| $SiO_2$ | 8.3 | 1000 | 60 |
| $SiO_2$ | 12 | 1000 | 60 |

| solution temp. /$[°C]$ | time /$[min]$ | amount / $[\mu l]$ | thickness/$[nm]$ |
|---|---|---|---|
| 100 | 90 | 160 | 59 |
| 100 | 90 | 160 | 70 |
| 100 | 90 | 160 | 120 |

To get a well defined substrate surface a cleaning process is necessary. The whole procedure was the following:

- Substrates were cleaned from particles like dust with $CO_2$
- Then put into first acetone and second isopropanol for each 10 $min$ in ultra sonic bath
- After the ultra sonic bath $SiO_2$ was plasma etched for 10 $min$, but the native $Si$ never
- The solution was heated up at a normal heating plate at 100°$C$ and kept there for 20 $min$ for P3HT. F8BT was kept also at 100°$C$ but for 90 $min$, because it is dissolving much slower than P3HT.
- Substrates have to be tried from isopropanol totally, otherwise the film becomes in homogeneous this was done in vacuum chamber for about 2 $min$ at a pressure of $10^{-2}$ $mbar$.
- Then the solution was pored on the substrate and the spin-coater started, Fig. 2.1.

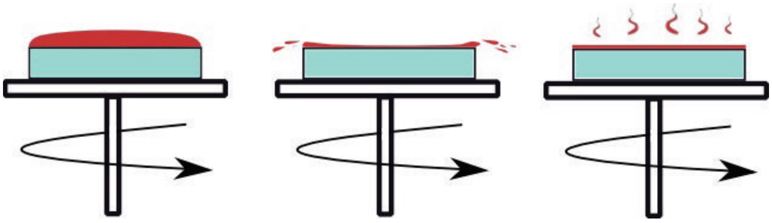

Figure 2.1: Spin-coating

### 2.1.2 Floating

For floating, the polymer is spin-coated on top of a glass substrate, parameters are listed in Tab. 2.2. The glass was cleaned like the silicon substrates. The floating was used to deposit the F8BT on top of the P3HT to build the bilayer samples. Floating was more less a necessary work around, because there was no knowledge of an orthogonal solvent for spin-coating the second layer on top of P3HT.
A pity was that the glass was to rough to find out the thickness of the F8BT on glass, but the assumption was that the thickness should not differ to much from the thickness of the native $Si$.
The F8BT film was scratched with a razor along the edges of the glass substrate. Through that scratches the distilled water can creep into the polymere/substrate interface and lift the film from the glass, Fig. 2.2. The film drifts then on the water surface and can be directed easily over the substrate or the P3HT for depositing. The films have to be kept over the P3HT while the water level decreases.

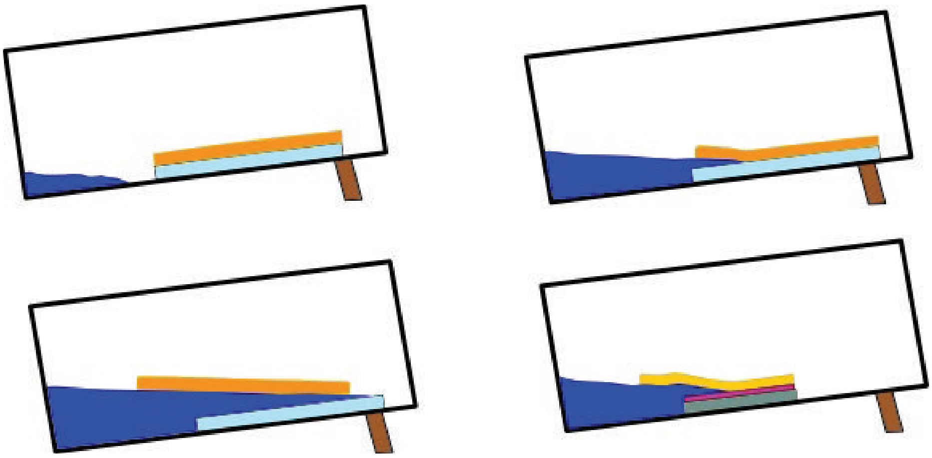

Figure 2.2: Floating

### Water Residuals in the Polymer Interface

Sometimes water droplets are enclosed in the interface, but the usually disappear very fast through the F8BT layer, see appendix 4.2. The water residual streches the F8BT and induces a local morphological change.
A very thin water film between those layers seems to be obvious, nevertheless it was never detected in the XRR or NR, but one have to mention that the scattering length density of water is similar to that of P3HT for X-rays. The only candidate left is the photovoltaic measurements, but also here an interpretation is hard and unconvincing. One option would be to find an orthogonal solvent and compare the efficiencies and I-V-characteristics of the floated and spin-coated bilayer OSC.

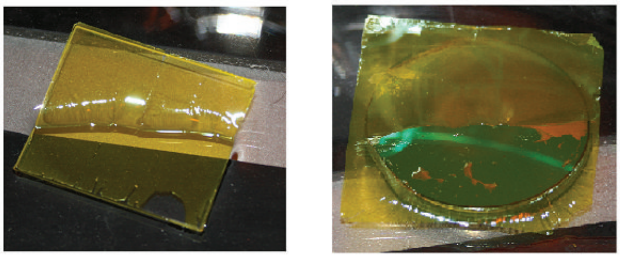

Figure 2.3: The water lifts the F8BT from the glass, left. Right F8BT is deposited on the P3HT, water residuals can be seen.

Personally I think there is some water in the interface and reduce the phase interface area, but its effects are not so strong, that the data which was obtain through XRR, NR or OPV-measurements is highly effected. Because as long as the OSC produce an electrical current, there have to be the polymers in contact, otherwise the efficiency would be not so high.

## 2.2 Preparations of Organic Solar Cells

OSC were built a bit differently than the normal ones. To get rid of another parameter PEDOT:PSS was disclaimed. To prevent a hole blocking barrier at the anode side, the ITO was plasma etched. It was shown that plasma etching with $O_2$ lowers the work function for ITO. If ITO is just cleaned in acetone and isoporpanol the work function is about $4.5 \pm 0.1\ eV$ and after plasma etching it is lowered to $4.70 - 4.89\ eV$ depending on the method of plasma etching, [54].
The cleaning procedure for ITO was the following:

- To get the rest of the photo resit of the ITOs were rubbed very carefully with in methanol dumped cotton buds.
- Cleaning with $CO_2$
- Cleaning with methanol, acetone and isopropanol for each 10 $min$. After every cleaning step they were washed with the next coming solvent.
- Plasma etched for 10 $min$ under a flow of 8
- Now the ITO substrates were ready for spin-coating.

Spin-coating and floating was the same as for the silicon substrates. The key for good OSC is timing and to work very clean. When the ITO are plasma etched, they have to be spin-coated immediately otherwise the work function level goes back to its original value.

### Glove Box

The advantages of a glove box are a defined and low oxygen and water atmosphere in the working area. The glove box can guarantee a reproducibility concerning especially organic devices.
One problem was that after floating the samples were wet. For drying they were stored in the lubricator of the chemical glove box over night under vacuum($10^{-3}\ mbar$). To reduce degradation the lubricant was filled with $Ar$ and evacuated three times.
Next step was to evaporate the cathode on top of the F8BT. For this the samples were put into a mask, Fig. 4.3 and then into the evaporator. With a rotary vane pump in combination with turbo molecular pump. The pressure was reduced to $9 \cdot 10^{-6} mbar$, that took in average 1 $h$.
Then the cathode was evaporated slowly on the F8BT. The thickness was controlled with a oscillating crystal constantly. After reaching 100 $nm$ of cathode material the evaporation was stopped.

As cathode material *Ag* was used, the work function is around 4.14 *eV*,4.22 *eV* and 4.46 *eV* with the orientations (110), (100) and (111), respectively, [55]. So it should lie in average around $\approx 4.20\ eV$.
Aluminium was not used because some colleagues had troubles with oxidation of the evaporated *Al*. A schematic picture of the energy levels of this bilayer OSC is given in Fig. 2.4.

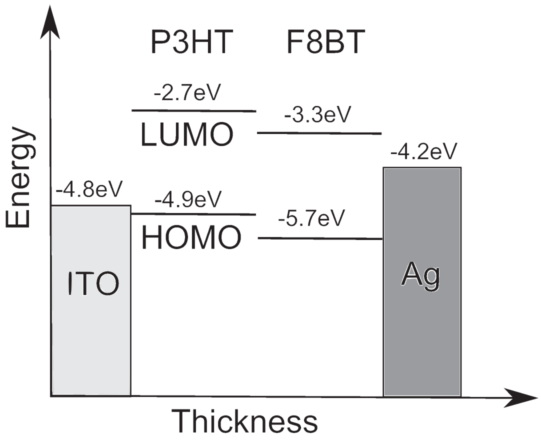

Figure 2.4: Energy levels of the built OSC

### Organic Solar Cells Preparation for Measurement

The ITO is patterned like in Fig. 2.5. The active area is about 6 $mm^2$ for every device, 6 devices are on each ITO substrate. For contacting them individually legs, like Fig. 2.5. have to be fixed on them. This was done in the chemical glove box. After that the cathode side was sealed with a glass plate, which was simply glued on it.

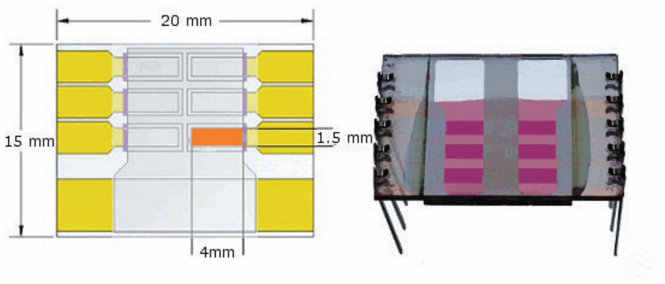

Figure 2.5: Left the patterned ITO, the active area is marked. Right finished OSC with legs that contact each device individually, [56]

### Evaporation Mask for the Cathode

Within this work the old evaporation mask was replaced by a new one with a better accuracy of the cathode deposition and more slots for ITOs. The old mask had a weakly

designed distance plate between the cathode mask and the ITO slots, so it was likely that the bilayer got some scratches, while putting them into the slots and this scratches causes normally a short circuit. Therefore it was hard to get with the old mask more than 60% of working device.
To be more reproducible a new mask was designed, which should compensate the problems of the old one. The new one has a better distance plate, which still too thick($0.3\,mm$) so evaporated cathode seems to be a bite washed out at the edges. Six slots and the accuracy is better than with the old one. The mask was fabricated at *Fein Blech Technik(FBT)* via waterjet cutting. The drawing are in the appendix, Fig. 4.3.
This mask has also two very accurate holes in every plate, in which cylindrical adjust pines can plugged to ensure the accuracy for the active area.

## 2.3 Annealing

### 2.3.1 X-ray Reflectivity

The bilayers on native $Si$ were annealed in the Anton Paar DHS 900 under inert conditions. The sample is covered with an plastic or graphite doom and this enables DHS 900 to measure the annealed samples in-situ. The DHS 900 was for one annealing series mounted in the PANalytical Empyrean. In one series the sample was never moved or touched. It was just necessary to align the sample after every annealing step for the XRR.

### 2.3.2 Organic Solar Cells

The annealing of the OSC was done in the oven of the solid state physics lab. The major problem was to guarantee a constant temperature during a annealing period. To ensure this a combination wrench size 20 was used. It is quiet heavy and serves as a heating bath. The OSC were put with the cathode side down onto the combination wrench after it was for $2\ h$ in the oven to guarantee a more less constant temperature.

### 2.3.3 Measurments of Organic Solar Cells

For this the legs of the OSC are put into the contacts of a special measuring board. Each pixel could be switch of individually and the cathode is set as ground. A calibrated light source simulates the spectra of the sun on earth AM 1.5G(air mass 1.5 global) with a $100\ mW/cm^2$.

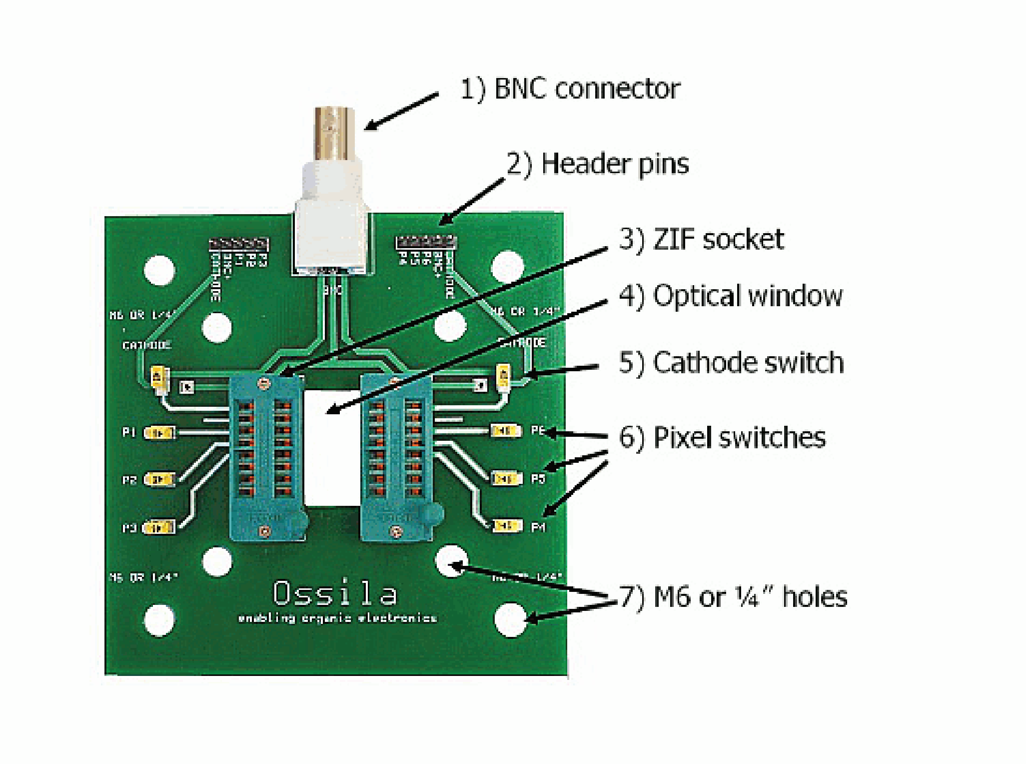

Figure 2.6: Measuring platin of Ossila. with the pins every device could be swithced individually, [56].

# 3 Data

All the sample preparations happened in the lab of the Solid State Physics Institute of TU Graz, but some measurements were done at other institutions, like the neutron experiments of cause, the atomic force microscope pictures were done by Dr. Bettina Friedel in Cambridge, England and the scanning electron microscope picture were shoot together with Sanja Simic, Dr. Bettina Friedel at the Institute for Microscopy and Nanotechnology.

## 3.1 Single Layers

First both polymers were investigated as single layers ontop of native $Si$, $SiO_2$ and unpatterend ITO to gain electron density, roughness and thickness. The XRR for the ITO are presented in the appendix, Fig. 4.6. Those substrates were too rough and so the data out of XRR was not very useful.

### 3.1.1 X-ray Reflectivity of P3HT

The fits of different P3HT films led to the conclusion, that on native $Si$ the P3HT tends to have a higher mass density and therefore a higher electron density than on $SiO_2$. Regarding the influence of the substrate, also the thickness is different for the same solution. $SiO_2$ has thinner films than native $Si$. A reasonable explanation is, that $SiO_2$ were always plasma etched for 10 $min$. It is known that plasma etching laid to a change of the surface energy of the substrate , the values are shown in Tab.3.1.

Table 3.1: Different thickness was obtained native $Si$ and $SiO_2$, when all other parameters were constant. The results below are for a concentration of 9.5 $\frac{g}{l}$.

| Substrate | Thickness $/[nm]$ |
|---|---|
| native $Si$ | 57 |
| $SiO_2$ | 51 |

Many XRR-measurements were done on thin-films of P3HT during this thesis, setup of the PANayltical is in the appendix, Sec. 4.1. Here are shown just three representative XRR-scans with fits. As it was discussed in Sec. 1.1.2, fits of XRR-data are not uniquely. The same model is used to describe the electron density of the film and roughness, so there will be always more than one fit for the same XRR-scan. Though there is no possibility to extract exact data for $\rho_e$ and $\sigma_{rms}$, one can get a rough idea out the range of the values and out of the shape of the XRR a qualitatively picture can be obtain, if

the interface is rougher or the surface.
In Fig. 3.1 is RR-P3HT on $SiO_2$ mind the very high accuracy of the thickness estimation, if the fringes are defined the mistake less than 2%. The Bragg-peak at $\alpha_i = 2.7°$ from the lamellar packing is visible. Measurement parameters were: range: $2\theta = 0 - 6°$, step size:0.005°, int.time: 2 $s$.

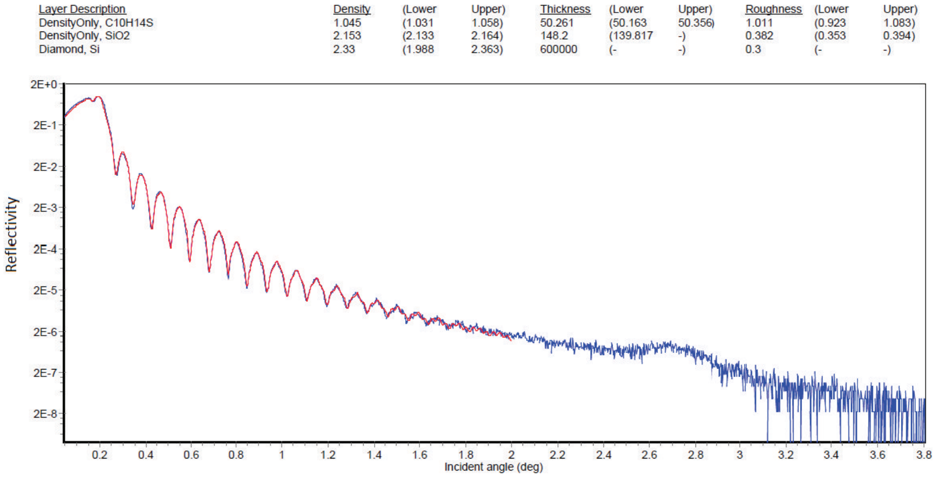

| Layer Description | Density | (Lower | Upper) | Thickness | (Lower | Upper) | Roughness | (Lower | Upper) |
|---|---|---|---|---|---|---|---|---|---|
| DensityOnly, C10H14S | 1.045 | (1.031 | 1.058) | 50.261 | (50.163 | 50.356) | 1.011 | (0.923 | 1.083) |
| DensityOnly, SiO2 | 2.153 | (2.133 | 2.164) | 148.2 | (139.817 | -) | 0.382 | (0.353 | 0.394) |
| Diamond, Si | 2.33 | (1.988 | 2.363) | 600000 | (- | -) | 0.3 | (- | -) |

Figure 3.1: The XRR-data is plotted in blue and the fit in red. The results of the fit are above.

In Fig. 3.2 RR-P3HT is on top of native $Si$. Fit on native $Si$ are easier to do, because the $SiO_2$ layer don't have to be regarded in the model and this made the fit a bit more accurate. At $\alpha_i = 2.7°$ the Bragg-Peak of P3HT and the simulation without a consideration of the lamellar structure are shown. Measurement parameters were: range: $2\theta = 0 - 6°$, step size:0.002°, int.time: 1 $s$.

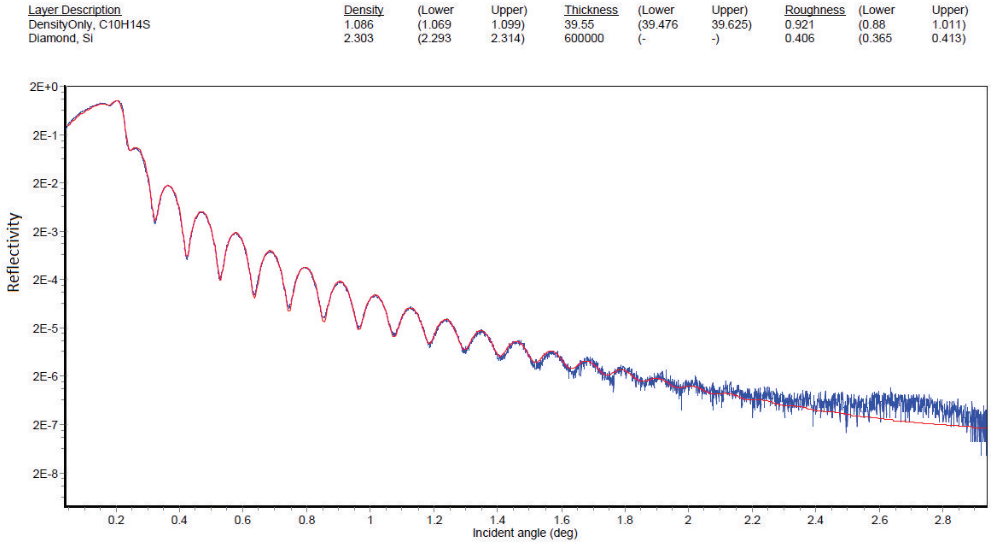

| Layer Description | Density | (Lower | Upper) | Thickness | (Lower | Upper) | Roughness | (Lower | Upper) |
|---|---|---|---|---|---|---|---|---|---|
| DensityOnly, C10H14S | 1.086 | (1.069 | 1.099) | 39.55 | (39.476 | 39.625) | 0.921 | (0.88 | 1.011) |
| Diamond, Si | 2.303 | (2.293 | 2.314) | 600000 | (- | -) | 0.406 | (0.365 | 0.413) |

Figure 3.2: The XRR-data is plotted in blue and the fit in red. The results of the fit are above.

Fig. 3.3 shows RRa-P3HT on top of $SiO_2$. The RRa-P3HT sample is amorpheus, compared to Fig. 3.2 and Fig. 3.1 there is no P3HT-peak at $\alpha_i = 2.7°$. Measurement parameters were: range: $2\theta = 0 - 8°$, step size:0.005°, int.time: 2 $s$

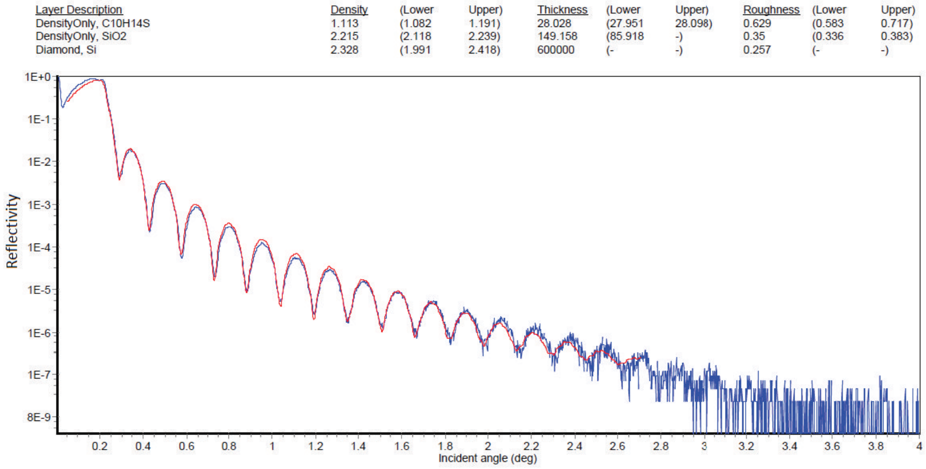

| Layer Description | Density | (Lower | Upper) | Thickness | (Lower | Upper) | Roughness | (Lower | Upper) |
|---|---|---|---|---|---|---|---|---|---|
| DensityOnly, C10H14S | 1.113 | (1.082 | 1.191) | 28.028 | (27.951 | 28.098) | 0.629 | (0.583 | 0.717) |
| DensityOnly, SiO2 | 2.215 | (2.118 | 2.239) | 149.158 | (85.918 | -) | 0.35 | (0.336 | 0.383) |
| Diamond, Si | 2.328 | (1.991 | 2.418) | 600000 | (- | -) | 0.257 | (- | -) |

Figure 3.3: The XRR-data is plotted in blue and the fit in red. The results of the fit are above.

The big difference between the regioregular(RRa)- and regiorandom(RR)-P3HT are, the lack of of the Bragg-peak at $\alpha_i = 2.7°$. The disorder of the head and tail groups in RRa-P3HT suppress the lamellar ordering, which can be observed in, Fig. 3.1 and

Fig. 3.3 and correlated to the distance of the polymer back bone. But also here the Bragg-peak is weak or better amorphous, this is because of the high $M_w = 70\ kg/mol$. The electron density of the P3HT can be calculated out of the mass density. To determine $\rho_e$ the homepage, [57] was used, the way was the following:

$$\rho_m(polymer) -> \ \delta\ and\ \beta -> \ \rho_e$$

The obtain $\rho_e$ are given in Tab. 3.2 below and were calculated out of the $\delta$ and $\beta$ with a program, provided from J. Novak, ESRF, Grenoble, France, 2008.
Tab. 3.2 list measurements of individual samples. The obtained data of the native $Si$ scans diverge, but the average value for the mass density for P3HT was $\rho_m = 1.06 \pm 0.04 g/cm^3$.

Table 3.2: The measurmetns were done on individual samples. With the XRR fit of P3HT single layer the mass density($\rho_m$) was calculated. [57] can provide $\delta$ and $\beta$ if the chemical structure and $\rho_m$ is known. The electron density and scattering length density($\rho$) was calculated.

| Polymer | $\rho_m$ / $[g/cm^3]$ | $\rho_e/[1/\AA^3]$ | $\rho/[10^{10}cm^{-2}]$ |
|---|---|---|---|
| P3HT($SiO_2$) | 1.045 | 0.343 | 9.66 |
| P3HT(n-$Si$) | 1.059 | 0.347 | 9.79 |
| P3HT(n-$Si$) | 1.086 | 0.356 | 10.00 |

The surface roughness(root mean square(RMS)) was nearly by all thin films of RR-P3HT around $0.80\ nm < RMS < 1.05\ nm$. The divergence comes from the fits, but also the samples themself vary a bit. The roughness was cross checked by Dr. Bettina Friedel via AFM in Cambridge, England. The samples were made with a concentration of 8.5 $g/l$ of P3HT in chlorbenzene on $SiO_2$ with the standard parameters.
The roughness values out of AFM are about $0.75\ nm < RMS < 0.90\ nm$. This nice accordance depict the potential of the XRR. It could be that the RMS out of the XRR provides a better estimation, because the bigger area is regraded with the X-ray beam than in AFM.

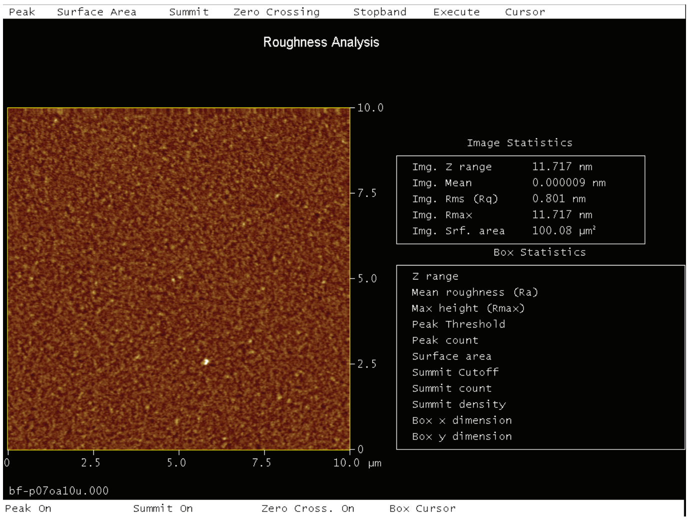

```
Image Statistics
Img. Z range       11.717 nm
Img. Mean          0.000009 nm
Img. Rms (Rq)      0.801 nm
Img. Rmax          11.717 nm
Img. Srf. area     100.08 µm²
Box Statistics
Z range
Mean roughness (Ra)
Max height (Rmax)
Peak Threshold
Peak count
Surface area
Summit Cutoff
Summit count
Summit density
Box x dimension
Box y dimension
```

Figure 3.4: AFM - picture of a P3HT film. $RMS = 0.80\ nm$.

### 3.1.2 X-ray Reflectivity of F8BT

F8BT has far less reports in literature than P3HT. Experiments were made to find a suitable solvent for F8BT. It turned out that the chlorine based solvents were better than the aromatic hydrocarbon ones, like Xylene. To have similar solvents for both polymers, chlorobenzene was chosen for F8BT to.

The obtained $\rho_m$ varies, but is around $\rho_m = 1.12\ g/cm^3$ for most of the time. The fits of F8BT scans can't disclose the true nature of interfaces uniquely, [2].

Without the additional information of the AFM, it would be hard to determine the interface roughness and mass density. If the fit of Fig. 3.5 is compared with the Fig. 4.1 appendix, it is had to decide, which fit is the right one.

But AFM pictures suggest that the surface roughness of the F8BT should be around $RMS = 0.34\ nm$, see Fig. 3.4. Because the surface roughness of AFM and XRR( Fig. 3.5, Fig. 3.6) must fit, the fits like Fig. 4.1 were neglected and be considered as wrong. Interesting is also, that all XRR-fits with the right surface roughness, have twice time bigger interface roughness than it is for P3HT, it is just a suspicion, but this could be correlated to the high $M_{w\ F8BT} = 150\ kg/mol$.

Fig. 3.5 shows F8BT on top of $SiO_2$. The concentration of the solution was $8.3\ g/l$. Here the parameters kept free and the surface roughness is coming in the right order of the AFM measurements, also the curve fits better than in Fig. 4.1. Measurement parameters were: range: $2\theta = 0 - 8°$, step size:0.005°, int.time: $2\ s$.

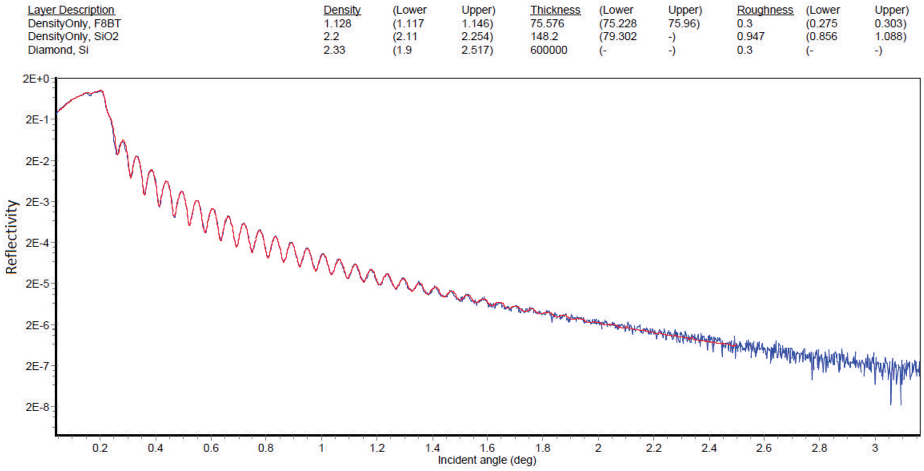

| Layer Description | Density | (Lower | Upper) | Thickness | (Lower | Upper) | Roughness | (Lower | Upper) |
|---|---|---|---|---|---|---|---|---|---|
| DensityOnly, F8BT | 1.128 | (1.117 | 1.146) | 75.576 | (75.228 | 75.96) | 0.3 | (0.275 | 0.303) |
| DensityOnly, SiO2 | 2.2 | (2.11 | 2.254) | 148.2 | (79.302 | -) | 0.947 | (0.856 | 1.088) |
| Diamond, Si | 2.33 | (1.9 | 2.517) | 600000 | (- | -) | 0.3 | (- | -) |

Figure 3.5: The XRR-data is plotted blue and the fit red. The scan was performed on F8BT on $SiO_2$.

In Fig. 3.6 F8BT is spin-coated on top of native $Si$ with a concentration of 7.8 $g/l$. Also here the surface roughness is in good accordance with the AFM. Measurement parameters were: range: $2\theta = 0 - 6.5°$, step size:0.01°, int.time: 5 $s$.

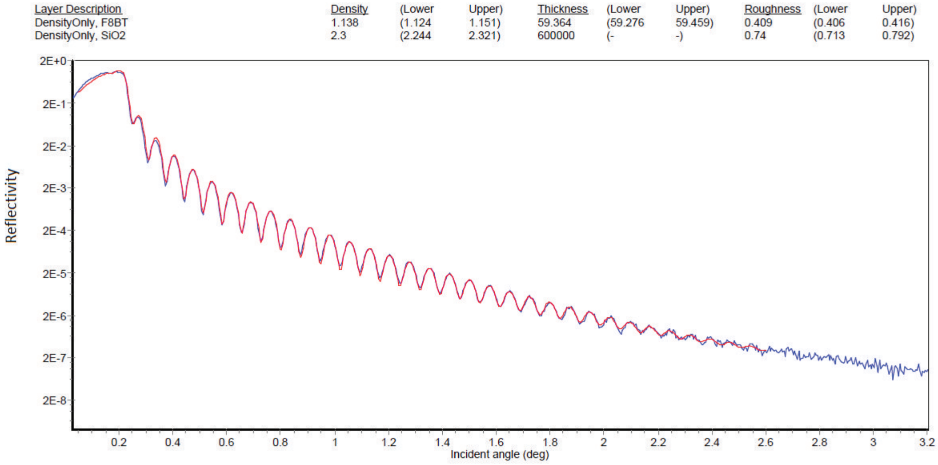

| Layer Description | Density | (Lower | Upper) | Thickness | (Lower | Upper) | Roughness | (Lower | Upper) |
|---|---|---|---|---|---|---|---|---|---|
| DensityOnly, F8BT | 1.138 | (1.124 | 1.151) | 59.364 | (59.276 | 59.459) | 0.409 | (0.406 | 0.416) |
| DensityOnly, SiO2 | 2.3 | (2.244 | 2.321) | 600000 | (- | -) | 0.74 | (0.713 | 0.792) |

Figure 3.6: The XRR-data is plotted blue and the fit is red. The scan was performed on F8BT on n-$Si$.

The $\rho_e$ were calculated the same way like for P3HT. The values are summed up in. Tab. 3.3.

Table 3.3: With the XRR fit of F8BT single layer the mass density($\rho_m$) was calculated. [57] can provide $\delta$ and $\beta$ if the chemical structure and $\rho_m$ is known. The electron density and scattering length density($\rho$) was calculated.

| Polymer | $\rho_m$ / $[g/cm^3]$ | $\rho_e/[1/\mathring{A}^3]$ | $\rho/[10^{10}cm^{-2}]$ |
|---|---|---|---|
| F8BT($SiO_2$) | 1.128 | 0.368 | 10.37 |
| F8BT(n-$Si$) | 1.138 | 0.371 | 10.47 |

The scattering length densities of F8BT and P3HT is very similar for $Cu_{K_\alpha}$ and have just for the best case a difference of ≈ 10%. If P3HT on native-$Si$ is regarded the difference decrease to ≈ 6%.

To Enclose this section: The $\rho_{m\ P3HT} = 1.060 \pm 0.040\ g/cm^3$ and for F8BT lays around $\rho_{m\ F8BT} = 1.12 \pm 0.050\ g/cm^3$(for both polymers these values depend strongly on the substrate) no matter how often XRR-scans are performed and analysed the values will be most of the time between these borders. The maximum contrast of the determined $\rho_m$ of F8BT and P3HT is about ≈ 13% in terms of scattering length densities($\rho$).

The average value of contrast is less than ≈ 5% in terms of scattering length density. Now the question arises, if such low values of contrast are enough to separate both polymers layer in a bilayer stack with X-rays?

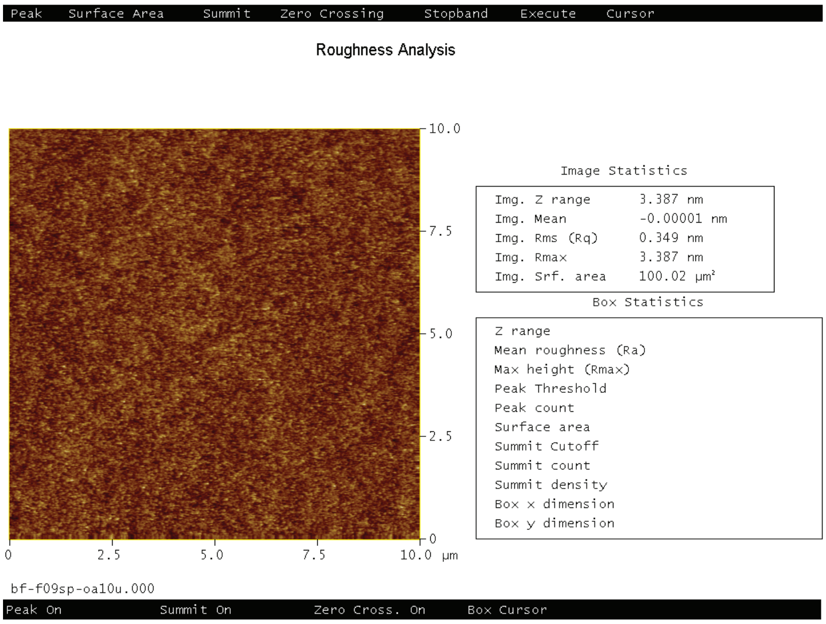

Image Statistics

| | |
|---|---|
| Img. Z range | 3.387 nm |
| Img. Mean | -0.00001 nm |
| Img. Rms (Rq) | 0.349 nm |
| Img. Rmax | 3.387 nm |
| Img. Srf. area | 100.02 µm² |

Box Statistics

Z range
Mean roughness (Ra)
Max height (Rmax)
Peak Threshold
Peak count
Surface area
Summit Cutoff
Summit count
Summit density
Box x dimension
Box y dimension

Figure 3.7: AFM - picture of a F8BT film. $RMS = 0.35\ nm$.

## 3.2 Bilayer of P3HT/F8BT

The XRR discovered a interesting behaviour of the reflectivity curve. Normally in multilayer stack a so called 'Schwebung' is expected, but for the P3HT/F8BT layers two different oscillations occurred, see for this Fig. 3.8. The fringes at low incident angles($\alpha_i = 2\theta/2$) displays the thickness of both layers together and for higher angles different Kiessig-fringes showed up. Variation of the thickness of the P3HT-layer, displayed that those Kiessig-fringes for higher angles belong to P3HT.
Just regarding the reflectivity coefficients, like in Sec. 1.12, means that for higher angles $3° \leq 2\theta \leq 6°$ the reflected intensities from the P3HT are dominant. That means the P3HT fringes in the bilayer are a qualitative hint for the morphology of the interface, because two reflections or intensities are needed to see this layer. The first must come from the P3HT/F8BT interface and the second from substrate/P3HT interface otherwise no fringes would occur in the XRR.
The reflectivity curve in Fig. 3.8 shows that both oscillation are strong pronounced. For low angles the XRR can not distinguish the two polymers and the fringes are correlated to the collective thickness. For higher angles those fringes disappear and the P3HT-fringes become stronger. The measurement parameters were: range: $2\theta = 0 - 6°$, step size:0.002°, int.time: 1 $s$.

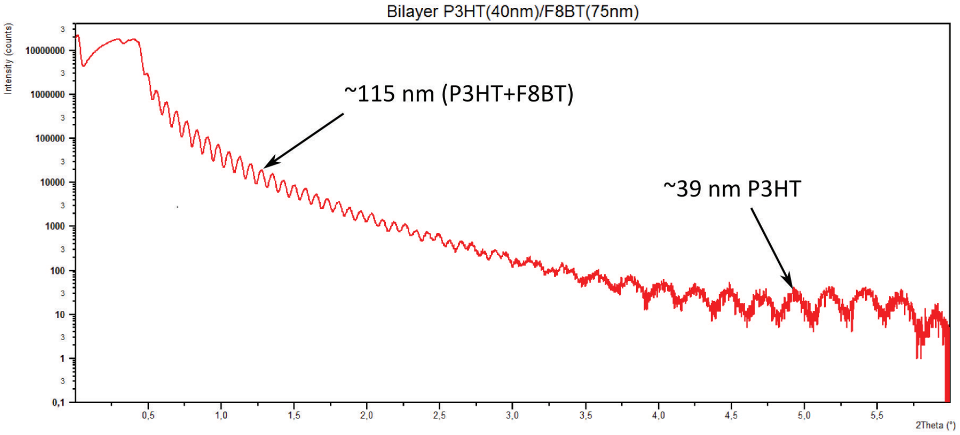

Figure 3.8: Typical XRR-curve from a bilayer.

### 3.2.1 Fitting of the Bilayer

Because of the Bragg-peak from P3HT at $2\theta = 5.4°$ it is not easy to fit the data, but still some knowledge was gained.
Additionally to fit the P3HT-fringes a very low interface roughness, compared to the surface roughness is needed to model the data. This lays maybe on the weak contrast among the polymers, which can lead to an electron density profile like it is shown in Fig. 3.9, right hand side.

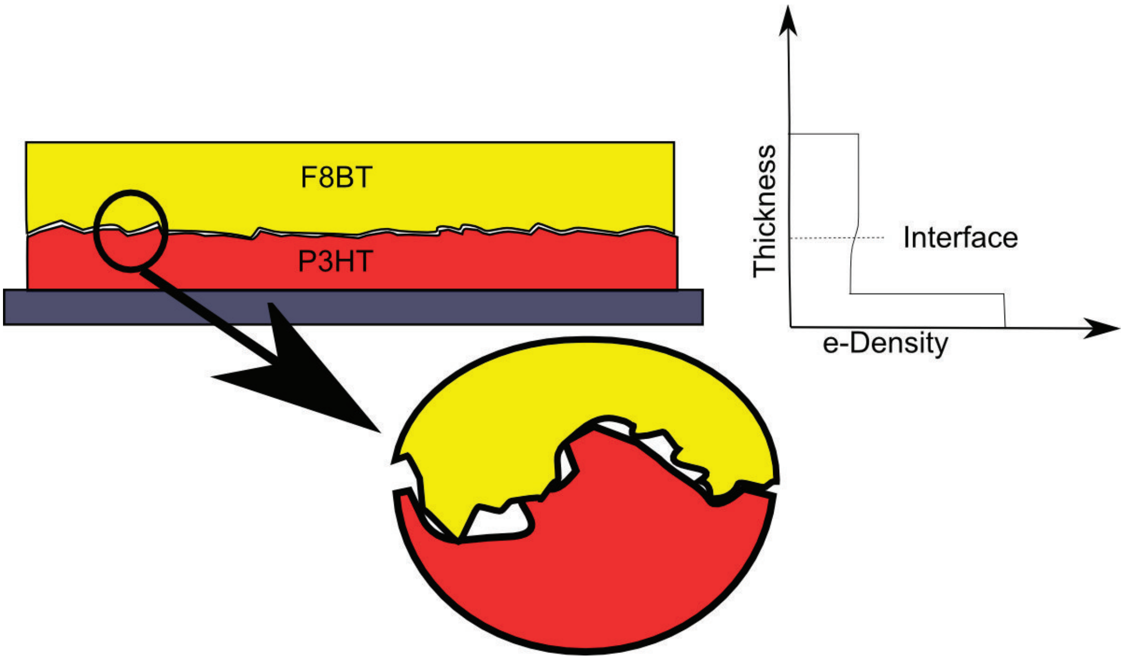

Figure 3.9: Schematic picture of the interface roughness and the electron density profile of the polymers.

Fig. 3.9 shows both polymers and a detailed look at the interface how it may look like. The F8BT has a surface roughness of about 0.3 $nm$ and roughness at the polymer/substrate intersface of 0.7 $nm$ according to the XRR-fit in Fig .3.6. When the F8BT comes of the glass substrate in the floating process, there will be a certain amount of roughness on the bottom side of the polymer, which should be in the range of the roughness of the polymer/substrate interface from the perviously mentioned XRR-fit.
By the deposition of F8BT the polymer is laid softly on the P3HT, what forms an interface which might looks like the picture in Fig. 3.9 below. There are areas where both polymers in contact and regions without, additionally the polymer interfaces will mesh into one another. This could led to a smoother electron density gradient at the interface, which causes the lack of 'Schwebung' in the XRR.
For a steeper incident angle the gradient becomes less diffuse at the contact area of both polymers, which could cause higher reflectivity coefficients and then the P3HT-fringes appears.

## 3.3 Heating Series of Bilayer with X-ray Reflectivity

All annealing experiments were done with the Anton Paar DHS 900 in-situ under inert conditions($N_2$). Different temperatures were tried: 80°$C$, 85°$C$, 90°$C$, 95°$C$, 100°$C$, 110°$C$, 130°$C$, 140°$C$ and 160°$C$. For the heating series a temperature with not so rapid change was need. At 130°$C$ and 140°$C$ the fringes decreased far to fast, the time scale was just tenths of minutes and lower temperature, like 80°$C$ and 85°$C$ showed just after hours a slight decrease of the P3HT-fringes. 90°$C$, 100°$C$ and 110°$C$ were chosen for further investigation.

Glass transitions of both polymers were higher than those temperatures, but still a change of the bilayer was detected. Now questions rises, if this change is connected to evaporation from water at the interface? A good point for this argumentation is that the used temperatures are very close to the boiling point of water.

For water the electron density is $\rho_e = 0.3362\ 1/\AA^3$ and scattering length density is $\rho = 9.47 \cdot 10^{10}\ 1/cm^2$, [57] and are very close to P3HT. Therefore it would be hard for the XRR to distinguish between the polymer and a thin water layer on top. But if the the water layer would have a thickness of several nanometers, why the solar cells are then working? Because a thick intermediate layer should reduce very effectively the contact between polymers and a thickness of these size should be some how seen in the XRR, but there is no sign of an additional layer at all.

When there is water in the inside the bilayer, it is definitely not more than some layers or maybe just a monolayer of $H_2O$ and for such a thin layer the XRR is not so sensible, that such strong effects could be seen, also the weak contrast to the P3HT supports this commend.

Another possibility could be that the water and P3HT froms a layer together though the lack of contrast. In Fig. 3.10 XRR-measurements of a bilayer at 100°$C$ for different annealing times is shown, which are plotted as reflectivity of $2\theta$, marked is the relaxation. Subplot below: $Iq^4$ over $q_z$. range: $2\theta = 0 - 6.5°$, step size:0.01°, int.time: 5 $s$

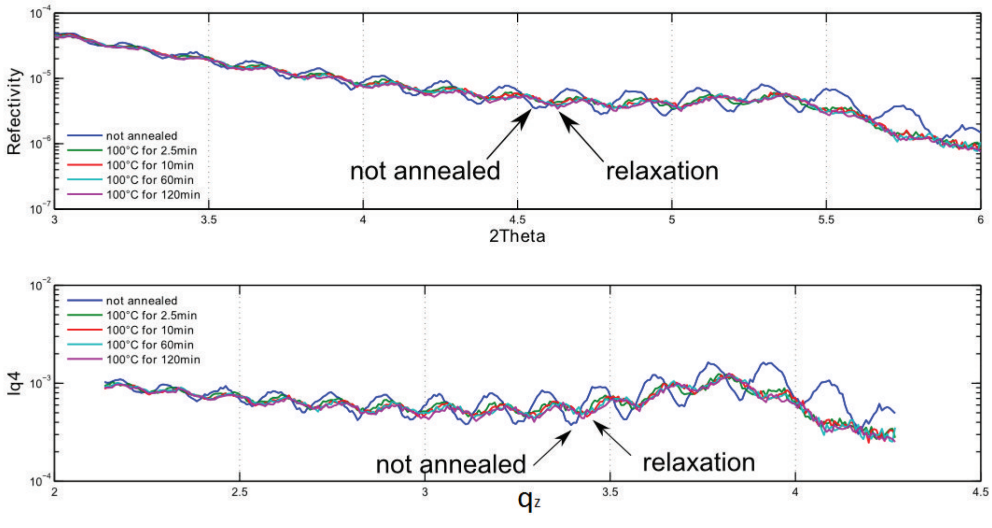

Figure 3.10: XRR-scans of the 100°$C$ series.

If the X-ray would be detect the the $H_2O$ and P3HT as a common layer, a constant decrease of thickness would be logical, but the fringes just change ones and than there thickness stays constant for longer annealing times, see Fig. 3.10.

The change of fringes from not annealed to the first annealing is connected to a relaxation of the polymer. Through spin-coating the polymers are in a non equilibrium state and a rise in temperature make the polymer chains more flexible to find a more stable state. At all temperatures relaxations were observed. The P3HT-fringes of the not-annealed bilayer become smaller with annealing. The change was normally of about 0.5 *nm* and become faster with higher temperatures. This phenomena was also observed at 80°$C$.

Also both polymers are highly hydrophobic, which for sure reduces the water to a minimum at the interface.

### 3.3.1 Fitting of X-ray Reflectivity from Temperature treated Bilayers

It turned out that the annealing at 90°, 100° or 110° for a certain time reduces the reflected intensity from the interface, which appears as decreasing P3HT-fringes. A reduction of intensity is mostly connected with an increase of roughness, so the heating series in the following sections, shows a constant decrease of the P3HT-fringes with annealing time, see Sec. .

The fitting of a bilayer at four different annealing stages is depicted in Fig. 3.11 - a) not annealed, b) annealed for 2.5 *min* at 100°$C$, c) annealed for 8 *min* at 100°$C$ and d) annealed for 40 *min* at 100°$C$. The fitting was done with the PANalytical X-pert software. Because of the Bragg-peak of P3HT at $\alpha_i = 2.7°$ and that the P3HT-fringes are very noisy and have quiet low intensity the fitting was hardly possilbe. Fig. 3.11 shows a simulation(red curve) of the bilayer. Nevertheless the simulations reveal an interesting result. The P3HT-fringes are just reproducible with a very low interface roughness, see Fig. 3.11 (a).

During the annealing process the fringes disappear, which could be simulated with an increase of roughness between P3HT and F8BT, see therefore Fig. 3.11 (b), (c) and (d). The order of interface roughness depends on the anealing time and ranges from no roughness at all to a nanometer according to the simulations.

Measuring parameters where for all scans in Fig. 3.11 the same: range: $2\theta = 0 - 6.5°$, step size:0.01°, int.time: 5 $s$

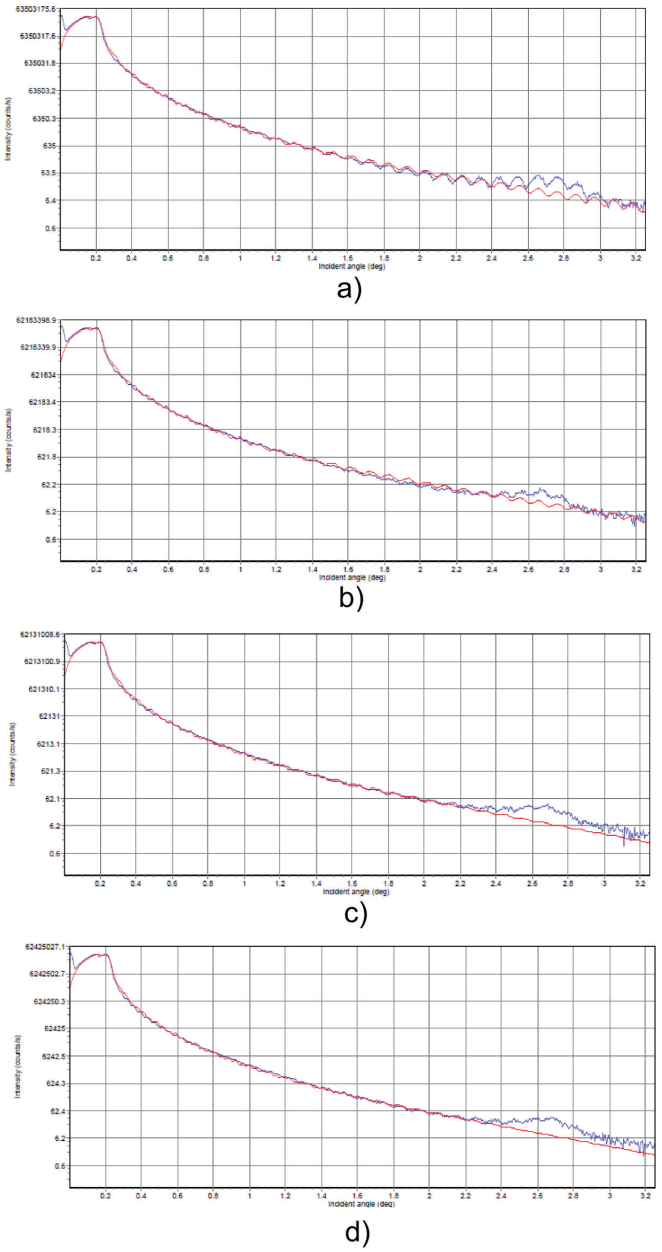

| Model: | Density: | Thickness: | Roughness |
|---|---|---|---|
| F8BT | 1.19 g/cm$^3$ | 74 nm | 0,9 nm |
| P3HT | 1.08 g/cm$^3$ | 42 nm | changed |
| Si | 2.30 g/cm$^3$ | infinite | 0.35 nm |

Figure 3.11: The XRR-scans are plotted in blue and the simulations are shown in red. a) has a roughness of $RMS = 0\ nm$, not annealed, b) $RMS = 0.25\ nm$ annealed for 2.5 $min$ at 100°$C$, c) $RMS = 0.5\ nm$ annealed for 8 $min$ at 100°$C$ and d) $RMS = 0.6\ nm$ annealed for 40 $min$ at 100°$C$.

### 3.3.2 X-ray Reflectivity of Bilayer annealed at $90°C$

All scans were done with the same setup regrading heating and scan parameters see Sec. 4.1. For each temperature one bilayer sample was prepared and annealed for different time scales. Fig. 3.12 shows the XRR-scan of the $90°C$ series over the whole range. The different scans were all divided by their maximum reflection at $\alpha_c$ and are plotted semi-logarithmically over $\alpha_i$. At $90°C$ the Kiessig-fringes of P3HT change hardly. Just for very long annealing times fringes begin to disappear.

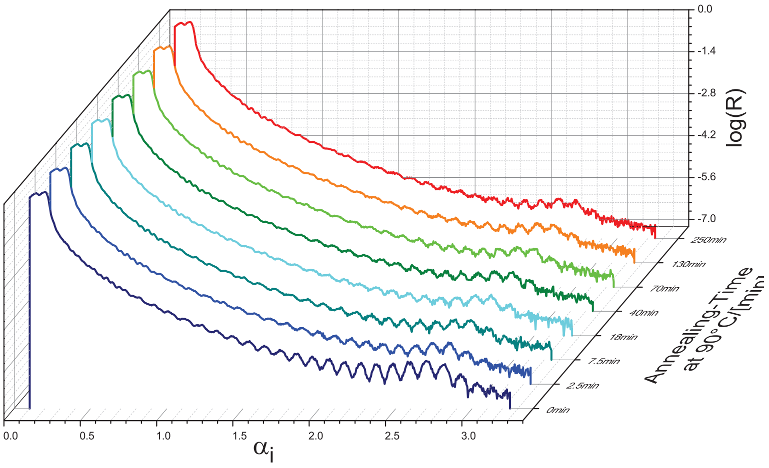

Figure 3.12: Heating series of $90°C$ in a waterfall plot.

Fig. 3.13 gives a more detailed look at the P3HT-fringes. Here it is clearly to see that the fringes hardly changes with annealing time. Measurement parameters were: range: $2\theta = 3 - 6.5°$, step size:0.01°, int.time: 25 $s$.

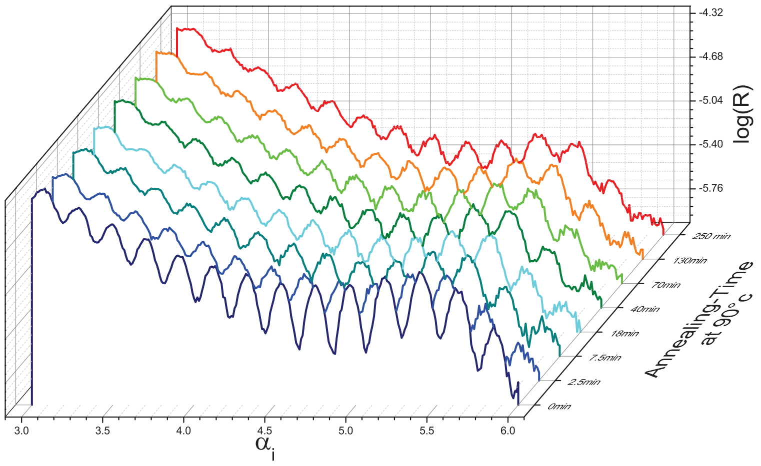

Figure 3.13: XRR-scan of the P3HT-fringes with a higher integration time.

The $Iq^4$-plots of the $90°C$ series is plotted in Fig. 3.14. Here the reflectiity curve is multiplied with the $q^4$ that just the decay from the roughness is displayed. The steeper this plot is the rougher is the sample.

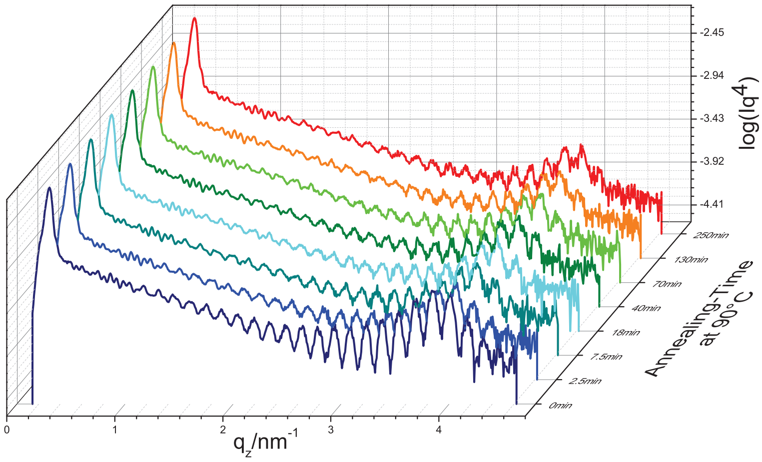

Figure 3.14: A $Iq^4$ over $q$ plot of the previous scan.

### 3.3.3 X-ray Reflectivity of Bilayer annealed at $100°C$

The setup was identical with the $90°C$ series. Again a scan over the whole region is shown, it is clearly to see in Fig. 3.15 that the P3HT decay faster at $100°C$. Measurement parameters were: range: $2\theta = 0 - 6.5°$, step size:0.01°, int.time: $5\ s$

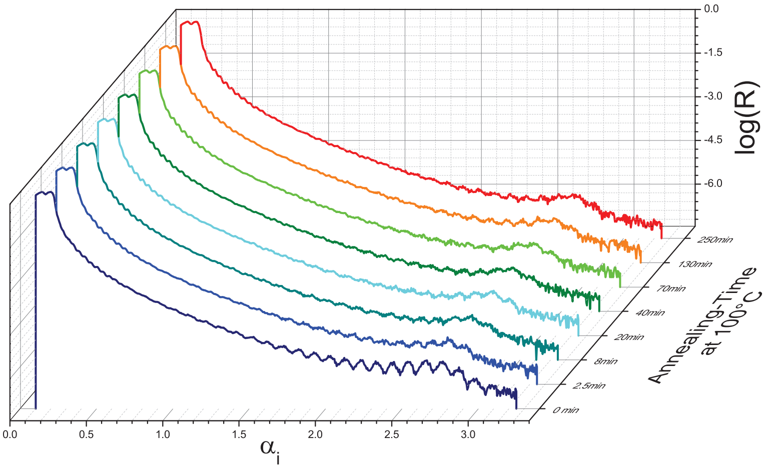

Figure 3.15: Heating series of $100°C$.

Closer look on the P3HT-fringes with a higher intergration time. In Fig.3.15 the P3HT were nearly gone, with a higher integration time they appear nicely. The change is stronger. Measurement parameters were: range: $2\theta = 3 - 6.5°$, step size:0.01°, int.time: $25s$.

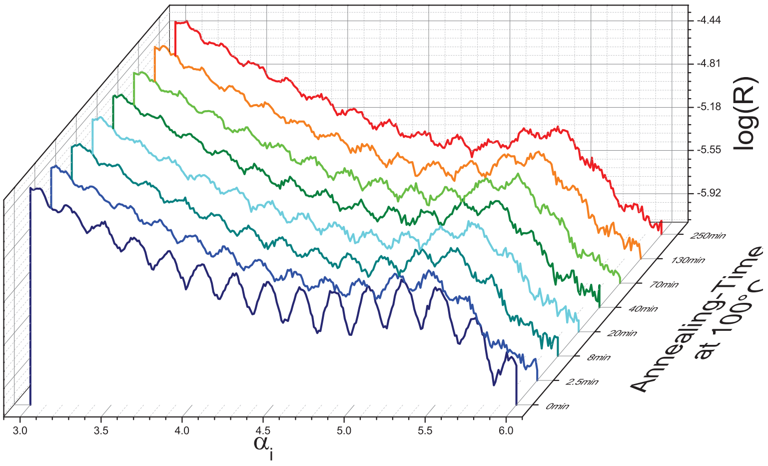

Figure 3.16: A higher integration time is applied for a more detailed scan.

The $Iq^4$-plots of the $100°C$ series is plotted in Fig. 3.17. Also here the decay of the fringes is clearly to see.

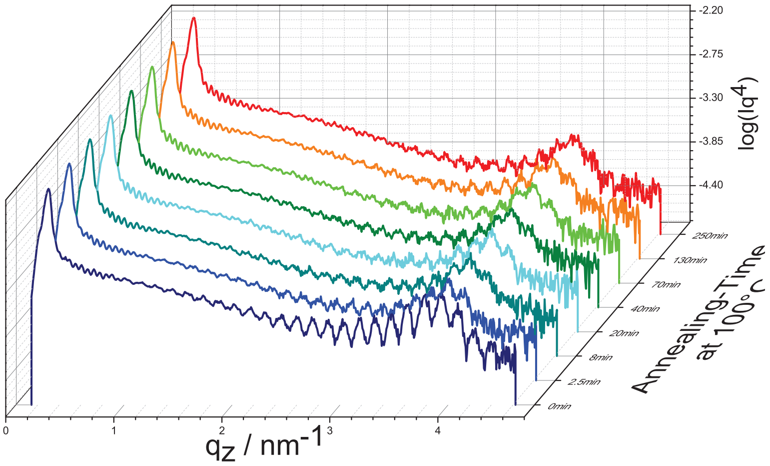

Figure 3.17: A $Iq^4$ over $q$ plot of the previous scan, Fig.3.15, is depicted.

### 3.3.4 X-ray Reflectivity of Bilayer annealed at $110°C$

$110°C$ was the highest temperature at which an annealing serie was done. The results are show in Fig. 3.18. At this temperature the fringes disappeared so quickly that the time scale was changed. The effects of annealing were for 110°$C$ the strongest. Measuring parameters were: range: $2\theta = 0 - 6.5°$, step size:0.01°, int.time: 5 $s$.

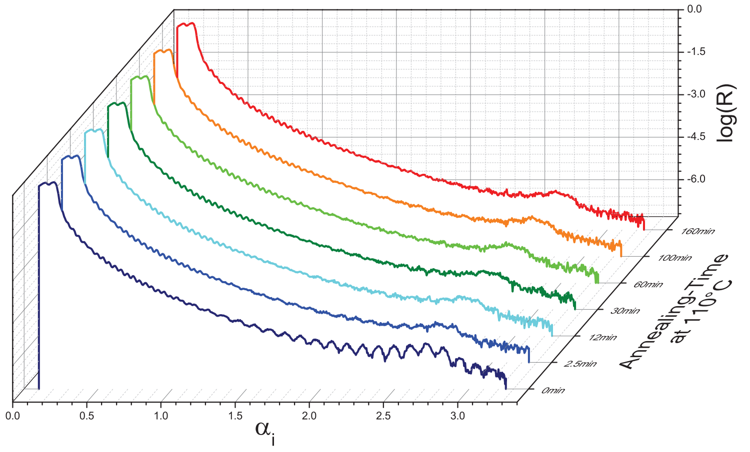

Figure 3.18: Heating series of 110°$C$.

Here also the change for longer integration times are very strong, see Fig. 3.19. The annealing time were change, even with a higher integration time the fringes are nearly gone for 160 $min$. Measuring parameters were: range: $2\theta = 3 - 6.5°$, step size:0.01°, int.time: 25 $s$.

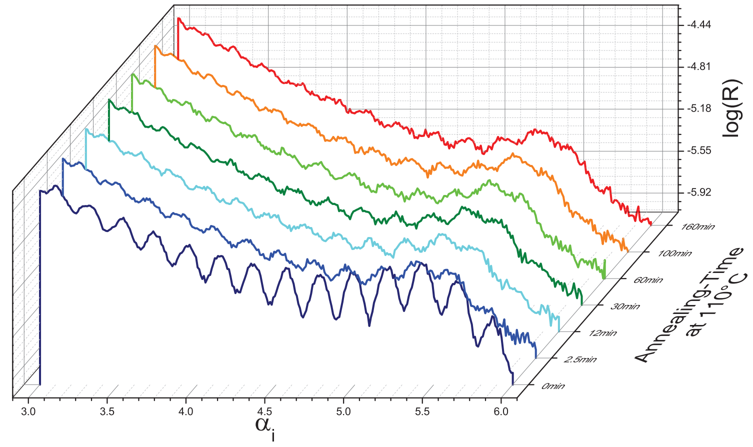

Figure 3.19: A higher integration time is applied for a more detailed scan.

The $Iq^4$-plots of the 110°$C$ series is plotted in Fig. 3.20. Here the reflectity curve is multiplied with the $q^4$ that just the decay from the roughness is displayed. The steeper this plot is the rougher is the sample.

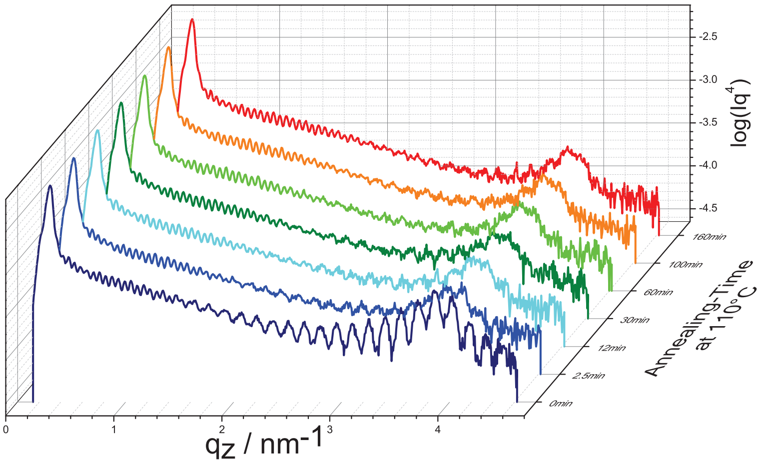

Figure 3.20: A $Iq^4$ over $q$ plot of the previous scan.

### 3.3.5 Numerical Analysis of the P3HT-Fringes

The program works as follows: First the minimas out of the XRR-scan for higher angles are searched. To do this the data was cut into equal intervals for optimisation. The obtained positions of the minimas were used to find the equal ones in the $Iq^4$ - data. The $Iq^4$-data is easier to fit, because the $q_z^{-4}$ decay is corrected. Now a fit was made for every fringe with a simple sinus model:

$$model_{fringe} = c_1 + c_2 sin(c_3 q_z)$$

$c_1$ and $c_2$ must be included to consider the back round and the decay of roughness. $c_3$ is correlated to the wave length and the thickness. The matlab function *nlinfit* optimized all three constants. Later a integration with the help of $model_{fringe}$ was done. This was done for every fringe individually over all annealing steps. Then the areas were compared and also fitted to compare the decay. The mathematical model is:

$$model_{area} = c_1 + c_2 \cdot e^{\frac{c_3}{c_4+t}}$$

$c_1$, $c_2$, $c_3$, $c_4$ are constants and $t$ is the annealing time. Sometimes the data was a hard do fit below a $q_z = 3.5\,\mathring{A}^{-1}$, because of noise. Still a the results of the XRR were reproducible also numerically . The conclusion was that changes of the P3HT fringes become stronger with higher annealing times. Fig. 3.21 displays one example of the fringes decay for every temperature, $90°C$ a), $100°C$ b) and $110°C$ c). For the calculation the area development below each was regarded fringe during the annealing process.

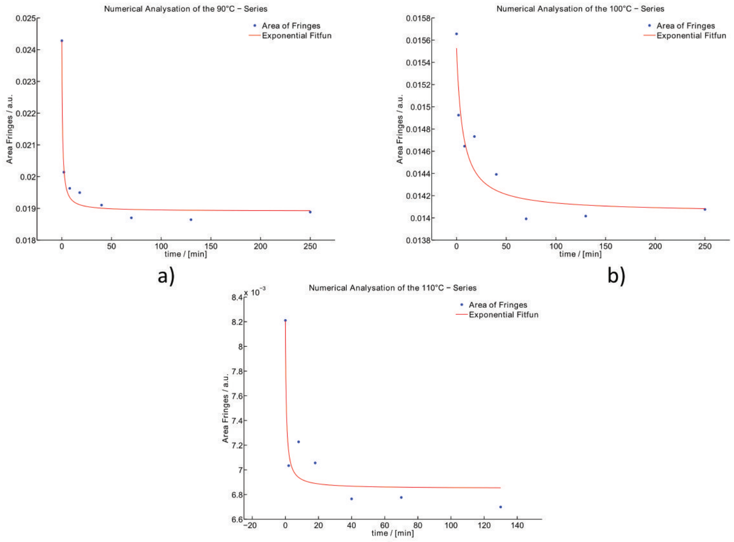

a) b)

c)

Figure 3.21: Decay of fringes at 90°$C$ a), 100°$C$ b) and 110°$C$ c).

## 3.4 Results from Neutron Reflectivity

Calculations of the scattering length density for neutrons showed a good contrast of $\approx 50\%$ theoretically and as well $\approx 50\%$ in the experiment, see Tab. 3.4. The values are calculated with, [58].

Table 3.4: The scattering length density($\rho$) were obtained with a calculator, provided by [58]. $\rho_m$ is the mass density, the data is from the XRR-fits and $\rho_{exp}$ is the scattering length density from the experiment.

| Material | $\rho_m$ / $[g/cm^3]$ | $\rho$ / $[10^{10} cm^{-2}]$ | $\rho_{exp}$ / $[10^{10} cm^{-2}]$ |
|---|---|---|---|
| P3HT | 1.06 | 0.651 | 0.62 |
| F8BT | 1.12 | 1.253 | 1.02 |
| Water | 1.00 | 0.560 | - |
| Silicon Oxid | 2.21 | 3.490 | 3.47 |

Sample preparation was differently from XRR. The substrate itself was also native $Si$ with 50 $mm$ in diameter and a hight of 5 $mm$. Here for every annealing time a single sample was made. That's why the thickness varying a bit from measurement to measurement. It was also just possible to examine one temperature series(100°C).

The big advantage of neutron reflectivity was the high contrast between the P3HT and F8BT. See Tab. 3.4. The fits of the neutron data was done with the free software *Motofit*. Neutron reflectivity data showed the following:

- A difference in scattering length density was determined.
- Both polymers could be separated in NR of the bilayer.
- The surface effects the first part of the spectrum.
- Surface roughness of the single layers fit with the results of the XRR.
- The surface roughness of the bilayer samples is much higher than in the XRR.
- The interface roughness hardly changes over the whole annealing periode at $100°C$.

Tab. 3.5 contain the fit results of the single layers and several annealing steps at $100°C$ of the bilayer samples. The data of the single layer fit are in very good accordance to the X-ray reflectivity data, regarding the surface and interface roughness. Nevertheless the data of the bilayer samples are very different from the X-ray reflectivity data. The surface roughness of the bilayer is much higher than it should be and the interface roughness of the polymers don't change with annealing time.

This is contradictory to the X-ray data, because there a constant change was observed, Sec. 3.3.2. It seems that for this high divergence comes from the floating process. When the F8BT begins to lay down on the P3HT the floated film can not preserve enough tension to push the water out from the interface. Therefore big water residuals were common during the preparation. This water residuals strech the F8BT and induce a local morphological change. The geometry of the neutron beam allows to illuminate a bigger sample area than in X-ray reflectivity. This leads to a sensibility for the traces of the water residuals, which increases the effective surface roughness.

Additionally a higher surface roughness reduces the effects of the interface and lead to a faster fringe decrease in the neutron reflectivity spectra. The consequnece of those effects is a bad data from the interface, which results in a nearly constant interface roughness. The results of the fits are summed up in Tab.3.5:

Table 3.5: $\sigma$ is the roughness and the uncertainty is about $\Delta\sigma = \pm 0.3\ nm$ and $\rho$ the scattering length density. The fitting software was provided from the Hahn-Meitner Institute, Berlin and is called Parrat32.

| Material | Thickness/$[nm]$ | $\sigma/[nm]$ | $\rho/[10^{10}cm^{-2}]$ |
|---|---|---|---|
| Single Layer | | | |
| P3HT | 40.3 | 1.3 | 0.65 |
| native Silicon | 1.2 | 0.5 | 3.40 |
| F8BT | 68.3 | 1.6 | 1.02 |
| native Silicon | 1.9 | 0.5 | 3.40 |
| Bilayer not annealted | | | |
| F8BT | 62.6 | 4.0 | 1.05 |
| P3HT | 39.8 | 1.4 | 0.62 |
| native Silicon | 1.1 | 0.3 | 3.42 |
| Bilayer annealed for 2 $min$ | | | |
| F8BT | 63.3 | 3.2 | 1.08 |
| P3HT | 42.4 | 1.5 | 0.60 |
| native Silicon | 1.7 | 0.2 | 3.49 |
| Bilayer annealed for 8 $min$ | | | |
| F8BT | 61.7 | 4.7 | 1.10 |
| P3HT | 42.7 | 1.6 | 0.62 |
| native Silicon | 1.7 | 0.7 | 3.50 |
| Bilayer annealed for 40 $min$ | | | |
| F8BT | 63.3 | 3.7 | 1.04 |
| P3HT | 43.2 | 1.4 | 0.62 |
| native Silicon | 1.6 | 0.5 | 3.42 |
| Bilayer annealed for 130 $min$ | | | |
| F8BT | 64.4 | 4.5 | 1.07 |
| P3HT | 42.0 | 2.5 | 0.62 |
| native Silicon | 1.3 | 0.2 | 3.42 |
| Bilayer annealed for 250 $min$ | | | |
| F8BT | 63.6 | 4.8 | 1.16 |
| P3HT | 43.2 | 2.1 | 0.62 |
| native Silicon | 1.7 | 0.4 | 3.42 |
| Material | Thickness/$[nm]$ | $\sigma/[nm]$ | $\rho/[10^{10}cm^{-2}]$ |

### 3.4.1 Neutron Reflectivity Data vs. X-ray Reflectivity Data

Beside the NR-measurements also XRR-scans were performed on the same samples to depicte the difference between both methods.

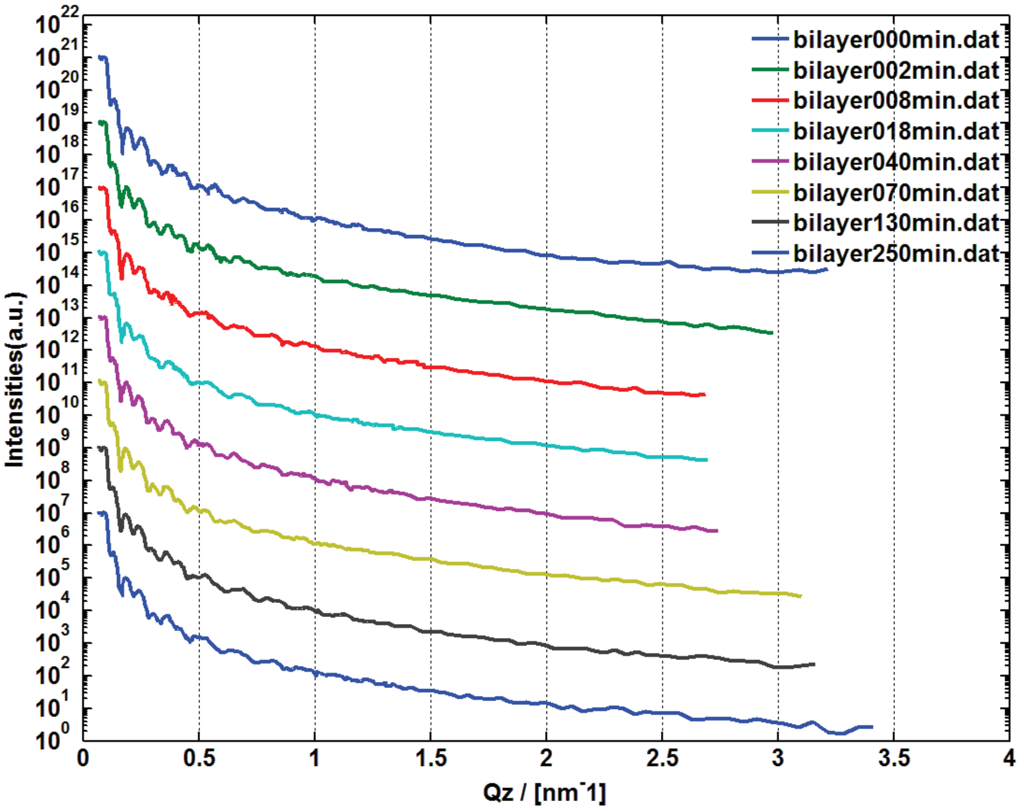

Figure 3.22: NR-data of the J-PARC bilayer samples at 100°$C$. Through all samples the fringes are visible and give a good opportunity to obtain good information out of fits.

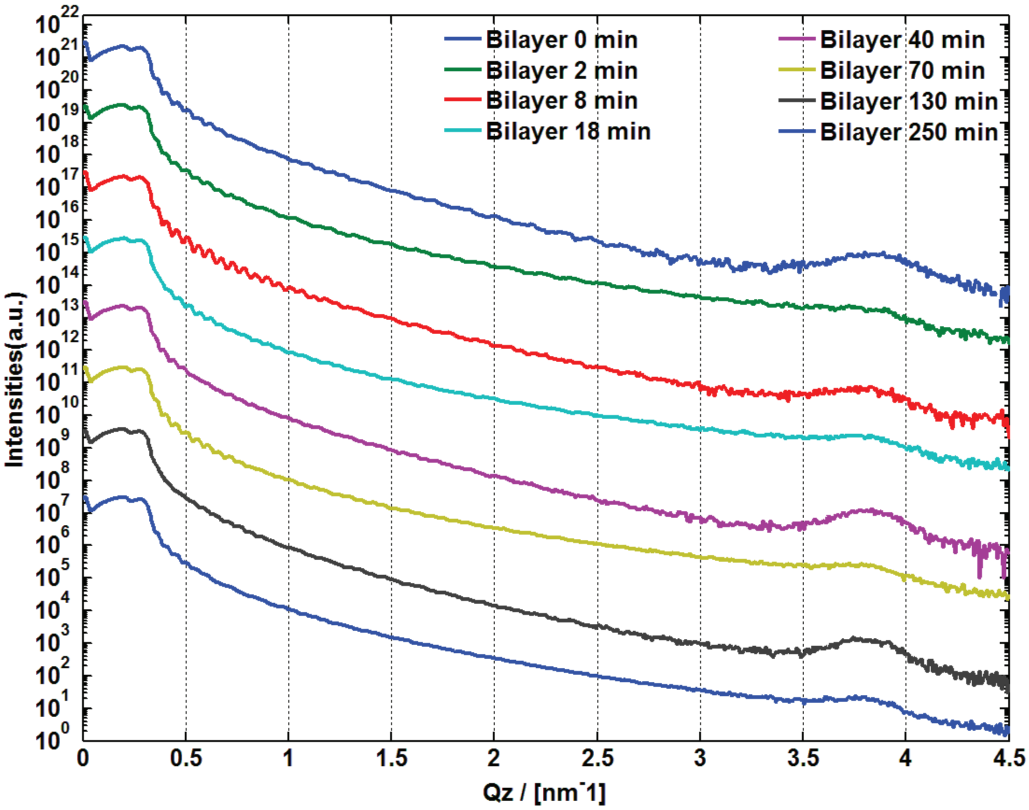

Figure 3.23: XRR-data of the J-PARC bilayer samples at 100°$C$. Here the P3HT hardly appears. In general the fringes are just weak pronounced, therefore a fit of the data was not perfect.

## 3.5 Gracing Incident X-ray Diffraction - Measurements

The GIXD investigations were done on the Bruker Discovery D8 and the setup was:

- Incident Side:
  - Divergence Slit: 0.1 $mm$
  - Primary Soller Slit: 2.5°
- Diffracted Side:
  - Secondary Soller Slit: 2.5°
  - Anti-Scatter Slit: 0.35 $mm$

Measurements were done with the J-PARC sample to gain additional data over the lateral correlations of the bilayer and its changes over annealing time. Results are in Fig. 3.24 demonstrated. The P3HT Bragg-peak could be identified at $2\theta = 5.4°$ or $q = 0.38$ $\AA^{-1}$, the Debye-Scherrer ring indicates polycrystallinity of P3HT, additionally the peak of P3HT is near the specular condition. Most of the crystallite P3HT has a in-plane order, were the hexyl groups are docked to the substrate, see Fig. 3.24.
F8BT has a peak at about $q = 0.43$ $\AA^{-1}$. Interesting is that the F8BT shows up near the specular region, because during all XRR-scans a specular peak of F8BT was never observed, below a temperature of $130°C$. The rod, which is marked at a $q_x = 1.7\AA{-}^{-1}$, comes from the planar parallel distance between the thiophene rings, which is about 3.7 $\AA$ or $q = 1.7$ $\AA^{-1}$, see Fig. 3.24. The distance of the P3HT backbones is in accordance with this result. The first look on the GIXD-maps show no big change in the crystallinity of both polymers over the whole temperature treatment. A further look on the Yoneda region is necessary, marked in Fig. 3.24 corner above left side.
Fig. 3.25 depict a weak in plane order of F8BT(peak 5.3 $\AA^{-1}$ and 4.4 $\AA^{-1}$), but both peaks are very weak. This can be correlated to the $M_w = 150$ $kg/mol$ of F8BT, that causes a weakly crystalline F8BT layer. The only clear peak is at 3.7 $\AA^{-1}$ from the polythiophene back bone of P3HT and it changes over the annealing time. For 2 $min$ the peak decrease significantly, maybe it is the same relaxation as it was observed in the XRR. Maybe the polythiophene back bone peak is a hint, that also temperatures like $T_{ann} < T_g$ enhance movement of P3HT.
All in all the GIXD shows no improve of crystallinity of F8BT.

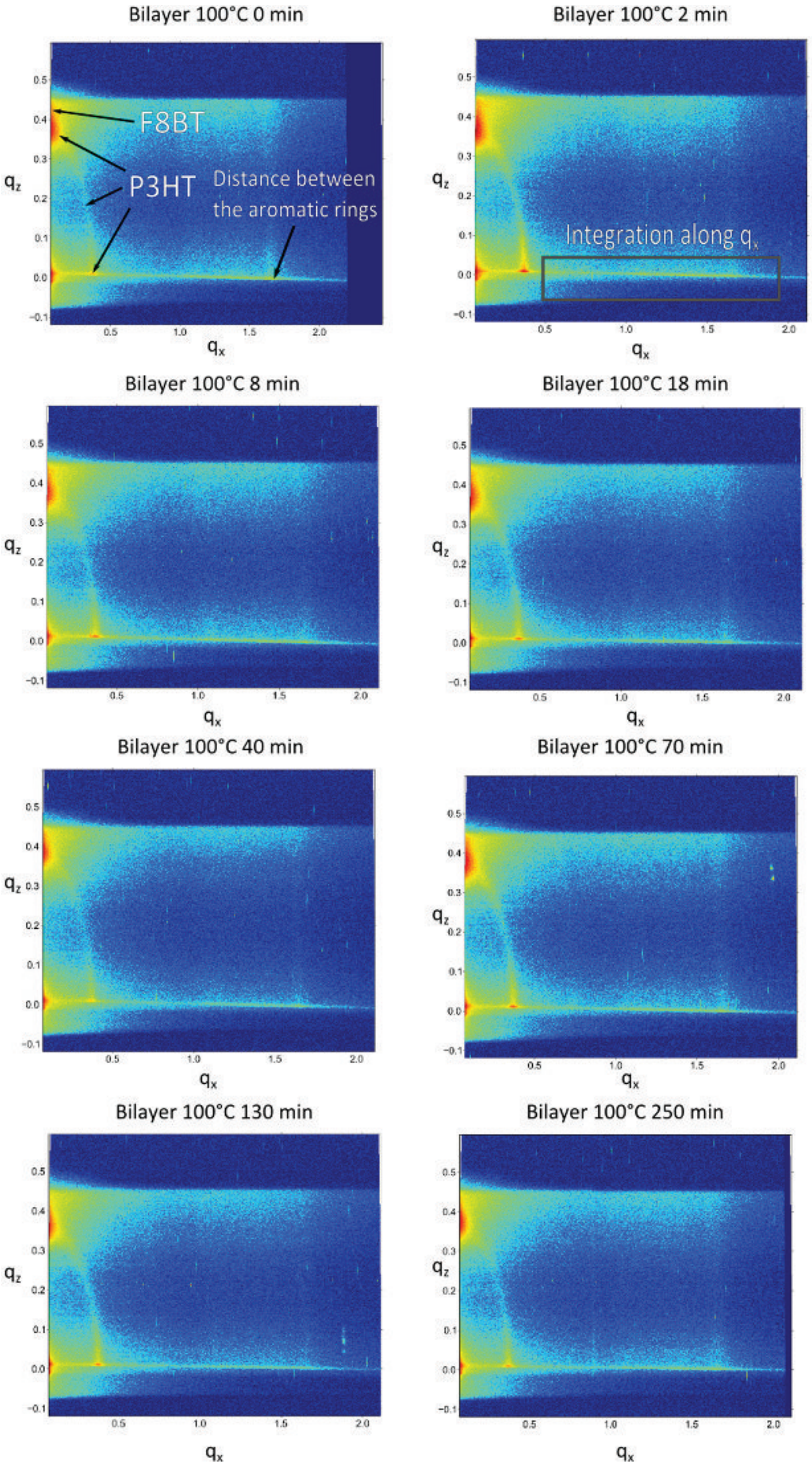

Figure 3.24: Reciprocal space maps of the J-PARC bilayer-samples prepared on native silicon.

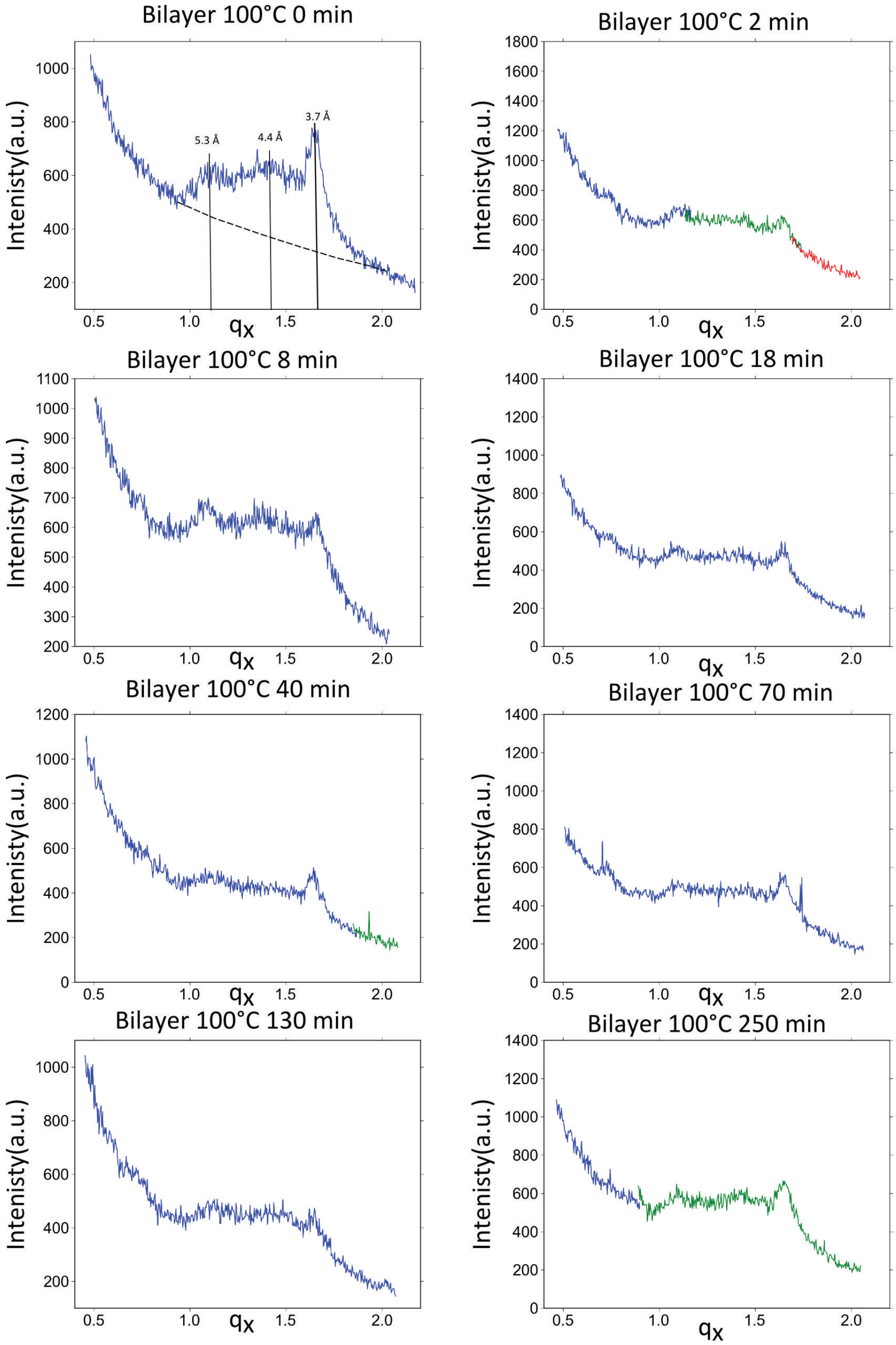

Figure 3.25: Integration of grazing incident X-ray diffraction path along the Yoneda-peak over $q_x$.

## 3.6 Photovoltaic-Measurements

The commonly accepted model of OSC says that the phase interface area is very important for the efficiency of the cell. If the interface roughness rises, it would also mean that the interface area increases and therefore an increase in efficiency should be observed. The goal of the photovoltaic measurements was to find any correlation of efficiency and roughness.

### 3.6.1 Photovoltaic Measurements for $90°C$

The Fig. 3.26 illustrates a typical photovoltaic-curve of two device for different annealing times. The not annealed curve is quiet flat and have a very low fill factor. For some devices a change of shape of the photovoltaic-curve through temperature treatment was observed. The photovoltaic curve change from concave at low internal field to convex at higher internal fields, which lead to a increase of photocurrent until $I_{SC}$, Fig. 3.26 a).
The others had also an increase in photocurrent, but their shape was more less conserved over the whole experiment, Fig. 3.26 b). Generally the current from the solar cell became higher for every part of the active regime, this was observed for all devices.
The fill factor was in average about $FF = 0.15\%$. The efficiency rised for nearly all devices until an annealing time of about 40 $min$. For longer annealing times the photocurrent drops again, but the shape of the curve was conserved.
In Fig. 3.26 a), the inflection point is marked for a typical device, were annealing led to a high increase of photocurrent. For devices like in Fig. 3.26 b) the photovoltaic-curve stay concave, but the inclination becomes higher. Additionally the curve is shifted parallel to higher photocurrents. Both effects increased the $I_{SC}$.

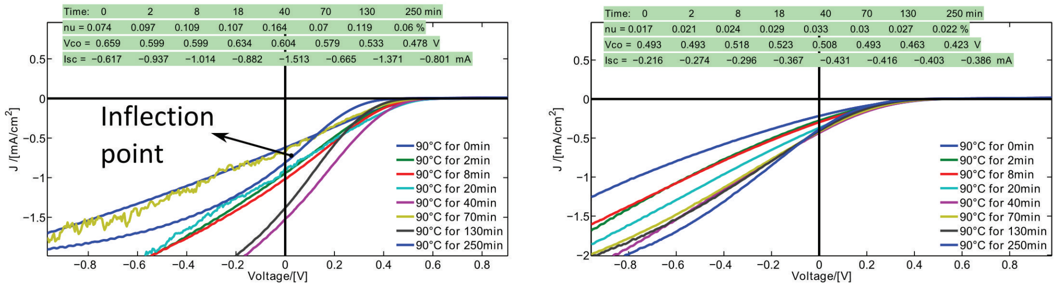

a) b)

Figure 3.26: Typical photovoltaic-curves for the $90°C$ series. $I_{SC}$ is the short circuit current, $V_{OC}$ is the open circuit voltage and $nu$ is the power conversion efficiency($PCE$).

To get a better overview, the change of $I_{SC}$, $V_{OC}$ and $PCE$ was averaged for all time steps and 12 devices to see the development of those parameters. For this the $I_{SC}$, $V_{OC}$

and $PCE$ of the annealed device was divided by the $I_{SC}$, $V_{OC}$ and $PCE$ of the not annealed one and the change is depicted percental.

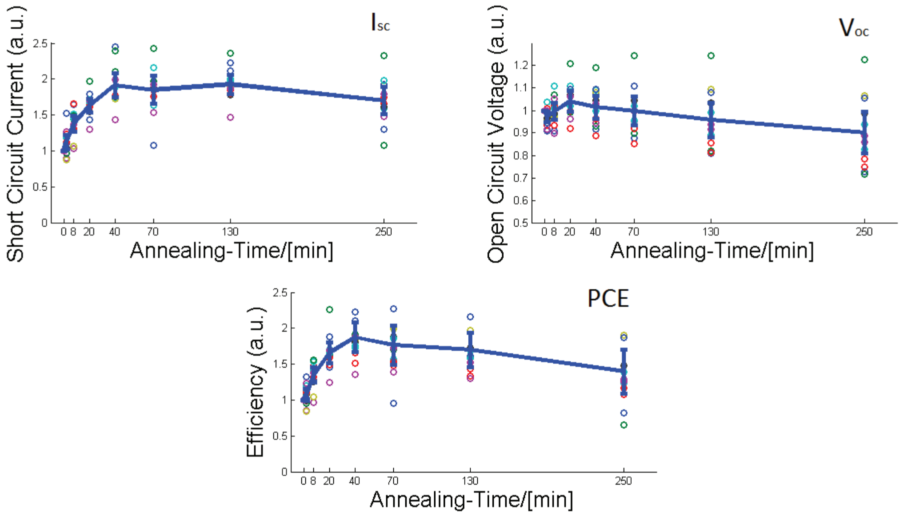

Figure 3.27: To compare the results of all devices at 90°$C$ the parameters $I_{SC}$, $V_{OC}$ and $PCE$ were divided by the initial values of the not annealed ones. Here just the relative change of those parameters is depicted.

Fig. 3.27 shows an increase of $I_{SC}$ until 40 $min$ then the current decays slowly again, but for 250 $min$ is still higher than the $I_{SC}$ of the not annealed devices. The $V_{OC}$ rises for short times, but decaying constantly after 20 $min$ to a value which is below the not annealed device. The change of the $V_{OC}$ is far less than for the $I_{SC}$, therefore the $PCE$ is highly influenced by the increase of photocurrent and has its maximum also at 40 $min$. After the whole annealing period the $PCE$ is mostly still higher than it was for the pristine devices.

The fill factor decreased generally with increasing $PCE$, which is caused by the shape of photovoltaic-curve.

### 3.6.2 Photovoltaic Measurements for 100°$C$

This photovoltaic-series showed a similar behaviour like the 90°$C$ series, but effects were weaker. The reason is maybe a in average weaker efficiency than in the 90°$C$ series, but for 80% of devices a change of shape from the photovoltaic-curve was observed. Fig. 3.28 left, shows the strongest effects, but almost all curves looked like Fig. 3.28 right. Also here the not annealed devices have a bad fill factor and with annealing the photocurrent increases and therefore the $I_{SC}$.

The photovoltaic curve with annealing is near the $V_{OC}$ concave and turns in a convex curve in the middle of the active regime and the photocurrent increases until $I_{SC}$. That is a hint for a better charge collection and separation at higher internal electric field in the OSC.

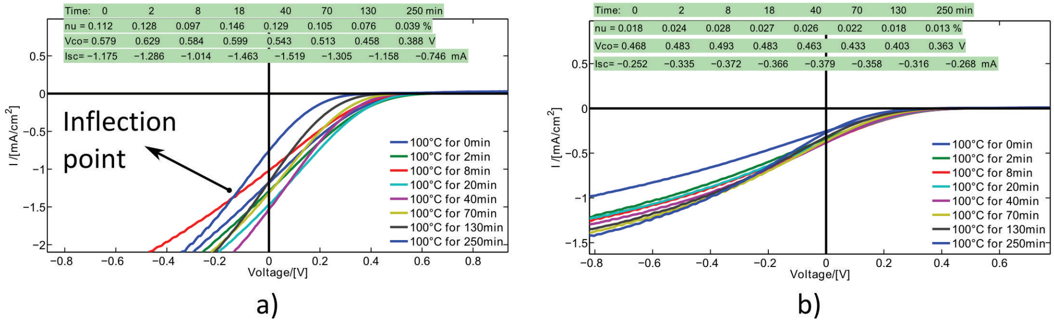

Figure 3.28: Typical photovoltaic-curve for the 100°$C$ series. The inflexion point is marked. $I_{SC}$ is the short circuit current, $V_{OC}$ is the open circuit voltage and $nu$ is the power conversion efficiency($PCE$).

A summery of results for the 100°$C$ is given in Fig. 3.29. As well as for the 90°$C$-series the 100°$C$-series displays an increase in the $I_{SC}$ is less and shifted a bit to shorter time steps around 40 $min$. $I_{SC}$ decays more rapid and reaches for 250 $min$ the $I_{SC}$ of the not annealed samples. The $V_{OC}$ decreases faster too.
The $PCE$ is again connected with increase of photocurrent and has its maximum at the same time were the photocurrent has its peak. After 250 $min$ of annealing the $PCE$ dropped below the not annealed devices, which can be connected to the high decrease of $V_{OC}$ for longer times.

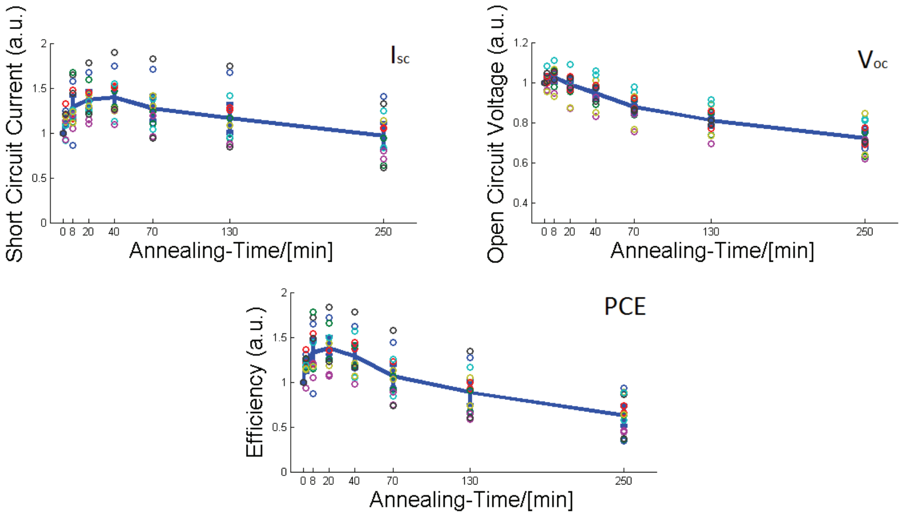

Figure 3.29: To compare the results of all devices at 100°$C$ the parameters $I_{SC}$, $V_{OC}$ and $PCE$ were divided by the initial values of the not annealed ones. Here just the relative change of those parameters is depicted.

### 3.6.3 Photovoltaic Measurements for $110°C$

The influence on the photovoltaic-curve was the strongest for the $110°C$-series. Interesting is the shape of the curve not changes from concave to convex in the active regime any more for most of the 18 devices. The inflection point is shifted into the reveres bias regime for further annealing Fig. 3.30.

The fill factor is still bad and has a average of about 15%. Photocurrent improves after the first heat treatment, also for a low internal field in the active layer, but for longer annealing times the internal field have to be stronger to perform the same photocurrent as the pristine OSC.

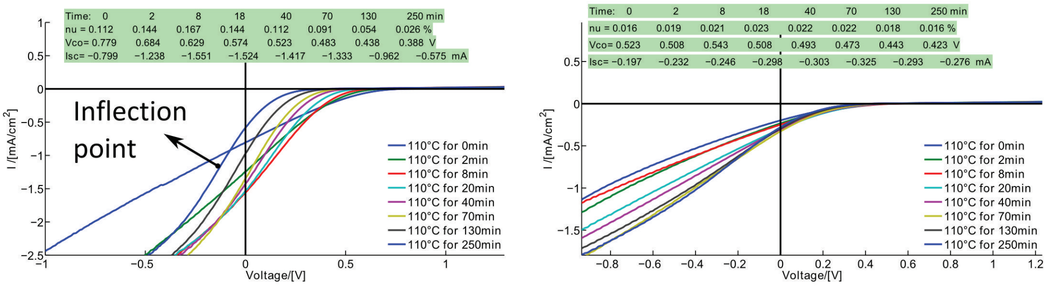

a) b)

Figure 3.30: Typical OPV-curve for the $110°C$ series. The inflexion point is marked. $I_{SC}$ is the short circuit current, $V_{OC}$ is the open circuit voltage and $nu$ is the power conversion efficiency($PCE$).

At $110°C$ the maximum peak of the $I_{SC}$ is shifted to shorter annealing times around 8 $min$. For 250 $min$ the $I_{SC}$ is still higher than the initial ones. That is a bit in controversy to the $100°C$-series, but for $100°C$ also the improve of $I_{SC}$ was lower, see Fig. 3.29. The decay of $V_{OC}$ goes down to 60% from the pristine devices and has so the strongest decay for all temperatures. Increase in $PCE$ is again proportional to $I_{SC}$ and has its maximum at 8 $min$, followed by a constant decrease, which is connected to $V_{OC}$ and the reduction of the $I_{SC}$.

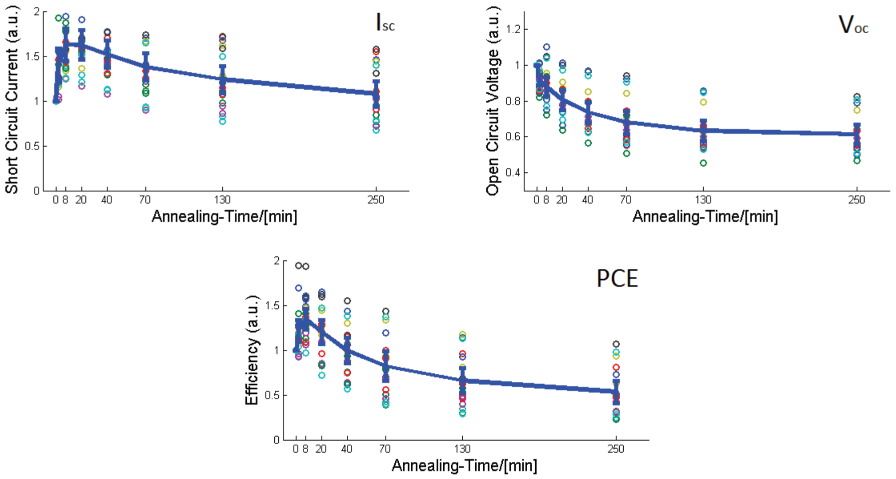

Figure 3.31: To compare the results of all devices at 110°$C$ the parameters $I_{SC}$, $V_{OC}$ and $PCE$ were divided by the initial values of the not annealed ones. Here just the relative change of those parameters is depicted.

To get a better overview of the reults from the photovoltaic measurements for three temperatures the efficiencies are depicted togehter in Fig. 3.32. It is clearly to see that the maximum of the efficiency shifts to shorter times with higher temperatures and also the decay is enhanced.

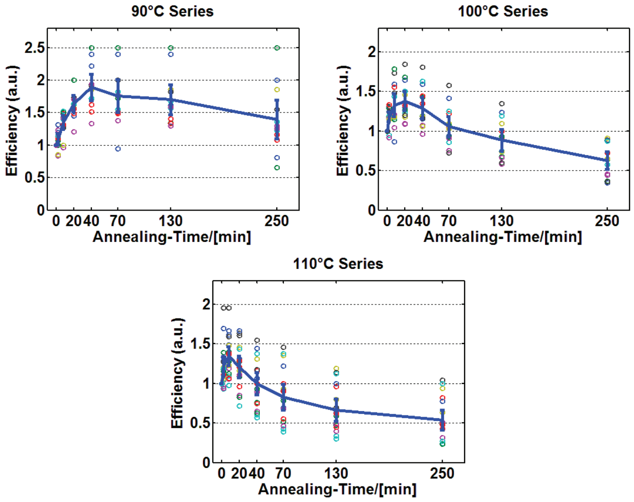

Figure 3.32: Efficiency of the 90°$C$-, 100°$C$- and 110°$C$- series is depicted.

## 3.7 Conclusion

### X-ray Reflectivity Measurements

The analysis of the bilayer samples with XRR on native silicon shows two different oscillations of fringes. This is correlated to a similar electron density of P3HT and F8BT. For the first part of the XRR-scan the X-ray can not separate the P3HT and F8BT, therefore the fringes are connected to the thickess of both layers. At incident angles of $\alpha_i \geq 1.5°$ the oscillations changes and fringes appear, which come form the P3HT.
Annealing experiments reveal a decrease of those P3HT-fringes, despite the applied temperatures are below the glass transition temperature of the polymers. The decay of the fringes is proportional to the applied temperature and annealing time. Further simulations suggest that the decrease depends on the interface roughness, which is in the order of a few nanometers.

### Neutron Reflectivity

The data of the singles layer are in accordance with the X-ray reflectivity, however the neutron reflectivity curve of the bilayer are contratictory. A too high surface roughness reduces the sensiblity for the interface, maybe therefore the neutron reflectivity depicts a nearly constant interface roughness. Those results of the neutron data must be consequently questioned.

### Gracing Incident X-ray Diffraction Measurements

The GIXD measurement showed clearly that the crystallinity of the both polymers dont't become higher with a temperature treatment at $100°C$. This result was expected because the glass tranistion temperature of the polymers is about $130°C$.

### Increase of Efficiency

The conclusion out of the measurement data and literature is, that the structural changes of P3HT lead to a higher charge mobility, which improves the exciton separation at the polymer interface. This enhancement results in a higher photocurrent and efficiency. The argumentation for a higher charge mobility in the P3HT is the following:

- According to [30], [31] the $\mu_h$ of P3HT becomes better with annealing, but the changes are very modest(less than a magnitude), see Sec. 1.4.2.
- The higher photocurrents for low internal fields of the annealed samples are a hint for a better mobility and charge separation at the interface. An efficient charge separation not only depends on a smooth interface, but also on a high mobility to reduce geminate recombination, [59].

- A improvement of the PLQE with temperature treatment can not be totally exclueded, but if the generation of excitons become better with annealing the photovoltaic-curve should maintain more less is original shape and the photocurrent should shift parallel to the initial photovoltaic-curve, can be seen in, [43]. Also the PLQE of P3HT not changes strongly at such temperatures. Therefore the effects of PLQE are regarded as minimal.
- The charge mobility of F8BT decreases through thermal treatment according to the literature, [36]. In [59] also bilayer solar cells were built with floated F8BT on top of PFB(poly(9,9'-dioctylfluorene-co-bis(N,N'-(4,butylphenyl))bis(N,N'-phenyl-1,4-phenylene)diamine)). There the annealing led to a constant decrease of the performance. The results from [36] and [59] lead to the conclusion that the F8BT is definitly not able to improve the efficiency by $40 - 100\%$.

### Decrease of Efficiency

The photovoltaic and X-ray reflectivity measurements displayed that the decrease of the efficiency is connected with the decay of the P3HT-fringes and therefore with the interfacial roughness. Due to a rough interface the charge separation probability decreases of the electron-holes pair, [59].
As evidence the $90°C$ is a good example. Here the fringes hardly change for the whole period, see Fig. 3.13. A similar behaviour could be also seen for the photovoltaic measurements at $90°C$. The $I_{SC}$ and the efficiency stays after the improvement nearly constant, see Fig. 3.27.
For the $100°C$ and $110°C$-series the decrease of the fringes and efficiency become stronger.

### Correlation between Efficiency and Interface Rouhness

At short annealing times the enhancement of the charge mobility through the structural changes of P3HT are dominat compared to the permanent decrease of the exciton separation due to higher roughness. For longer annealing times the structural ordering comes to its limits and the still growing interface roughness leads then to the decay of efficiency, which was observed for all temperatures.
The result suggests that a smooth interface provids an effective charge separation, in contrast rougher interfaces have a higher disorder, which may leds to a decrease of performance, [59].

# 4 Appendix

## 4.1 Setup of the PANalytical EMPYREAN

The standard setup for X-ray reflectivity was:

- Incident Side:
  - Multilayer Mirror
  - Mask 10 $mm$
  - Beam Attenuator
- Diffracted Side:
  - Divergence Slit: 0.1 $mm$
  - Soller Slit: 2°
- Used was $Cu_{K_\alpha}$-radiation
- X-ray tube was at 40 $mA$ and 40 $kV$
- Detector: 0D receiving slit mode 3 channels open

## 4.2 X-ray Reflectivity-Fit of F8BT single layer

Without the AFM measurement for a cross check, it would be harder to get reliable values out of the XRR-fit. In Fig. 4.1 the interface roughness and surface roughness of Fig. 3.6 are switched. Fig. 4.1 is a good example of the problem by applying the same model for roughness and electron densities. Both models are in competition with each other. Here the surface roughness is higher, but as a consequence the electron density is lower as in Fig. 3.6.
Of course the fit is not perfectly fitting in the low $q$-region, which is a hint for a mistake in the surface roughness, but still the cross check with the AFM was helpful to get good data.

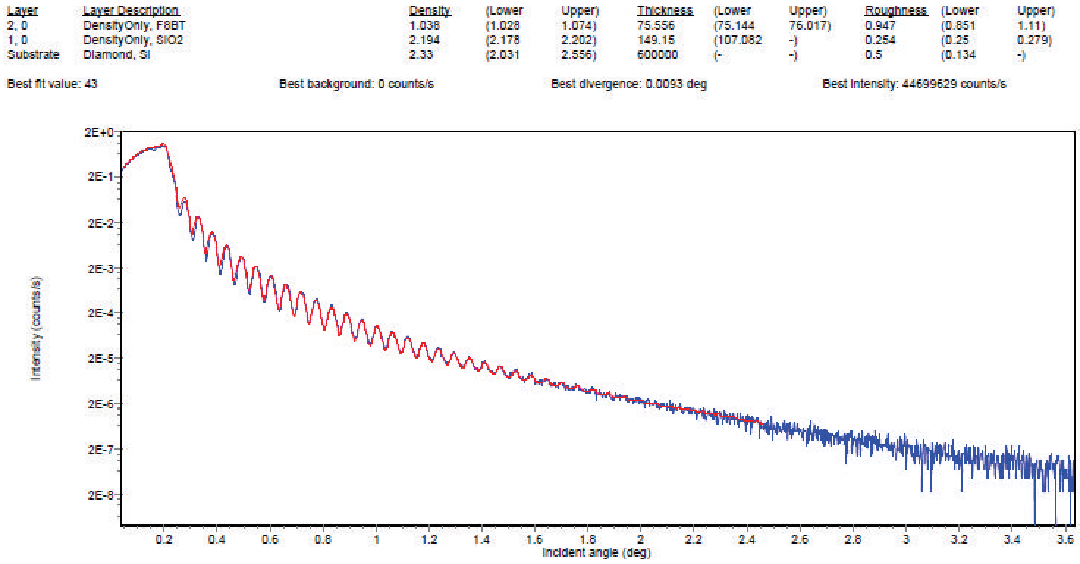

| Layer | Layer Description | Density | (Lower | Upper) | Thickness | (Lower | Upper) | Roughness | (Lower | Upper) |
|---|---|---|---|---|---|---|---|---|---|---|
| 2, 0 | DensityOnly, F8BT | 1.038 | (1.028 | 1.074) | 75.556 | (75.144 | 76.017) | 0.947 | (0.851 | 1.11) |
| 1, 0 | DensityOnly, SIO2 | 2.194 | (2.178 | 2.202) | 149.15 | (107.082 | -) | 0.254 | (0.25 | 0.279) |
| Substrate | Diamond, Si | 2.33 | (2.031 | 2.556) | 600000 | (- | -) | 0.5 | (0.134 | -) |

Best fit value: 43 Best background: 0 counts/s Best divergence: 0.0093 deg Best intensity: 44699629 counts/s

Figure 4.1: Fit of F8BT-single layer on top n-$Si$. Here interface roughness and surface roughness are switched. Mind the lower electron density of F8BT.

## 4.3 Water at the Interface

The standard $Si$-substrates($20\ mm \times 20\ mm$) are better to float than bigger ones. Especially the substrates for the J-PARC samples had a lot of water residuals in the interface directly after floating. Fig. 4.2 is a photo series over 1.5 $h$ and displays the evaporation from the distilled water through the F8BT. This documentation shows just that big amounts of water can easily evaporate through the F8BT layer. Of cause monolayers of water will still be sticing at the interface of the polymers.

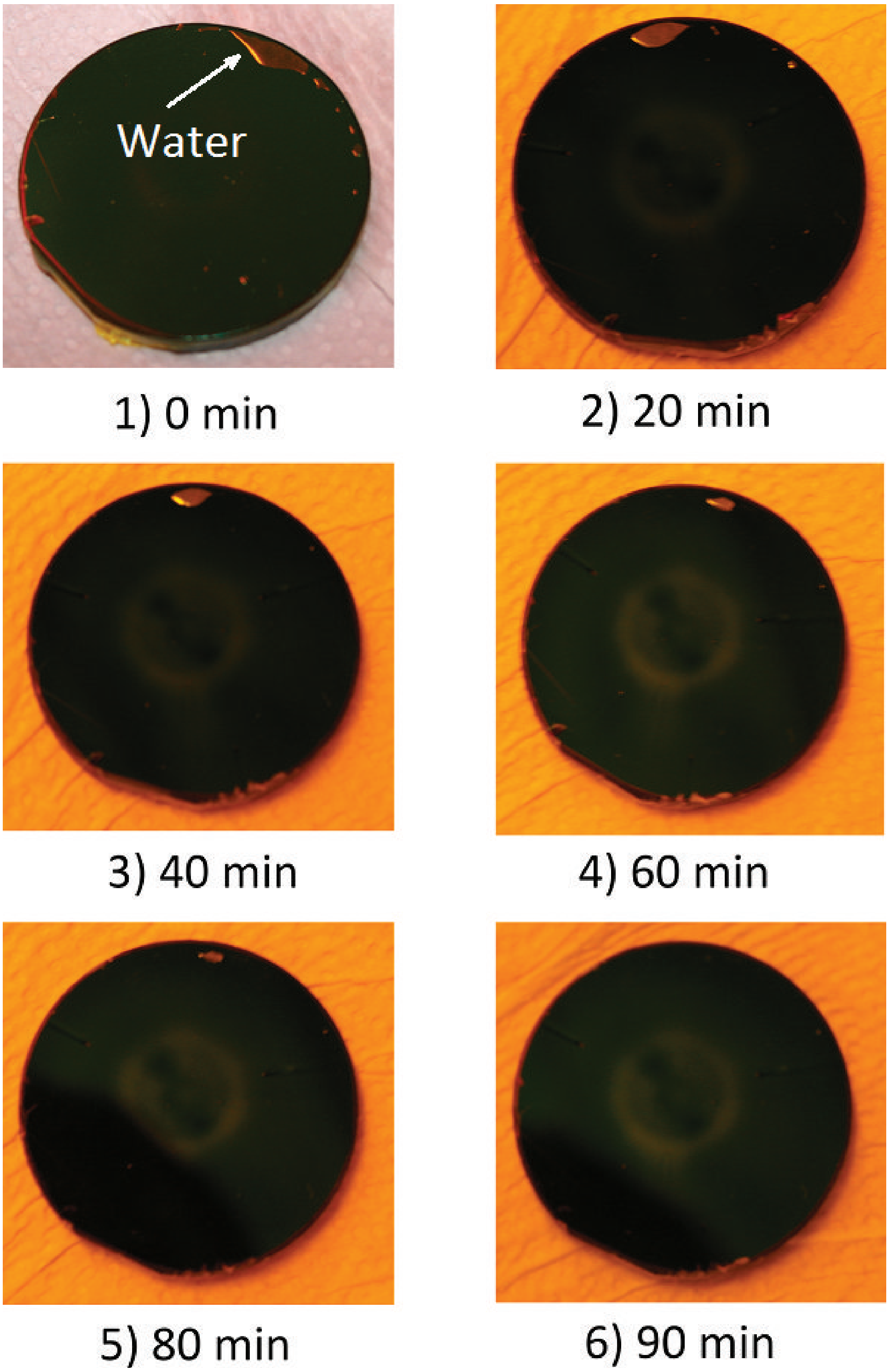

1) 0 min

2) 20 min

3) 40 min

4) 60 min

5) 80 min

6) 90 min

Figure 4.2: Evaporation of water from the interface through the top layer in 1.5 *h*.

## 4.4 Mask

To evaporate more ITO samples at once a new mask was need. The drafts are given in the following figures.

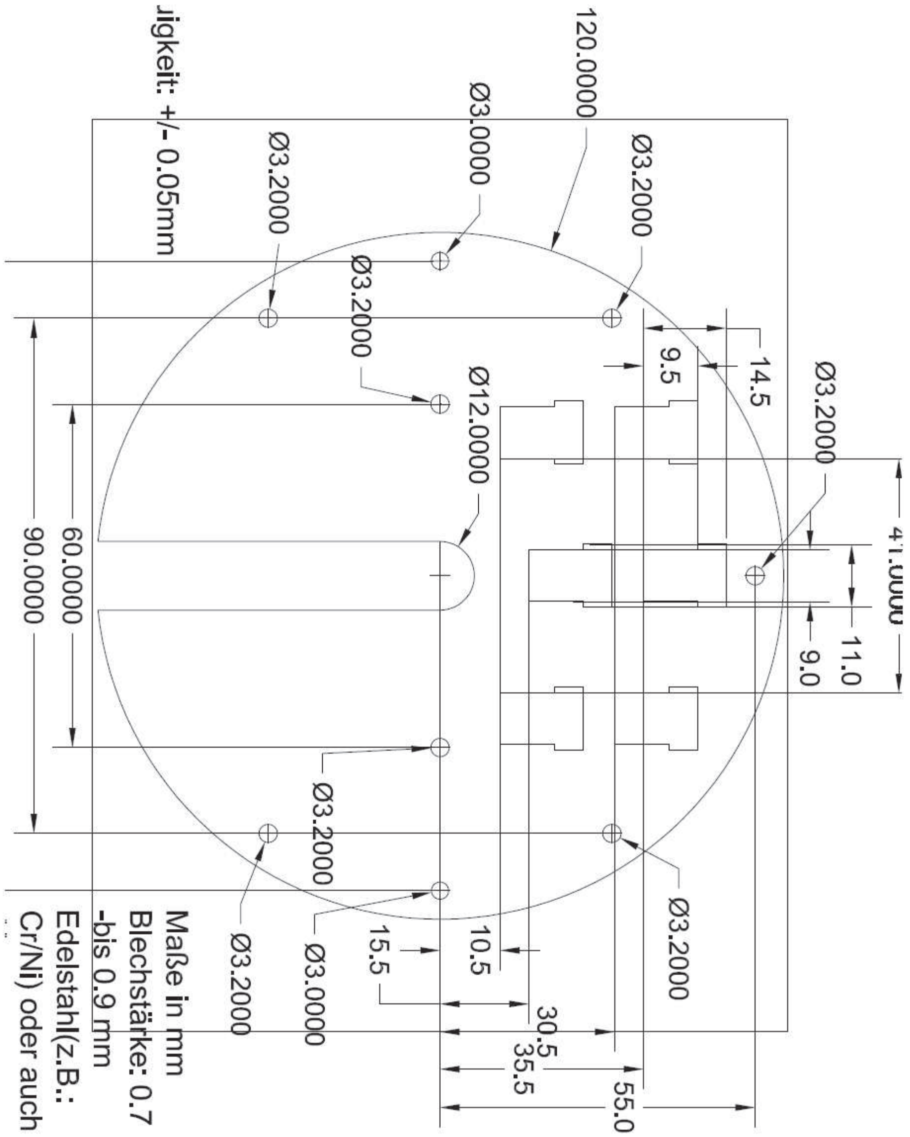

Figure 4.3: Cathode side of the mask. Six patterns are cut with high accuracy into high quality steel.

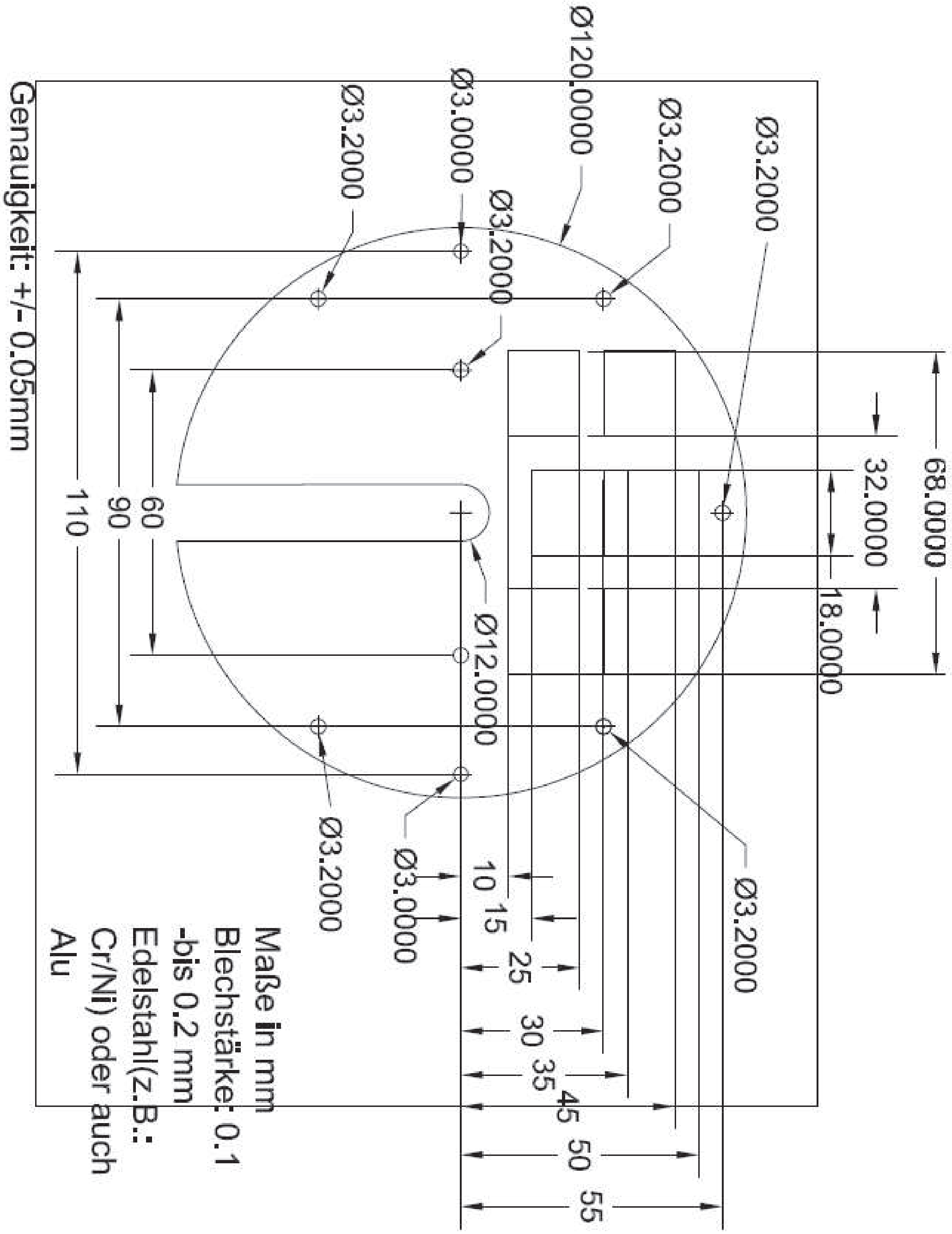

Figure 4.4: Distance plate between cathode side and the plate which fixes the ITOs. This plate protects the ITOs and make the handling a bit easier.

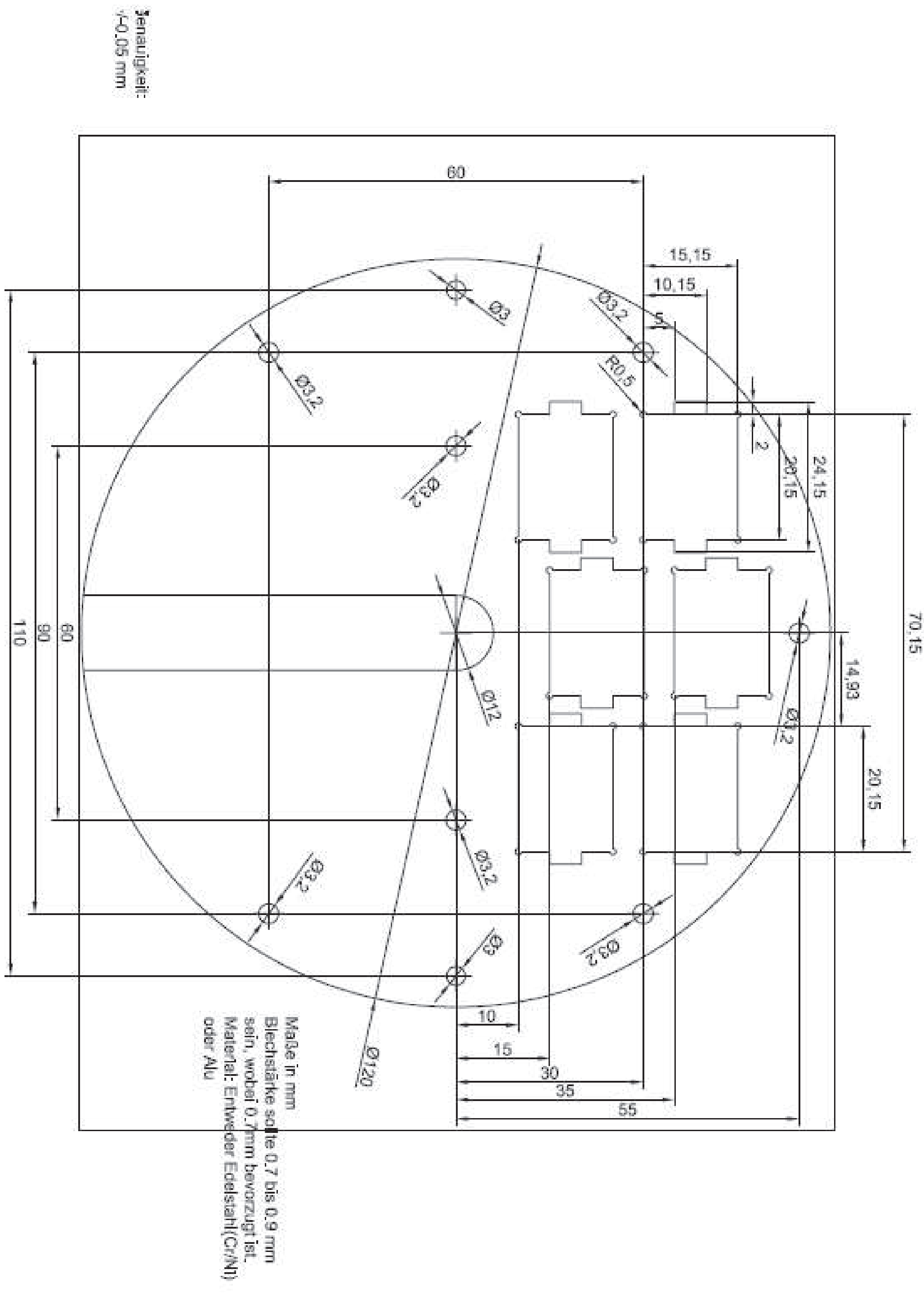

Genauigkeit:
+/-0.05 mm

Maße in mm
Blechstärke sollte 0.7 bis 0.9 mm
sein, wobei 0.7mm bevorzugt ist.
Material: Entweder Edelstahl(Cr/Ni)
oder Alu

Figure 4.5: Here the recess for the ITOs is cut.

## 4.5 X-ray Reflectivity on Indium Tin Oxid

ITO was far to rough to exime it with the XRR. A look upon Fig. 4.6 shows that the XRR-curve has a low reflectivity for small angles. The ITO layer here is about 120 $nm$, which are the first fringes. The bigger ones come from a protactive layer of $SiO_2$. It should prevent the sodium from the diffusing into the ITO.

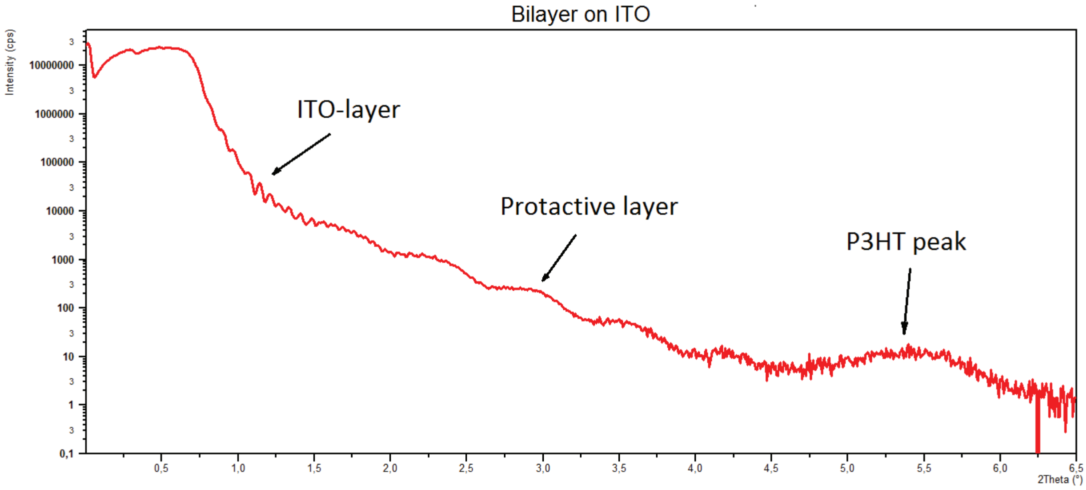

Figure 4.6: XRR of a polmer bilayer on ITO. It was impossilbe to identify the polymers on the ITO.

## 4.6 Organic Solar Cells - Dark Current

Normally the OSC should show a diode behaviour for voltages like $V > V_{OC}$. Charge injection takes place similar to an inorganic diode, but the bilayer OSC showed, compared to other OSC, a strange dark current, Fig. 4.7. Just after applying high voltages the diod current begins to increase. The applied voltages are four to five times higher than the $V_{OC}$ of OSC itself. The real reason was not discovered until now. I don't think it is a lack of contact at the bilayer, because then OSC should not work as it does.

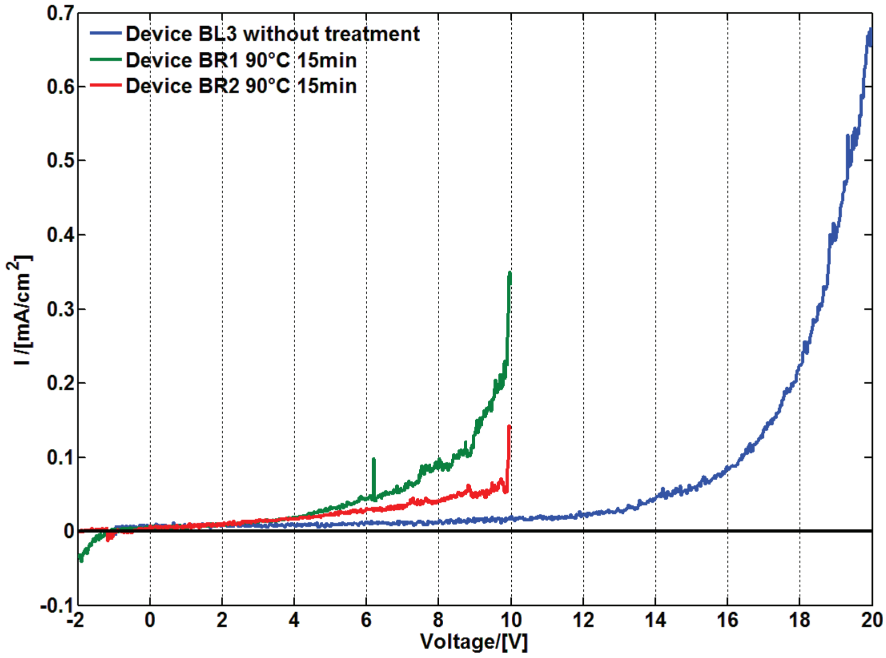

Figure 4.7: Diod current of some OSC. With annealing the dark current increases at lower voltages.

# Bibliography

[1] H. Kiessig, *Interferenzen von Röntgenstrahlen an dünnen Schichten*, Annalen der Physik, Volume 402, Issue 7, pages 769Ű788, 1931

[2] J.A.Nielson and D.McMorrow, *Elements of Modern X-Ray Physics*, John Willey and Sons, LTD, 2001

[3] M.Tolan, *X-Ray Scattering from Soft-Matter Thin Films*, Springer-Verlag Berlin Heidelberg,1999

[4] M.Birkholz, *Thin Film Analysis by X-Ray Scattering*, WILEY-VCH Verlag GmbH and Co, 2006

[5] T.Neger, *Optik*, LV Nr.511.131, SS 2010, unpublished

[6] R.Resel, *Röntgendiffraktometrie*, LV Nr. 512.142 SS 2013

[7] A.Pichler, *Crystal Structure Resolution of Organic Thin Films*, Master Thesis, TU Graz 2013

[8] P.Linder ,Th.Zemb, *Neutrons, X-Rays and Light: Scattering Methods Applied to Soft Condensed Matter*, North-Holland, ELSEVIER 2002

[9] J.Daillant, A. Gibaud, *X-Ray and Neutron Reflectivity*, Springer-Verlag Berlin Heidelberg, 2009

[10] Wikipedia, *Neutron Source*, *http : //en.wikipedia.org/wiki/Neutron*$_s$*ource*, Online: accessed in August 2013

[11] Institute of Electrical and Electronics Engineers, *SYNCHROTRON RADIATION IN 2003*, *http : //www.ieee.org/organizations/pubs/newsletters/npss/*0304*/sync.html*, Online: accessed in September 2013

[12] Veqter, *Residual Stress Experts*, *http : //www.veqter.co.uk/residual − stress − measurement/neutron − diffraction*, Online: accessed in July 2013

[13] TU München, *Forschungs-Neutronenquelle, Heinz-Maier-Leibnitz (FRM-II)*, *http : //www.frm2.tum.de/technik/reaktor/index.html*, Online: accessed in July 2013

[14] Heinz-Maier-Leibnitz Zentrum, *Neutronen für Forschung, Industrie and Medizin*, *http : //www.mlz − garching.de/neutronenforschung/neutronenquelle.html*, Online: accessed in August 2013

[15] Wikipedia, *Spallation*, $http://en.wikipedia.org/wiki/Spallation$, Online: accessed in August 2013

[16] J-PARC, beamline: SOFIA, *Specifications of neutron instruments*, $http://j-parc.jp/researcher/MatLife/en/instrumentation/ns_spec.htmlbl16$, Online: accessed in August 2013

[17] G.Krexner, *Inelastic Neutron Scattering*, NESY Winterschool, Palnneralm 2013

[18] Wikipedia, *Conductive Polymer*, $http://en.wikipedia.org/wiki/Conductive_polymer$, Online: accessed in August 2013

[19] Wikipedia, *Conjugated system*, $http://en.wikipedia.org/wiki/Conjugated_system$, Online: accessed in August 2013

[20] Wikipedia, *Polypropylene*, $http://commons.wikimedia.org/wiki/File:Polypropylene.svg$, Online: accessed in August 2013

[21] B.Friedel, Ch.R.McNeill and N.C.Greenham, *Influence of Alkyl Side-Chain Length on the Performance of Poly(3-alkylthiophene)/Polyfluorene All-Polymer Solar Cells*, Chem. Mater.2010,20,3389-3398

[22] H.D.R.Calado, T.Malencio, C.L.Donnici, C.A.Cury, J.Rieumoni, J.R.Pernaut,*Synthesis and electrochemical and optical characterization of poly(3-octadecylthiophene)*, ELSERVIER,Volume 158, Issues 21Ű24, December 2008, Pages 1037Ű1042

[23] D.Fichou, *Handbook of Oligo- and Polyythiophenes*, WILEY-VCH Verlag GmbH and Co, 1999

[24] J.U.Wallace, *Carrier Mobility in Organic Charge Transport Materials:Methods of Measurement, Analysis, and Modulation*, Phd. Thesis, University of Rochester, 2009

[25] R.A.L.Jones, *Soft Condensed Matter*, Oxford Univeristy Press, 2011

[26] W. Li and AJ Ryan, *Phase Transitions in Soft Matter*, $http://www.helsinki.fi/\ serimaa/soft-luento/soft-2-phase.html$, Online: accessed in August 2013

[27] Wikipedia, *Differential Scaning Calormetry*, $http://en.wikipedia.org/wiki/File:Inside_DSC_small.jpg$, 14.08.2013, Online: accessed in August 2013

[28] P.G.Nicholson, V.Ruiz, J.V.Macphersona and P.R.U, *Effect of composition on the conductivity and morphology of poly(3-hexylthiophene)/gold nanoparticle composite LangmuirŰSchaeffer films*, Phys. Chem. Chem. Phys., 2006,8, 5096-5105

[29] Wikipedia, *Poly(3-hexylthiophen-2,5-diyl)-(P3HT)*, $http://de.wikipedia.org/wiki/Poly(3-hexylthiophen-2,5-diyl)$, Online: accessed in August

[30] A.M.Ballantyne1, L. Chen, J. Dane, T. Hammant, F.M. Braun, M. Heeney, W. Duffy, I. McCulloch, D.D.C. Bradley, J. Nelson, *The Effect of Poly(3-hexylthiophene) Molecular Weight on Charge Transport and the Performance of Polymer:Fullerene Solar Cells*, Adv. Funct.Mater. 2008 18, 2373-2380

[31] H.G. Flesch, R. Resel and C.R. McNeill, *Charge transport properties and microstructure of polythiophene/polyfluorene blends*, Organic Electronics 10(8): 1549-1555

[32] W. Bagienski, M.C. Gupta, *Temperature dependence of polymer/fullerene organic solar cells*, ELSEVIER 95(2011) 933-941

[33] T.T. Ngo, D.N. Nguyen, Van T. Nguyen, *Glass transition of PCBM, P3HT and their blends in quenched state*, Adv. Nat. Sci.: Nanosci. Nanotechnol. 3 (2012) 045001

[34] Y. Zhao, G. Yuan, P. Roche, *A calorimetric study of the phase transitions in poly(3-hexylthiophene)*, Polymer Vol. 36 Nr.11,1995

[35] G.C. Faria, H.V. Seggern, R.M. Faria, E.R. deAzevedo, *Influence of molecular dynamics on the dielectric properties of poly(9,9-di-n-octylfluorene-altbenzothiadiazole) -based devices*, Dielectrics and Electrical Insulation, IEEE, (2012) August,1181 - 1185

[36] C.L. Donley, J. Zaumseil, J.W. Andreasen ,M.M. Nielsen, H. Sirringhaus, R.H. Friend, Ji-S. Kim, *Effects of Packing Structure on the Optoelectronic and Charge Transport Properties in Poly(9,9-di-n-octylfluorene-alt-benzothiadiazole)*, J. Am. Chem. Soc. 2005,127,12890-1289

[37] Ch.R. McNeill1, A. Abrusci, I. Hwang, M.A. Ruderer, P. Müller-Buschbaum, N.C. Greenham, *Photophysics and Photocurrent Generation in Polythiophene/Polyfluorene Copolymer Blends*, Adv.Funct.Mater. 2009,19,3103-3111

[38] M.J. Banach, R.H. Friend, H. Sirringhaus, *Influence of the Molecular Weight on the Thermotropic Alignment of Thin Liquid Crystalline Polyfluorene Copolymer Films*, Macromolecules 2003,36, 2838-2844

[39] T. Kietzke, *Recent Advances in Organic Solar Cells*, Advances in OptoElectronics Volume 2007 (2007), Article ID 40285, 15 pages

[40] H. Hoppe, N. S. Sariciftci, *Polymer Solar Cells.* Photoresponsive Polymers II. (2008) 1Ű86

[41] S. Günes, H. Neugebauer, N.S. Sariciftci, *Conjugated Polymer-Based Organic Solar Cells*, Chem. Rev. 2007,107, 1324-1338

[42] D. Woehrle, D. Meissner, *Organic Soalr Cells*, Adv.Material. 3(1991) No.3

[43] T. Erb, U. Zhokhavets, G. Gobsch, S. Raleva, B. Stühn, P. Schilinsky, C. Waldauf, C.J. Brabec, *Correlation Between Structural and Optical Properties of Composite Polymer/Fullerene Films for Organic Solar Cells*, Adv.Mater. 2005,15,1193-1196

[44] Y.o Kim, D.D.C. Bradley, *Bright red emission from single layer polymer light-emitting devices based on blends of regioregular P3HT and F8BT*, Current Applied Physics 5(2005) 222-226

[45] W.C.H. Choy, *Organic Solar Cells*, Springer Verlag London, Heidelberg, New York, Dordrecht, 2013

[46] K. Taylor, *Tandem Polymer Solar Cell set Energy Conversion Record*, $http://www.tgdaily.com/sustainability-features/61433-tandem-polymer-solar-cells-set-energy-conversion-record$, Online: accessed in August 2013

[47] Heliathek, *Neuer Weltrekord für organische Solarzellen: Heliatek behauptet sich mit 12 % Zelleffizienz als Technologieführer*, $http://www.heliatek.com/newscenter/latest_news/neuer-weltrekord-fur-organische-solarzellen-heliatek-behauptet-sich-mit-12-zelleffizienz-als-technologiefuhrer/$, Online accessed in August 2013

[48] H. Ma, H.L. Yip, F. Huang, A.K.Y. Jen, *Interface Engineering for Organic Electronic*, Adv.Funct.Mater.2010,20,1371-1388

[49] Wikipedia, *Photovoltaic system*, $http://en.wikipedia.org/wiki/Photovoltaic_system$, Online: accessed in August 2013

[50] M. Jørgensen, K. Norrman, F.C. Krebs, *Stability/degradation of polymer solar cells*, ELSEVIER, Volume 92, Issue 7, July 2008, Pages 686Ũ714

[51] Y. Zhang, P.W.M. Blom, *Electron and hole transport in poly(fluorene-benzothiadiazole)*, Applied Physics Letters 98,143504(2011)

[52] A.M. Ballantyne, L. Chen, J. Dane, T. Hammant, F.M. Braun, M. Heeney, W. Duffy, I. McCulloch, D.D.C. Bradley, J. Nelson, *The Effect of Poly(3-hexylthiophene) Molecular Weight on Charge Transport and the Performance of Polymer:Fullerene Solar Cells*, Polymers Chemistry and Physics of Modern Materials, 2nd. Ed., Blackie Academic and Professional, Glasgow, 1991

[53] F. Padinger, R.S. Ritterberg, N.S. Sariciftci, *Effects of Postproduction Treamtent on Plastic Soalr Cells*, Adv. Funct. Mater. 2003,13,Nr.1,Jan

[54] R. Schlafa, H. Muratab, Z.H. Kafafib, *Work function measurements on indium tin oxide films*, ELSEVIER, Journal of Electron Spectroscopy and Related Phenomena 120 (2001) 149Ũ154

[55] M. Chelvayohan, C. H B. Mee, *Work function measurements on (110), (100) and (111) surfaces of silver*, 1982 J. Phys. C: Solid State Phys. 15 2305

[56] Ossila, *S101 Pixelated Anode Substrates for OPV/OLED Testing*, $http://www.ossila.com/oled_opv_ofet_catalogue3/OLED_OPV_Substrates/S101-pre-patterned_ITO_glass_substrates.php$, Online: accessed in August 2013

[57] The Center for X-Ray Optics, *Index of Refraction* ,$http : //henke.lbl.gov/optical_constants/getdb2.html$, Online: accessed in August 2013

[58] google app engine, *Scattering Length Density Calculator*, $http : //sld - calculator.appspot.com/$, Online: accessed in August 2013

[59] H. Yan, S.l Swaraj, Ch. Wang, I. Hwang, N.C. Greenham1, Ch.Groves, H. Ade, Ch.R. McNeill, *Influence of Annealing and Interfacial Roughness on the Performance of Bilayer Donor/Acceptor Polymer Photovoltaic Devices*, Adv. Funtc. Mate. 2010,20,4329-4337

[60] L. He, Z. Wu, Z. Li, J. Ju, Q. Ou and R. Liang, *Surface work function of indium tin oxide treated using plasma immersion ion implantation*, Journal of Physics D: Applied Physics, 46(2013) 175306

[61] Y. Li, J. B. Lagowski, *A multi-step simulation of electron mobility in fluorene-benzothiadiazole conjugated polymer - Case study*, ELSEVIER, Computational and Theoretical Chemistry 977(2011) 157-162